ULTRA-LOW JITTER MODE-LOCKED FIBER LASER

WU KAN

School of Electrical & Electronic Engineering

A thesis submitted to the Nanyang Technological University
in fulfillment of the requirement for the degree of
Doctor of Philosophy

2012

Statement of Originality

I hereby certify that the content of this thesis is the result of original research done by me and has not been submitted for a higher degree to any other university or institute.

Date	Wu Kan

Acknowledgements

This thesis would not have been possible without the help from many generous people. I first wish to acknowledge my Ph.D. supervisor Professor Shum Ping for his invaluable encouragement and guidance. His passion in research inspired me in my journey of pursuing the Ph.D. degree. I am also very grateful to Dr. Fu Songnian and Dr. Zhao Luming for their kind help and the knowledge gained from them during my early days as a post-graduate student. I also wish to thank Dr. Ouyang Chunmei. Discussion with her was always inspiring. The advice received from Professor Sheel Aditya and Professor Luan Feng was of great values. I appreciate the help from Dr. Kenneth Lee and Dr. Huy Quoc Lam for the discussion on laser noise. I would like to especially thank my master supervisor Professor Chen Jianping. His research initiated my interest in the research field of photonics. Finally, I am grateful to the current and previous members of Network Technology Research Centre. They are Dr. Jiang Meng, Dr. Zhou Junqiang, Dr. Zhang Yixin, Wong Jia Haur, Huang Ying, Huang Guanghui, Wu Xuan and Liu Huanhuan.

Table of Contents

Summary

Lasers have been widely used in various fields since the invention of first laser in 1960. Low-noise passively mode-locked lasers, as a special kind of pulsed lasers, provide ultra low intensity fluctutation and timing jitter and therefore have significant applications in optical sampling, frequency metrology and high-precision clock distribution, etc. Therefore, it is important to investiage the methods to reduce the phase noise and timing jitter of the mode-locked lasers. Moreover, various noise conversion phenomena also affect the laser noise such as the noise conversion from the pump to the mode-locked lasers, or degrade the microwave signal quality synthesised from the mode-locked lasers such as the excess phase noise conversion in the photodetectors. It is also meaningful to understand and characterize these noise conversion phenomena.

In this thesis, we focus on three main aspects. They are timing jitter reduction for passively mode-locked fiber lasers, noise conversion from the pump to the mode-locked lasers and excess phase noise conversion induced by the photodetection process.

For the timing jitter reduction for passively mode-locked lasers, we first analyze the optimization of the cavity loss in order to suppress the indirect noise source coupled from the frequency jitter to the timing jitter. For the mode-locked laser in our experiment with a cavity net dispersion of -0.1 ps^2, a timing jitter reduction of 24% is demonstrated. Then a feedback control loop based on Proportional-Integral-Derivative (PID) control and piezoelectric transducer (PZT) is set up to lock the repetition frequency of the laser to an external reference oscillator. The phase noise at low offset frequency is found to be suppressed when the

feedback is turned on. We also investigate the effect of external incoherent addition structures. Two structures called Mach-Zehnder (MZ) and ring are studied. Both MZ and ring structures are found to be able to suppress the phase noise at specific spectrum positions (dependent on the design of the MZ or ring structures) for pulse trains with a background phase noise level above -130 dBc/Hz at high offset frequency range. This result can be applied to reduce the timing jitter for the pulse trains after amplification.

For the noise conversion from the pump to the mode-locked lasers, we first experimentally investigate the linear noise conversion from the pump relative intensity noise (RIN) to the RIN and phase noise of mode-locked fiber lasers at 1.55 μm. Two mode locking mechanisms, nonlinear polarization rotation (NPR) and semiconductor saturable absorber mirror (SESAM) are compared. Pump RIN is found to be the dominant noise source for both lasers (NPR laser and SESAM laser) and thus their RIN and phase noise can be predicted with the measured noise conversion ratios and pump RIN. It is also found that the SESAM laser shows a higher phase noise than the NPR laser due to the additional intracavity RIN to phase noise conversion caused by the slow saturable absorber effect of the SESAM. Then we study the nonlinear RIN conversion from the pump to the mode-locked lasers. The nonlinear RIN conversion is found to generate additional noise power at various harmonics kf_M with respect to the fundamental pump modulation frequency f_M. An exponential decay model is proposed to describe the behavior of the nonlinear RIN conversion. Physical explanation from the view of gain modulation is proposed and verifies the validity of this exponential decay model.

For the excess phase noise conversion induced by the photodetectors, we present a method based on the power dependent impulse response of the

photodetectors in order to characterize the excess noise conversion from optical RIN to electrical pulse width jitter (PWJ), relative amplitude noise (RAN) and phase noise in the photodetectors when detecting the optical pulse train from mode-locked lasers. Theoretical analysis is presented to describe the relations among these noise conversion ratios and to predict the measured electrical RAN and phase noise power spectral densities. The effect of the pulse width of incident optical pulses is also discussed. Moreover, a photodetector with higher impulse-response saturation power is found to allow a larger input optical power range while maintaining low RIN-to-phase-noise conversion ratio. These results provide useful guidelines for low-noise microwave synthesis by photo-detecting the output of a low-noise mode-locked laser.

List of Abbreviations

AC	Alternating Current
ADC	Analog-to-Digital Conversion
ASE	Amplified Spontaneous Noise
BPF	Band Pass Filter
CNT	Carbon Nanotube
CW	Continuous Wave
DC	Direct Current
DCF	Dispersion Compensating Fiber
DOS	Density of States
DSB	Double Side Band
DSP	Digital Signal Processing
DSF	Dispersion Shift Fiber
EDF	Erbium Doped Fiber
EDFA	Erbium Doped Fiber Amplifier
ENOB	Effective Number of Bits
FBG	Fiber Bragg Grating
FDL	Fiber Delay Line
FFT	Fast Fourier Transform
FWM	Four-Wave Mixing
GVD	Group Velocity Dispersion
HNLF	Highly Nonlinear Fiber

KLM	Kerr Lens Mode locking
LD	Laser Diode
LNA	Low Noise Amplifier
LPF	Low Pass Filter
MZ	Mach-Zehnder
MZI	Mach-Zehnder Interferometer
NF	Noise Figure
NFOEC	National Fiber Optics Engineers Conference
NPR	Nonlinear Polarization Rotation
OC	Optical Coupler
OCXO	Oven Controlled Crystal Oscillator
OFC	Optical Fiber Communication Conference
OSA	Optical Spectrum Analyzer
OSC	Oscilloscope
PBS	Polarization Beam Splitter
PC	Polarization Controller
PCF	Photonic Crystal Fiber
PD	Photodetector
PID	Proportional–Integral–Derivative
PLL	Phase Locked Loop
PM	Polarization Maintaining
PMFL	Passively Mode-locked Fiber Laser

PSD	Power Spectral Density
PWJ	Pulse Width Jitter
PZT	Piezoelectric Transducer
RF	Radio Frequency
RAN	Relative Amplitude Noise
RIN	Relative Intensity Noise
SA	Saturable Absorber
SE	Spontaneous Emission
SESAM	Semiconductor Saturable Absorber Mirror
SMF	Single Mode Fiber
SOA	Semiconductor Optical Amplifier
SPM	Self-Phase Modulation
SRS	Stimulated Raman Scattering
SSA	Signal Source Analyzer
SSB	Single Side Band
SWCNT	Single-Wall Carbon Nanotube
TEC	Temperature Controller
TIWDM	Tap Isolator Wavelength Division Multiplexer
VCO	Voltage Controlled Oscillator
VDL	Variable Delay Line
VOA	Variable Optical Attenuator
WDM	Wavelength Division Multiplexer

XPM Cross-Phase Modulation

List of Symbols

$A(t)$	Amplitude
Δa	Amplitude noise
$C_{Tot}(f)$	Total noise conversion ratio
$C_{Lin}(f)$	Linear noise conversion ratio
D	Group velocity dispersion in the units of s^2
D_p	Diffusion coefficient related to pulse momentum in Haus and Meccozi's model
D_t	Diffusion coefficient related to pulse timing in Haus and Meccozi's model
D_w	Diffusion coefficient related to pulse energy in Haus and Meccozi's model
E	Young's modulus
E_p	Pulse energy
$E(t)$	Electrical field
f	Frequency
Δf_g	Gain bandwidth
f_M	Modulation frequency
f_R	Repetition frequency
G	Gain
ΔG	Fluctuation of gain
g	Incremental gain or gain coefficient
Δg	Fluctuation of incremental gain

$G_x(t)$	Autocorrelation function of x
h	Planck constant
j	Imaginary part of complex numbers
J(t)	Relative timing jitter
ΔJ(t)	Difference of two relative timing jitter J(t)-J(t-T)
K_D	Differential coefficient in PID control
K_I	Integral coefficient in PID control
K_P	Proportional coefficient in PID control
L(f)	Phase noise power spectral density
n_{eff}	Effective group refractive index
P_{AV}	Average power
P(t)	Instant power
P_0	Magnitude of instant power
P_S	Saturation power
r_{RAN_P}	Laser RIN to electrical RAN (of the pulse) conversion ratio
r_{RAN_R}	Laser RIN to electrical RAN (of the repetition frequency) conversion ratio
r_{RF}	Pump RIN to relative RF power conversion ratio
r_{RIN}	Pump RIN to laser RIN conversion ratio
r_{PN}	Pump RIN to laser phase noise conversion ratio
Δr_{PN}	Change of pump RIN to laser phase noise conversion ratio
r_{PWJ}	Laser RIN to electrical pulse width jitter conversion ratio
$S_{f\_laser}(f)$	Repetition frequency jitter power spectral density of lasers

$S_J(f)$	Relative timing jitter power spectral density
$S_{PN}(f)$	Phase noise power spectral density
$S_{Pump\text{-}RIN}(f)$	RIN power spectral density of pump lasers
$S_{RIN}(f)$	RIN power spectral density
$S_t(f)$	Timing jitter power spectral density
$S_{t\_laser}(f)$	Timing jitter power spectral density of lasers
t	Time
Δt	Timing jitter
t_{FWHM}	Pulse width at full width half maximum
$T_{Nonlin}(f)$	Nonlinear noise conversion ratio
T_R	Pulse train period or round trip time of the laser cavity
w_0	Pulse energy
Z(f)	Suppression ratio
Z_{int}	Integral suppression ratio
γ_{sp}	Decay rate parameter used in Appendix A
$\delta(f)$	Delta function in frequency domain
$\delta P(t)$	Fluctuation of pulse power
ε	Error signal in section 3.3 and modulation depth in the rest part of thesis
η	Coupling ratio from pump modulation to saturation power modulation
θ	Enhancement factor due to the incomplete inversion of gain medium
μ	Poisson ratio
ν	Optical frequency

σ Cross section in chapter 5 and duty cycle in Appendix B

σ_{AC} Standard deviation of autocorrelation measurement

σ_{CC} Standard deviation of cross correlation measurement

σ_{f_laser} RMS frequency jitter of a laser

σ_t RMS timing jitter of a pulse train

σ_{t_laser} RMS timing jitter of a laser

τ Pulse width

$\Delta\tau$ Time delay in the autocorrelation calculation

τ_d Delay in MZ or ring structures in section 3.4

τ_p Relaxation time related to pulse momentum in Haus and Meccozi's model

τ_{ph} Photon life time in the cavity

τ_{sp} Upper state lifetime of the gain medium

τ_w Relaxation time related to pulse energy in Haus and Meccozi's model

ϕ Optical phase

$\Delta\varphi$ Phase noise of the repetition frequency

ω_0 Angular frequency of repetition frequency, i.e., $\omega_0 = 2\pi f_R$

ω_{sp} Frequency parameter used in Appendix A

List of Figures

List of Tables

1 Introduction

Since the demonstration of first ammonia maser by Charles Townes in 1953 [1], optical maser or laser has been predicted and later realized by T. H. Maiman as well as other researchers almost simultaneously in 1960 [2]. Many types of lasers have been developed based on different mechanisms. These lasers allow significant values in academic research and engineering applications [3-4]. Lasers at wavelength 1550 nm are of particular interest as the light sources for optical communication which has provided us ultrafast data rate and formed the backbone of our daily life. Other types of lasers such as high-energy pulsed lasers have been used for high-precision manufacturing. As a special type of laser, mode-locked lasers generate ultra-short optical pulses and have wide applications in various fields, e.g., optical sampling [8], frequency metrology [5-7], high-precision clock distribution [9-10] and microwave signal synthesis [11-17], etc. Among all these applications, in order to obtain high effective number of bits (ENOB) in optical sampling, high accuracy in frequency metrology and low timing error in clock distribution system, low noise is always a critical requirement for mode-locked lasers. Therefore it is important to understand the noise properties of a mode-locked laser and to find a way to improve it.

There are a few types of mode-locked lasers to be chosen as a low noise optical pulse source, e.g., solid-state lasers, fiber lasers and semiconductor lasers. Compared with the solid state lasers with bulky elements, fiber lasers are much more compact, cost effective and easy to maintain in the communication wavelength of 1550 nm, which has attracted intensive interest for the research on mode-locked fiber lasers. Semiconductor lasers are also potential to provide compact and cost effective solutions for mode-locked lasers but currently their phase noise is still

quite high [18-19] and the extinction ratio in the RF spectrum is lower than those of solid state lasers and fiber lasers. Therefore we focus our research topic onto the mode-locked fiber lasers. In the two types of mode-locked lasers, i.e., passive and active, both can achieve low-noise operation. For the applications mentioned above, passively mode-locked fiber lasers provide narrower pulse width, higher pulse energy and wider optical spectrum compared with actively mode-locked lasers. Thus, it is meaningful to investigate the characteristics of low-noise passively mode-locked fiber lasers and the related noise conversion phenomena.

1.1 *Literature review of different laser sources*

For different application purposes, e.g., communication, disease treatment and manufacturing, etc., there have been many types of lasers invented to meet the requirements in optical power, operation wavelength and noise, etc. Fig. 1.1 shows a tree of the laser types to form a picture of laser hierarchy. We focus on the types of pulsed lasers in the tree. All the laser types shown in Fig. 1.1 will be described in the following sections.

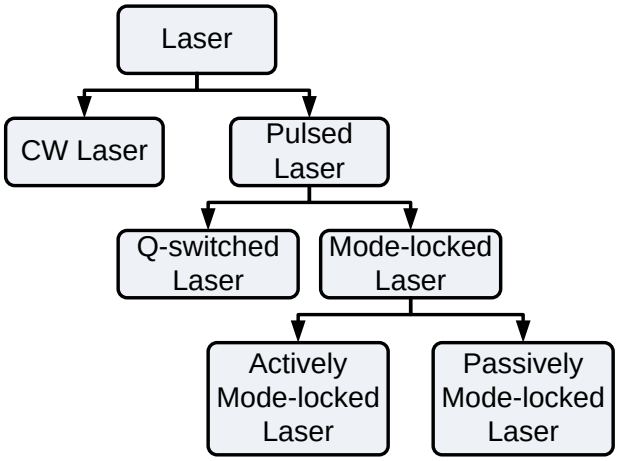

Fig. 1.1 Laser hierarchy based on different mechanisms

1.1.2 CW laser vs. pulsed laser

Continuous wave (CW) lasers are probably the most widely used lasers. Its structure is shown in Fig. 1.2. A typical CW laser contains gain media, resonant cavity and pump, and has continuous-wave output in time domain. This is why it is called CW laser. The first laser invented by T. H. Maiman in 1960 was a laser with Ruby as gain media and electrical flash light as pump [2]. The wavelength a CW laser outputs is dependent on the energy levels of the gain media. Currently, CW lasers with different gain media can cover the wavelengths from far ultra-violet region (<200 nm) to far infra-red region (>10 μm). The output power of CW lasers is time invariant and the average output power equals to peak power (instant power measured in a very short time range). CW lasers have wide applications in optical communication, optical sensing and etc.

Pulsed lasers are the development based on CW lasers. The output of pulsed lasers is, as the name has indicated, pulse train. This means, in time domain, lasers will periodically output a pulse within a very short time window and then output nothing in the rest of the time. The structure of pulsed lasers is the combination of CW laser and pulse shaper to achieve pulsed operation, as shown in Fig. 1.2. The technologies of pulse shaper can be grouped in two major mechanisms – Q-switching and mode locking [20]. These two mechanisms will be discussed in the next section. The average output power is not equal to peak output power due to the pulsed operation in the pulsed laser. A simple calculation example is given here: suppose the average output power is 5 mW, the repetition rate of pulse train is 40 MHz (corresponding to 25 ns period), the pulse width is 100 fs. Then the peak power of each pulse is given by P = 5 mW * 25 ns / 100 fs = 1.25 kW which is much higher than average power. Due to this feature, pulsed lasers are widely used in

nonlinear optics, material fabrication and etc. The comparison of CW lasers and pulsed lasers is summarized in Table 1.1

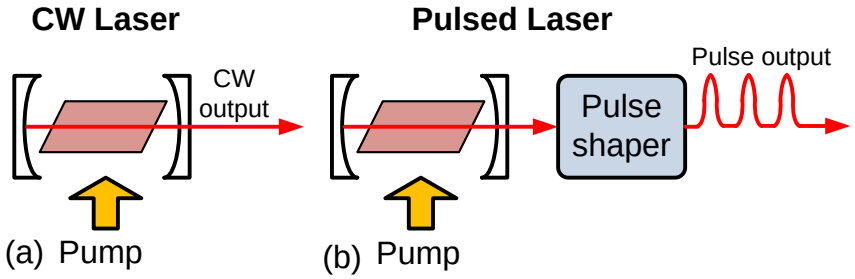

Fig. 1.2 Schematic diagrams of (a) CW laser and (b) pulsed laser

Table 1.1 Comparison between CW lasers and pulsed lasers

Laser type	CW laser	Pulsed laser
Laser structure	Gain media + resonant cavity + pump	CW laser + special designs for pulsed operation
Output in time domain	Continuous wave	Pulse train
Output power	Average power = peak power	Average power << peak power
Output in Frequency domain (wavelength domain)	Usually narrow spectrum	a wide range of spectrum

1.1.3 Q-switched laser vs. mode-locked laser

Q-switching and mode locking are two main methods to achieve pulse operation [4]. Q-switching adds a “shutter” in the CW laser. When the shutter is off, the CW laser cannot lase because the cavity is blocked by the shutter and cavity loss is much higher than the gain provided. Meanwhile the pump is still on so the energy from the pump will accumulate in the gain media and form a strong inversion distribution. When the shutter is on, the accumulated energy in the gain media will be released within a very short time and thus generates a pulse. The typical pulse width generated by Q-switching is >10 ns [4]. The shutter can be mechanical devices, e.g.,

chopper, or electrical devices, e.g., modulator. Q-switched lasers are usually used to generate pulse with high energy (e.g., Alvarez-Chavez obtained pulse with energy as high as 2.3 mJ [21]) and sometimes wide tunable range of central wavelength (e.g., Renaud obtained Q-switched operation with 40 nm tunable range [22]).

Mode locking is another mechanism to form pulse operation. The principle of it is quite different from Q-switching although sometimes laser output based on these two different mechanisms seems very similar. We know that there are many longitudinal modes in the laser cavity and usually the fundamental longitudinal mode is selected to output for CW laser. Mode locking is to allow many of these longitudinal modes to exist simultaneously and to lock the relevant phase of all these longitudinal modes. Mathematically, we can derive this process [4]. Each longitudinal mode in the cavity can be written as follows

$$E_m \exp[j(\phi_m - 2\pi\nu_m t)] \tag{1.1}$$

where E_m, ϕ_m and $\nu_m = mc/(nL) = m\Delta\nu$ are amplitude, phase and frequency of m-th mode. The total optical field is then given by

$$E(t) = \sum_{m=-M}^{M} E_m \exp[j(\phi_m - 2\pi\nu_m t)] \tag{1.2}$$

where M is related to the number of modes. Total number of modes is $2M+1$. If all the relevant phases are locked as $\Delta\phi = \phi_m - \phi_{m-1} = \phi$, or $\phi_m = m\phi + \phi_0$, and all the amplitudes are supposed to be the same and equal to E_0, then we have

$$E(t) = \sum_{m=-M}^{M} E_m \exp[\, j(\phi_m - 2\pi\nu_m t)] \\ = \sum_{m=-M}^{M} E_0 \exp[\, j(m\phi - 2m\pi\Delta\nu t) + j\phi_0\,] \tag{1.3}$$

$$\left|E(t)\right|^2 = \frac{\sin^2[(2M+1)\pi\Delta\nu t + \phi/2]}{\sin^2(\pi\Delta\nu t + \phi/2)} {E_0}^2 \tag{1.4}$$

Fig. 1.3 gives the plot of $\left|E(t)^2\right|$ with respect to different values of the number of modes *M*. It can be seen that the more modes are phase locked, the weaker the wing will be and the narrower the pulse will be. Pulse width is $\tau = 1/[(2M+1)\Delta\nu]$. Typical pulse width of mode-locked operation is <10 ps. Since the pulse width is very small, pulse train generated by mode locking can easily obtain high peak power (see the example given in CW laser vs pulsed laser section). The tunable range of central wavelength is dependent on the gain bandwidth of the gain media. Ti : Sapphire lasers can have wide tunable range (e.g., >40 nm).

Two major mechanisms to achieve mode locking are called active mode locking and passive mode locking [3-4]. Active mode locking utilizes an external modulator to actively control the laser cavity loss and obtain mode-locked operation. Passive mode locking utilizes some passive material such as saturable absorber to reach mode-locked operation. These two mechanisms will be discussed and compared in next section. We also provide a comparison between Q switching and mode locking in Table 1.2.

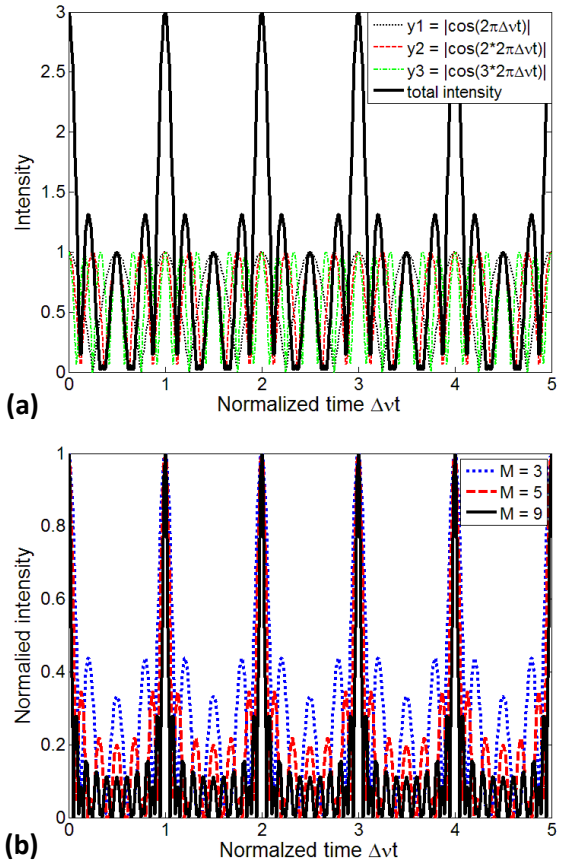

Fig. 1.3 (a) Intensity of three phase locked modes and their total intensity and (b) Normalized total intensity of phase locked modes with respect to different number of modes

Table 1.2 Comparison between Q switching and mode locking technologies

Types	Q switching	Mode locking
Mechanisms	By controlling laser on and off with shutter or similar mechanisms	By controlling laser gain/loss with external modulator (active) or saturable absorber (passive)
Pulse feature	High energy pulse width is usually > 10 ns	High peak power and high repetition rate pulse width is usually < 10 ps
Tunable range of central wavelength	> 40 nm	> 40 nm

1.1.4 Actively mode-locked lasers vs passively mode-locked lasers

As we have mentioned previously, active mode locking and passive mode locking are two major mechanisms to obtain mode-locked operation of lasers. Active mode locking is realized by inserting a modulator in the laser cavity. When a RF signal is applied on the modulator, modulator will generate a periodic modulation of cavity loss (equivalent to cavity gain) or optical phase with the same frequency of RF signal. Then those photons fitting this gain/loss/phase modulation window will obtain highest gain each round trip in the laser cavity. Thus periodic pulse train occurs. This process can be illustrated in Fig. 1.4 (a). The typical design of an actively mode-locked laser is also given in Fig. 1.4 (b). One thing to be noted is that in order to obtain a stable operating pulse train, the modulation frequency must be equal to the fundamental repetition rate frep=1/T_R (T_R is cavity round trip time) or its multiples because when the pulse finish one round trip and enter the modulator again it requires the same high gain it experienced last time. Otherwise it will shift in time domain to obtain higher gain or new pulse will build up which all leads to the instability of the mode locking operation.

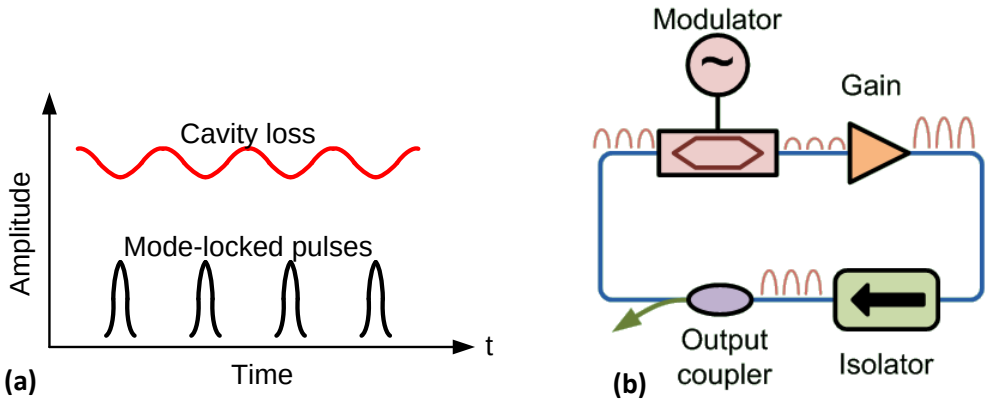

Fig. 1.4 (a) Modulation on cavity loss in active mode locking process in time domain, the pulses will be generated at low-loss windows and (b) a typical design of an actively mode-locked laser

One advantage of actively mode-locked laser is that it can operate at harmonic mode-locking state, which means there are many pulses simultaneously running inside the laser cavity, and the repetition rate is N/T_R. Typical repetition rate of actively mode-locked laser is from 1 GHz ~ 40 GHz [23]. And the interval between two adjacent pulses can be easily controlled by modulator. The pulse width is typically a few picoseconds and the spectrum width is typically less than a few nanometers.

Passive mode locking requires no active component, e.g., modulator, in the laser cavity. Instead it utilizes a key component called saturable absorber to achieve mode locking operation [3-4]. Saturable absorber is a kind of material or physical mechanism that exhibits higher loss for low input optical power and lower loss for high input optical power, and therefore works as a pulse shaper. There are two major types of saturable absorbers, that is material based and physical mechanism based (called artificial) saturable absorbers. For certain materials, they have finite density of states (DOS) in the upper energy state. And when the upper energy state is filled with the electrons excited by the incident laser beam, they cannot further absorb photons and exhibits low loss property. These saturable absorbers include semiconductor saturable absorber mirror (SESAM) [20], carbon nanotubes [24-25] and graphene [26-27]. For artificial saturable absorbers, some physical mechanisms are usually applied to achieve power dependent loss. These includes [4] Kerr lens mode-locking (KLM), nonlinear polarization rotation (NPR) and etc. KLM utilizes the property that high optical power can change the refractive index (Kerr effect) and causes a smaller beam size. This smaller beam size can result in lower loss by letting the beam cross a small hole (hard KLM) or higher gain by controlling the pump profile in the gain media (soft KLM). KLM is usually used by mode-locked

Ti : Sapphire laser centered at 780 nm. NPR works similarly. High power leads to larger change of refractive index and thus a large angle of polarization rotation in the birefringence media such as fiber. This power dependent polarization rotation then is converted to power dependent loss by adding a polarizer whose axis matches the polarization angle of high power components. NPR is usually used by mode-locked fiber laser centered at 1064 nm (Yb-doped fiber laser), 1550 nm (Er-doped fiber laser) or other wavelengths.

Pulses running in the passively mode-locked laser usually have higher peak power, narrower pulse width, and wider spectrum than those in actively mode-locked laser. For passive mode locking, the peak power is typically > 100 W. The pulse width is typically < 10 ps. The passively mode-locked laser is the only way ever developed to generate sub-10 fs pulse width [28]. The spectrum width is typically > 6 nm. Passively mode-locked lasers usually operate at fundamental frequency which means there is only one pulse running in the cavity. The lasers can also operate at harmonic mode locking but the interval from pulse to pulse is very hard to make equal. This drawback limits the highest repetition frequency that passively mode-locked lasers can achieve. Table 1.3 gives the comparison between actively and passively mode-locked lasers.

Table 1.3 Comparison between actively and passively mode-locked lasers

Laser type	Actively mode-locker laser	Passively mode-locker laser
mechanism	Gain/loss modulation by intra-cavity modulator	Power dependent loss/gain by saturable absorber
Peak power	< 0.1 W	> 100 W
Pulse width	~10 ps	< 10 ps
Spectral width	< 5 nm	> 6 nm
Repetition rate	1 GHz ~ 40 GHz	< 5 GHz
Harmonic mode-locked operation	Can, usually operating at this mode to achieve high repetition rate	Can, but seldom operating at this mode due to poor stability and noise properties
Application	Optical communication, optical sampling and etc.	Nonlinear optics, frequency metrology and etc.

1.2 *Motivation*

As discussed in the previous sections, mode-locked lasers generate ultra-short pulses with high transient peak power compared with the other types of lasers, e.g., CW lasers and Q-switched lasers. Also, mode-locked lasers exhibit ultra-low noise properties which suggests promising high-precision applications, e.g., high-resolution optical sampling [8], frequency metrology [5-7] and drift-free clock distribution [9-10]. For optical sampling, it has been reported a 10 Tera samples/s sampling rate with a resolution of 4.5 effective bits which is the fastest sampling system ever developed [8]. For frequency metrology, the Nobel Prize in physics 2005 was awarded to John L. Hall and Theodor W. Hänsch for their contributions to the laser based frequency metrology technology [29]. With this technology, the accuracy of frequency measurement can approach to 10^{-18} which is even better than

the currently used atomic clock [5, 7]. Other applications such as high precision satellite-based navigation system (e.g., GPS) may also emerge. F. X. Kartner's group in MIT has recently demonstrated the possibility to synchronize large number of facilities with extremely high timing accuracy (< 10 fs drift for 72 hours) by using low-noise mode-locked lasers [9].

To draw a clearer picture of the importance of low noise mode-locked lasers, we would like to give an example of optical sampling. Optical sampling provides an optical solution for high-precision high-speed signal sampling which allows a variety of applications such as high-speed signal processing for radar system. The simplified mechanism of optical sampling is illustrated in Fig. 1.5. A pulse train with repetition rate f_{rep} is used to detect the instant amplitude of a RF signal by an electro-optical modulator. Then the pulse train which carries the information of RF signal is equally separated into N paths with repetition rate f_{rep}/N (e.g., N=4 in the figure). These N pulse trains will be expanded (e.g., stretched in time domain) and converted to electrical signal and detected by traditional low-speed electrical analog-to-digital converters (ADCs). Finally the output of N-path electrical ADCs will be combined together to re-build the input RF signal. A few techniques can achieve the function that separating pulses to different ADCs. For example, one can use a DWDM to divide one input pulse to a few pulses with different center wavelengths. Then these pulses can go to different ADCs through another DWDM after sampling the RF signal.

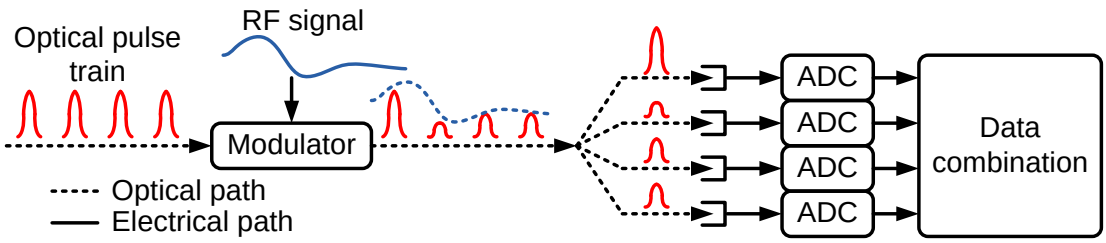

Fig. 1.5 Illustration of high-speed high-resolution optical sampling

Then we discuss the effect of laser noise on optical sampling system. Suppose we have an optical pulse train with repetition rate f_R, the highest target signal frequency we can detect is $f_R/2$ according to Nyquist sampling theorem. Suppose the target signal is $\sin\pi f_R t$. The peak to peak amplitude of this signal is 2 and the largest slope appears at $t=m\pi$. If pulse train has a timing jitter Δt (it means the pulse will randomly shift from its original position by Δt), the largest sampling error will occur at the point with largest slope, as shown in Fig. 1.6 (a), and therefore, the error can be given by $\Delta I = \sin \pi f_R \Delta t \approx \pi f_R \Delta t$. This error must be smaller than the minimum quantization unit $2/2^N$ to avoid the generation of an error bit. The relation between timing jitter and effective number of bits (ENOB) of optical sampling is therefore given by $\Delta I \approx \pi f_R \Delta t < 2/2^N$ or $N < 1 - \log_2 \pi f_R \Delta t$. Fig. 1.6 (b) describes the relation between ENOB of optical sampling (N) and timing jitter (Δt) at different repetition rate of the pulse train. The typical commercial high-speed ADC is around 780 MHz and 12 bits [30]. For comparison, if we can obtain a mode-locked laser with 1 GHz repetition rate and 20 fs timing jitter, the corresponding ENOB can be as high as 15. Therefore optical sampling with a low-noise mode-locked laser is a very promising solution for high-speed high-accuracy sampling compared with the traditional electrical ADC solutions.

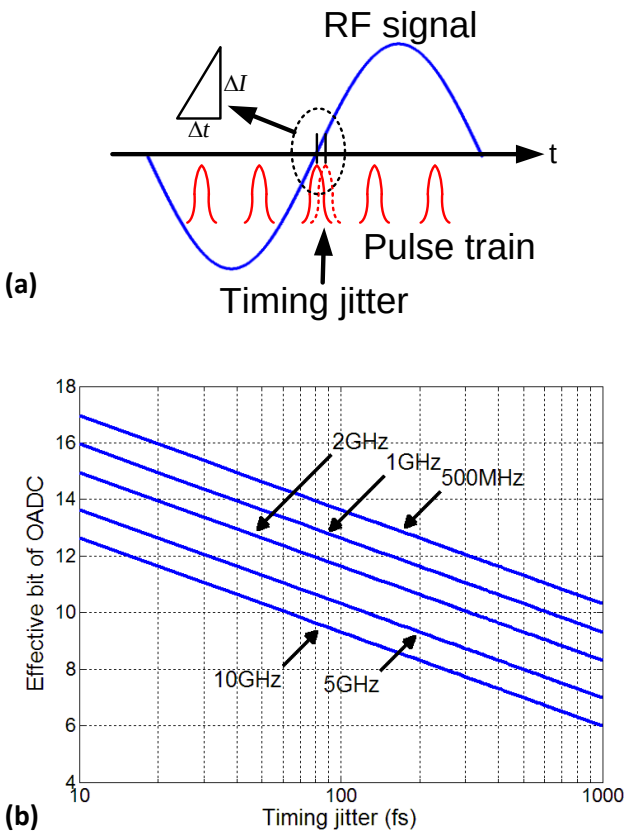

Fig. 1.6 (a) Effect of timing jitter on optical sampling error and (b) theoretical limit on effective bit of optical sampling with respect to different timing jitter at different repetition rate of the pulse train

As we can see, many research and engineering fields can benefit if we can better understand the noise characteristics of the mode-locked lasers and design a low-noise mode-locked laser. Up to now, the noise properties of mode-locked laser has been widely investigated including the quantum noise limit [31-36], method of noise measurement [37-48] and technologies to reduce noise of mode-locked laser [33, 49-50]. However, there is still much room to investigate including the method to reduce the laser noise, low-noise microwave signal synthesis and etc. Also, compared with the solid state mode-locked lasers, mode-locked fiber lasers are easy to align and of low cost while maintaining the low-noise property of solid state mode-locked lasers, which is very promising for commercial applications as well as

laboratory research. Therefore it is very meaningful to investigate the technology to achieve low-noise mode-locked fiber lasers and related noise conversion phenomena.

1.3 *Objective*

The objective of our research is to investigate the noise properties of the passively mode-locked fiber lasers and to reduce the timing jitter of mode-locked fiber lasers. The noise conversion phenomena including the noise conversion from the pump to the mode-locked lasers and the noise conversion in the photodetectors are also discussed theoretically and experimentally.

1.4 *Main Contributions*

Three main contributions are presented in the thesis.

a) We investigate the methods to reduce the phase noise and timing jitter for the mode-locked lasers at 1.5 μm. Based on the theory on the quantum limited noise for mode-locked lasers, the optimization of the cavity loss is found to suppress the indirect noise source coupled from the frequency jitter to the timing jitter. We demonstrate a timing jitter reduction of 24% for a mode-locked laser with the cavity net dispersion of -0.1 ps^2. We also apply a feedback control loop to lock the repetition frequency of the mode-locked laser to an external reference oscillator and suppress the phase noise at low offset frequency of the laser when the feedback loop is on. Moreover, we investigate the effect of external incoherent addition structures with Mach-Zehnder (MZ) and ring setups which are found to suppress the phase noise at specific spectrum positions (dependent on the design of the MZ or ring structures) for pulse trains with a background phase noise level above -130 dBc/Hz

at high offset frequency range. This result can be applied to reduce the timing jitter of the pulse trains after amplification, e.g., Erbium-doped fiber amplifier (EDFA).

b) Both linear and nonlinear noise conversions from the pump to the mode-locked lasers are investigated. For linear noise conversion, two mode locking mechanisms, nonlinear polarization rotation (NPR) and semiconductor saturable absorber (SESAM) are compared. Pump relative intensity noise (RIN) is found to be the dominant noise source for both NPR based mode-locked laser (NPR laser) and SESAM based mode-locked laser (SESAM laser) and thus their RIN and phase noise can be predicted with the measured noise conversion ratios and pump RIN. Then we study the nonlinear RIN conversion from the pump to the mode-locked lasers. The nonlinear RIN conversion is found to generate additional noise power at various harmonics kf_M with respect to the fundamental pump modulation frequency f_M. An exponential decay model is proposed and the physical explanation from the view of gain modulation verifies the validity of this exponential decay model.

c) The excess phase noise conversion induced by the photodetection process is characterized. We present a method based on the power dependent impulse response of the photodetectors to characterize the excess noise conversion from optical RIN to electrical pulse width jitter (PWJ), relative amplitude noise (RAN) and phase noise in the photodetectors when detecting the optical pulse train from mode-locked lasers. Theoretical analysis has been presented to describe the relations among these noise conversion ratios and to predict the measured electrical RAN and phase noise power spectral densities. The effect of pulse width is also discussed. Moreover, a photodetector with higher impulse-response saturation power is found to allow a larger input optical power range while maintaining low RIN-to-phase-noise

conversion ratio. These results provide useful guidelines for low-noise microwave signal synthesis by photo-detecting the output from a low-noise mode-locked laser.

1.5 *Outline of the thesis*

This thesis is organized as follows.

In Chapter 1, we briefly introduce different types of lasers including continuous wave (CW) lasers, Q-switched lasers, passively and actively mode-locked lasers. Then we explain the motivation of our work, in which as an example, we analyze the effect of laser noise (especially timing jitter) on the effective number of bits (ENOB) of a photonic analog-to-digital converter system at various sampling frequencies. The objective and main contributions are also provided.

In Chapter 2, we review the quantum noise of a mode-locked laser which was first proposed by Haus and Meccozi [31]. Recently, Paschotta has extended the model to a more general condition suitable to any kind of mode-locked lasers [34]. Then we discuss the measurement technologies of the intensity noise and phase noise (timing jitter) of the mode-locked lasers. RF spectrum based method [45], demodulation method [51] and cross-correlation method [43] are mathematically analyzed and compared.

In Chapter 3, methods to suppress the noise, especially timing jitter, of the mode-locked lasers are investigated. Based on the quantum noise model, timing jitter of the mode-locked lasers can be reduced by optimization of the cavity loss. A piezoelectric transducer (PZT) based feedback loop is applied to stabilize the repetition frequency and reduce the noise at low offset frequency region. Moreover,

the incoherent addition structures are also discussed to reduce the timing jitter outside the laser cavity of mode-locked lasers.

In Chapter 4, we discuss the linear noise conversion from the pump to the mode-locked lasers. It is found that the pump relative intensity noise (RIN) is a dominant noise source for the mode-locked lasers. And the noise of the mode-locked lasers can therefore be predicted by the measured pump RIN and noise conversion ratios.

In Chapter 5, the nonlinear noise conversion from the pump RIN to the RIN of the mode-locked lasers is investigated. An exponential decay model is proposed and matches the experimental results well. The physical explanation from the view of gain modulation is presented and verifies the validity of the exponential decay model.

In Chapter 6, the excess noise conversion induced by the photodetectors is characterized. Due to the power dependent pulse broadening and pulse delay, photodetectors cause excess noise conversion from laser RIN to the electrical noise after photodetection. Theoretical analysis is performed and impulse response method is applied to characterize this noise conversion effect.

Chapter 7 is the conclusions and the future work. The main research results in Chapter 3-6 are summarized. For future work, mode-locked fiber laser consisting of only Erbium-doped photonic crystal fiber (PCF) is interesting to investigate which allows the possibility of wideband dispersion compensation for a wider output spectrum and short cavity length for a higher repetition frequency. Low-noise pulse train amplification is another possible direction for future work.

Appendix A gives the derivation of the equations used in Chapter 4 and Appendix B gives the definition and calculation of the Fourier coefficients used in Chapter 6.

2 Quantum noise of mode-locked lasers and noise measurement

This chapter describes the noise type, quantum noise of mode-locked lasers and how the noise is measured. This chapter is fundamental for the rest chapters because all the noise measurements in those chapters are based on the theory and methods described in this chapter.

2.1 *Noise types of a pulse train*

Noise performance is a key factor describing the quality of a pulse train output from a mode-locked laser. For high-precision applications, low-noise pulse train is always preferred. There are two major types of noise in a pulse train: relative intensity noise (RIN) and timing phase noise. We first consider a sine wave signal with noise given in Eq.(2.1).

$$V_{in}(t) = (1 + \Delta a(t)) \cos(2\pi f_R t + \Delta\varphi(t)) \tag{2.1}$$

$$\Delta\varphi(t) = 2\pi f_R \Delta t(t) \tag{2.2}$$

where Δa is RIN and $\Delta\varphi$ is the timing phase noise. Here we should mention that the timing phase noise is referred to the phase noise of the repetition frequency not the phase noise of optical carrier. All the phase noise used in the thesis later referred to the timing phase noise. The phase noise $\Delta\varphi$ is directly related to the timing jitter Δt with Eq.(2.2). For pulse train, the signal can be decomposed as a series of frequency comb in frequency domain as $f_R, 2f_R ... kf_R ...$. We will show later that the phase noise (or timing jitter) and the RIN of a pulse train are equal to the phase noise and the RIN of the fundamental frequency f_R. An illustration of an ideal pulse

train, a pulse train with intensity noise and a pulse train with phase noise is given in Fig. 2.1. It can be seen that the RIN represents the pulse amplitude (or intensity) fluctuation and the phase noise represents the pulse timing fluctuation.

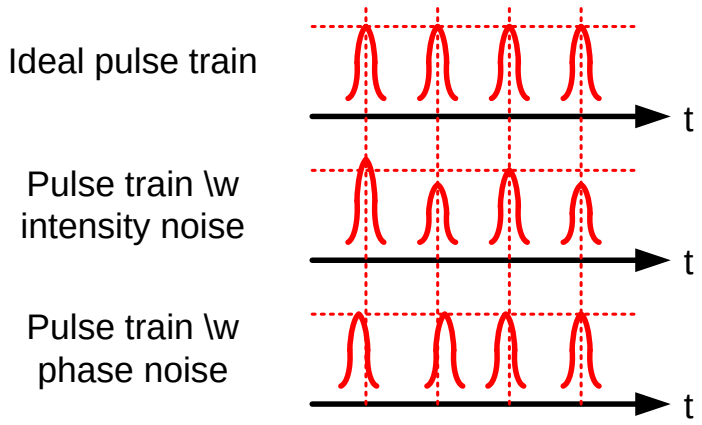

Fig. 2.1 Illustration of an ideal pulse train, a pulse train with intensity noise and a pulse train with phase noise, respectively

2.2 *Power spectral density of noise*

As we know, noise is not a periodic signal but a random process in time domain, so it is not so meaningful when we talk about the Fourier transform of a noise which is what we usually do for a signal to analyze its spectral property. However we do observe some noise spectra when using an RF spectrum analyzer to measure an electrical signal. Power spectral density (PSD) is used to describe the property of noise.

Suppose these is a noise $n(t)$ in time domain, we calculate its autocorrelation function defined as follows

$$G_n(\Delta\tau) \equiv \langle n(t)n(t-\Delta\tau)\rangle \equiv \int_{-\infty}^{+\infty} n(t)n(t-\Delta\tau)dt \qquad (2.3)$$

where $G_n(\tau)$ is the autocorrelation function and $\Delta\tau$ is time delay. The PSD of noise $n(t)$ is given by the following equation, meaning that PSD is the Fourier transform of the autocorrelation function

$$S_n(f) = \int_{-\infty}^{+\infty} G_n(\Delta\tau) e^{j2\pi f\Delta\tau} d\Delta\tau \tag{2.4}$$

The root mean square (RMS) value of $n(t)$ is given by

$$\langle n \rangle = \sqrt{\int_{-\infty}^{+\infty} S_n(f) df} \tag{2.5}$$

An interesting comparison is that if we assume $n(t)$ is a signal rather than a noise. Then we are able to calculate the Fourier transform of $n(t)$, that is

$$N(f) = \int_{-\infty}^{+\infty} n(t) e^{j2\pi ft} dt \tag{2.6}$$

And the PSD of $n(t)$ is then given by

$$\begin{aligned} S_n(f) &= \int_{-\infty}^{+\infty} G_n(\Delta\tau) e^{j2\pi f\Delta\tau} d\Delta\tau \\ &= \int_{-\infty}^{+\infty} \int_{-\infty}^{+\infty} n(t) n(t-\Delta\tau) dt e^{j2\pi f\Delta\tau} d\Delta\tau \\ &= \int_{-\infty}^{+\infty} \int_{-\infty}^{+\infty} n(t) n(x) dt e^{j2\pi f(t-x)} dx \\ &= \int_{-\infty}^{+\infty} n(t) e^{j2\pi ft} dt \cdot \int_{-\infty}^{+\infty} n(x) e^{-j2\pi fx} dx \\ &= N(f) \cdot N^*(f) \\ &= |N(f)|^2 \end{aligned} \tag{2.7}$$

It is easy to find that PSD describes the noise power distribution in the frequency domain. Suppose the unit of $n(t)$ is "x", with reference to Eq.(2.5), one can find that the unit of PSD $S_n(f)$ is "x2/Hz". For example, the unit of PSD is "1/Hz" for relative intensity noise with the units of "1", "rad2/Hz" for phase noise with the

units of “rad”, “s2/Hz” for timing jitter with the units of “s” and “Hz2/Hz” for frequency jitter with the units of “Hz”. The unit of PSD is often expressed in logarithmic scale as “dB/Hz” or “dBc/Hz”. dBc means the noise power is a relative value with reference to the carrier power. Of course when one calculates the integration in Eq.(2.5), the units must be changed back to a linear scale. The horizontal axis of a PSD figure is frequency or offset frequency when one talking about the noise around a certain carrier frequency.

2.3 *Quantum noise of mode-locked lasers*

Mode-locked lasers are good choices for low-RIN and low-phase-noise pulse train sources due to their low quantum noise. Quantum noise represents the lowest noise a mode-locked laser can achieve, that is, all technical noises are isolated including the noises induced by thermal fluctuation, air flow, mechanical vibration and etc. For mode-locked lasers, quantum noise is generated purely by spontaneous emission (SE) of the gain media which can never be isolated and always exists. Haus and Mecozzi first systematically investigated the quantum noise of mode-locked lasers [31]. Haus and Mecozzi’s derivation is based on soliton perturbation theory. Their theory gives the quantum noise limit of phase noise and intensity noise in a mode-locked laser. We do not give the detailed derivation of Haus and Mecozzi’s model here because this model was later extended to a broader content by Paschotta [34, 36] and thus can be considered as a special case of soliton laser in Paschotta’s model. Paschotta’s model will be discussed in detail later in this sub-section.

The phase noise power spectral density derived by Haus and Meccozi [31] is given in Eq.(2.8) with some coefficients later corrected by Paschotta [34]

$$L(f) = (2\pi f_R)^2 \left[\frac{D^2 D_p}{T_R^2} \frac{1}{(2\pi f)^2((2\pi f)^2 + \tau_p^{-2})} + \frac{D_t}{(2\pi f)^2} \right]$$
$$= (2\pi f_R)^2 \left[\frac{1}{(2\pi f)^2} \frac{4D^2 \theta h\nu}{3T_R^3 w_0 \tau^2} \frac{g}{(2\pi f)^2 + \frac{4g^2}{9\pi^4 T_R^2 \Delta f_g^4 \tau^4}} + \frac{1}{(2\pi f)^2} \frac{\pi^2 \tau^2 \theta h\nu}{3 w_0 T_R} g \right] \tag{2.8}$$

where $D_p = \frac{2}{3w_0\tau^2}\theta\frac{2g}{T_R}h\nu$ and $D_t = \frac{\pi^2\tau^2}{6w_0}\theta\frac{2g}{T_R}h\nu$ are diffusion constants of quantum noise, representing the noise properties of offset frequency and timing, respectively, θ is the enhancement factor due to the incomplete inversion of the gain medium ($\theta = N_2/(N_2 - N_1)$ for a non-degenerate two-level system. Ideally, we can let $\theta = 1$), $\tau_p = 3\pi^2 T_R \Delta f_g^2 \tau^2/(2g)$ is the relaxation time, D is the total group dispersion in the units of s^2, T_R is the round trip time, w_0 is the total energy in the cavity, g is the incremental gain per round trip, τ is the pulse duration and Δf_g is the gain bandwidth.

This equation indicates two mechanisms describing how spontaneous emission couples to phase noise (timing jitter). The first term represents an indirect contribution to phase noise coupled from the random shift of center frequency caused by spontaneous emission via group velocity dispersion. The second term represents a direct contribution to phase noise (random shift of pulse position) caused by spontaneous emission.

The intensity noise PSD is given in Eq.(2.9)

$$S_{RIN}(f) = \frac{1}{w_0^2} \frac{D_w}{((2\pi f)^2 + \tau_w^{-2})} \tag{2.9}$$

where $D_w = 2w_0\theta\frac{2g}{T_R}h\nu$ is the diffusion constants of quantum noise, representing the noise properties of energy, $\tau_w = T_R/(2g_s - 2\gamma A_0^2)$ is the relaxation time. Different relaxation time is related to different parameters used in Haus and Meccozi's model. So the spectrum of relative intensity noise is a Lorentz shape with knee frequency $f_{knee} = (2\pi\tau_w)^{-1}$.

Later Namiki [32] and Jiang [33] developed Haus and Meccozi's model in stretched pulsed mode-locked laser and semiconductor mode-locked laser, respectively. The analysis is very similar to what Haus and Meccozi did in their model, so we just give a summary of these three models in Table 2.1 and won't discuss further.

Many researchers have contributed to the analysis of the noise of mode-locked lasers. Menyuk also analyzed the relaxation oscillation and frequency pulling effect in the mode-locked lasers [52]. Paschotta proved that Haus and Meccozi's model can be adapted to the laser cavity with different pulse shape (corresponding to different cavity dispersion and mode locking states) because the basic derivation in their theory was nothing to do with soliton [34, 36]. Paschotta re-derived Haus and Meccozi's model in a more general way. His theory can be summarized as follows.

Table 2.1 Summary of three models from Haus & Meccozi, Namiki and Jiang

Researchers	Haus & Meccozi	Namiki	Jiang
Mode-locked laser type	Soliton lasers with hyperbolic secant pulse shape	Stretched pulsed lasers with Gaussian pulse shape	Semiconductor lasers
Different laser cavities can the theories be applied to	Anomalous dispersive cavity	Dispersion compensated cavity	Semiconductor cavity
Different considerations in the theories	Fundamental theory for soliton laser using soliton perturbation theory	Considering the Gaussian pulse in a nearly zero dispersive cavity where pulses are periodically stretched and compressed	Considering the amplitude and phase modulation depth in the actively mode-locked semiconductor lasers; Considering the carrier-photon population coupling in semiconductor material
Merits and limitations	Relatively simple and later be proven to be able to be extended to other laser cavities with nearly zero or normal dispersion	Complicated and only suitable for laser cavities with nearly zero dispersion	Complicated and only suitable for semiconductor lasers

The variance of the pulse position is defined in Eq.(2.10) where $\bar{P}(t)$ is the noiseless pulse instant power, $E_p = \langle \bar{P}(t) \rangle T_R$ is the average pulse energy. In the derivation of the last part in Eq.(2.10), two equations of Eqs.(2.11) and (2.12) are used where $G_{\delta A}$ is the autocorrelation function, δA and δP are the fluctuation of pulse amplitude and power respectively. For soliton operation $\bar{P}(t) = P_0 \operatorname{sech}^2(t/\tau)$, the variance then becomes Eq.(2.13) where $t_{FWHM} = \sqrt{2 \operatorname{arccosh} \sqrt{2}}\ \tau$ is the pulse

width at full width half maximum (FWHM). For Gaussian pulse, the coefficient in Eq.(2.13) is 0.1803.

$$\sigma_t^2 \equiv \left[\frac{\int t\delta P(t)dt}{\int \bar{P}(t)dt}\right]^2 = \frac{1}{E_p^2}\left[\int t\delta P(t)dt\right]^2 = \frac{h\nu}{E_p^2}\int t^2\bar{P}(t)dt \qquad (2.10)$$

$$G_{\delta A}(\Delta\tau) \equiv \left\langle \delta A^*(t)\delta A(t-\Delta\tau)\right\rangle = \frac{h\nu}{2}\delta(\Delta\tau) \qquad (2.11)$$

$$\delta P(t) = A(t)\delta A^*(t) + A^*(t)\delta A(t) \qquad (2.12)$$

$$\sigma_t^2 = \frac{h\nu}{E_p^2}\int t^2\bar{P}(t)dt = \frac{h\nu}{E_p^2}\frac{\pi^2}{6}P_0\tau^3 = \frac{\pi^2}{12}\frac{h\nu}{E_p}P_0\tau^2 = 0.2647\frac{h\nu}{E_p}P_0t_{FWHM}^2 \qquad (2.13)$$

The physical meaning of σ_t^2 is that the average shift of pulse position is σ_t in time T_R. So the timing jitter noise spectrum is white noise $S_t = \sigma_t^2 / f_R$, so that timing jitter $\Delta t = \sqrt{\int_0^{f_R} S_t df} = \sigma_t$, and the phase noise spectrum is given by $L(f) = (2\pi f_R)^2 S_t = (2\pi f_R t_{FWHM})^2 0.2674 h\nu / P_{AV}$. This result is valid for any optical pulse train with hyperbolic secant shape, which defines the minimum noise we can achieve and is usually called shot noise.

Similarly, the variance of pulse position output from a laser is given in Eq.(2.14) where *g* is the incremental gain per round trip. Then it can be proved that the timing jitter noise spectrum is given in Eq.(2.15).

$$\sigma_{t\_laser}^2 = \frac{h\nu}{E_p^2}2g\int t^2\bar{P}(t)dt \qquad (2.14)$$

$$S_{t\_laser} = \sigma_{t\_laser}^2 \frac{1}{(2\pi f)^2} \frac{1}{T_R} \tag{2.15}$$

The variance and spectrum of optical frequency noise can be given in Eq.(2.16) and Eq.(2.17) where τ_w is the relaxation time (recovery force) induced by gain filtering effect.

$$\sigma_{f\_laser}^2 = \frac{h\nu}{E_p^2} 2g \int f^2 \bar{P}(f) dt \tag{2.16}$$

$$S_{f\_laser} = \sigma_{f\_laser}^2 \frac{1}{(2\pi f)^2 + \tau_w^{-2}} \frac{1}{T_R} \tag{2.17}$$

This frequency noise then couples to the timing jitter noise via dispersion as $S_{t\_laser} = \left(\frac{D}{fT_R} \right)^2 S_{f\_laser}$ and the total timing noise spectrum is derived in Eq.(2.18).

$$S_{t\_laser} = \frac{1}{(2\pi f)^2} \frac{1}{T_R} \frac{h\nu}{E_p^2} 2g \int t^2 \bar{P}(t) dt + \left(\frac{D}{fT_R} \right)^2 \frac{1}{(2\pi f)^2 + \tau_w^{-2}} \frac{1}{T_R} \frac{h\nu}{E_p^2} 2g \int f^2 \bar{P}(f) dt \tag{2.18}$$

And phase noise spectrum is given by $L(f) = (2\pi f_{rep})^2 S_{t\_laser}(f)$. For hyperbolic secant pulse, this formula is the same as the one given by Haus and Meccozi in Eq.(2.8). The whole derivation process is not related to the exact pulse shape and therefore the formula is valid for all kinds of pulse shape and different laser cavities.

Besides the theoretical work, Paschotta also first proposed software simulation of phase noise and intensity noise of the mode-locked laser. Since Haus and Meccozi's theory is based on solving master equation, it is sometimes less accurate for the lasers with relatively complex structure of the cavity. Software

simulation can completely solve this problem and works for most kinds of solid state lasers and fiber lasers. For example, Paschotta's simulation predicted that the phase noise spectrum of a mode-locked laser with normal cavity dispersion (this laser is also called self-similar mode-locked laser) exhibits a drop at very high offset frequency around a few tens of MHz [34-36], which has never been observed before due to the noise limitation of the electrical measurement system. Until recently, this drop in the phase noise spectrum has been experimentally observed by applying optical cross correlation method [53].

2.4 *Measurement methods for pulse train noise*

There are three main measurement methods for pulse train noise. They are RF spectrum analyzer method, demodulation method and cross-correlation method. In the following sections, these three methods will be discussed respectively.

2.4.1 RF spectrum analyzer method (Von der Linde's method)

D. von der Linde first proposed a model to evaluate the phase noise and the RIN of a pulse train from its RF spectrum [45]. This model is of fundamental importance because it explains how the phase noise and the RIN influence the RF spectrum of a non-ideal pulse train. We briefly introduce von der Linde's model. The ideal pulse train can be expressed in Eq.(2.19)

$$F_0(t) = \sum_n f(t + nT_R) \tag{2.19}$$

where $f(t)$ is the amplitude envelope of a single pulse, T_R is the pulse period. We add timing jitter to $F_0(t)$ and expend to its Taylor series in Eq.(2.20)

$$F(t)=\sum_n f(t+nT_R+\Delta t_n)\approx\sum_n f(t+nT_R)+\sum_n \dot{f}(t+nT_R)\Delta t_n$$
$$=\sum_n f(t+nT_R)+\sum_n \dot{f}(t+nT_R)\,j_nT=F_0(t)+\dot{F}_0(t)J(t)T_R$$

(2.20)

where $\dot{f}=df/dt$, $j_n=\Delta t_n/T_R$ is the relative timing jitter, $J(t)=j_n, t\in(-0.5T+nT, 0.5T+nT)$. Then we add amplitude noise (or RIN) $A(t)$ and yield Eq.(2.21) as follows.

$$F(t)=F_0(t)+\dot{F}_0(t)J(t)T_R+F_0(t)A(t) \tag{2.21}$$

The corresponding PSD of Eq.(2.21) can be proved as

$$P_V(f)=\left|\tilde{H}(f)\right|^2\left|\tilde{f}(f)\right|^2\sum_{k=-\infty}^{+\infty}\left[\delta(f-kf_R)+S_{RIN}(f-kf_R)+4\pi^2k^2S_J(f-kf_R)\right]$$

(2.22)

where $\tilde{H}(f)$ is the system response of detection equipment, $\tilde{f}(f)$ is the Fourier transform of amplitude envelope of single pulse, $\delta(f)$ is delta function in frequency domain induced by periodic pulse train, f_R is the fundamental repetition rate, k is the harmonic number, $S_{RIN}=4\left|\tilde{A}(f)\right|^2$ and $S_J=\left|\tilde{J}(f)\right|^2$ are the power spectrum density of RIN $2\tilde{A}(f)$ and relative timing jitter noise $\tilde{J}(f)$, respectively. Eq.(2.22) can be illustrated in Fig. 2.2 where the definitions of δ_k, I_{Ak} and I_{Jk} are given in Eq.(2.23) and (2.24).

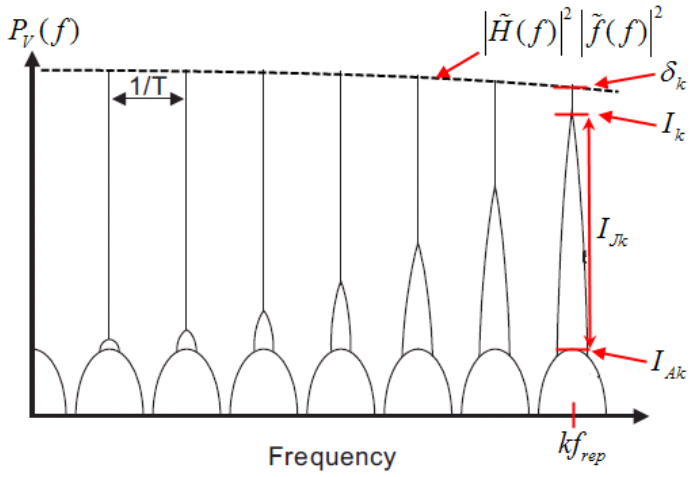

Fig. 2.2 Power spectral density of a noisy pulse train with phase noise and RIN. I_k represents the total noise power at k-th harmonic frequency kf_R including the phase noise power I_{Jk} and relative intensity noise power I_{Ak}

Eq.(2.22) indicates that

a) An ideal periodic pulse chain displays as a chain of delta function $\delta(f - kf_R)$;

b) Intensity noise remains unchanged in fundamental and each harmonic frequency kf_R;

c) Timing jitter noise (or phase noise) increases quadratic with harmonic number k.

The displayed power value at frequency f_i in RF spectrum analyzer is the integration of $P_V(f)$ within a given resolution bandwidth f_{res}, given by Eq.(2.23) where $f_i = kf_R$ and Eq.(2.24) where $f_i \neq kf_R$.

$$\delta_k \equiv \int_{f_i - f_{res}/2}^{f_i + f_{res}/2} P_V(f)df \approx \left|\tilde{H}(kf_R)\right|^2 \left|\tilde{f}(kf_R)\right|^2 \quad (f_i = kf_R) \qquad (2.23)$$

$$
\begin{aligned}
I_k(f_i) &\equiv \int_{f_i - f_{res}/2}^{f_i + f_{res}/2} P_V(f)df \qquad\qquad (f_i \neq kf_R) \\
&\approx \left|\tilde{H}(kf_R)\right|^2 \left|\tilde{f}(kf_R)\right|^2 \left[S_{RIN}(f_i - kf_R) + 4\pi^2 k^2 S_J(f_i - kf_R)\right] f_{res} \\
&\equiv I_{Ak}(f_i) + I_{Jk}(f_i)
\end{aligned}
\tag{2.24}
$$

The relative timing jitter noise PSD $P_J(f)$ (or phase noise PSD $L(f) = 4\pi^2 S_J(f)$) can be extracted by comparing fundamental component and high order component (e.g., 10th harmonics) in Eq.(2.25), where $R_k(f)$, defined in Eq.(2.26), is the relative value in kth component with respect to offset frequency $f \equiv f_i - kf_R$. Relative intensity noise PSD $S_{RIN}(f)$ can be obtained in Eq.(2.27).

$$
L(f) \equiv 4\pi^2 S_J(f) = \frac{R_{10}(f) - R_1(f)}{99 f_{res}} \tag{2.25}
$$

$$
R_k(f) \equiv I_k(f + kf_{rep}) / \delta_k = \left[S_{RIN}(f) + 4\pi^2 k^2 S_J(f)\right] f_{res} \tag{2.26}
$$

$$
S_{RIN}(f) = R_1 / f_{res} - L(f) \tag{2.27}
$$

So the expected timing jitter and relative intensity noise are given by

$$
\left(\frac{\Delta t}{T_R}\right)^2 = \left\langle J^2(t)\right\rangle = \int_{-\infty}^{+\infty} S_J(f)df \tag{2.28}
$$

$$
\Delta t = \frac{1}{2\pi f_R}\sqrt{2\int_0^{f_R/2} L(f)df} \tag{2.29}
$$

$$
\left(\frac{\Delta I}{I}\right)^2 = 4\left\langle A^2(t)\right\rangle = 2\int_0^{f_R/2} S_{RIN}(f)df \tag{2.30}
$$

The unit of $S_J(f)$ is 1/Hz and the unit of $L(f)$ is rad^2/Hz. $L(f)$ will sometimes be described by logarithmic scale in the units of dBc/Hz where dBc

represents the relative power to the carrier. Many researchers have further developed this method and given more general interpretation of the relation between the RF spectrum and the noise of the pulse train [31, 37-38, 40]. The RF spectrum analyzer method fully utilizes the information at each harmonic frequency in RF spectrum and is a method specially designed for the noise measurement of a pulse train. However, the drawback of the analyzer method is that a large portion of the dynamic range of the spectrum analyzer is occupied by the carrier power and therefore only a very small portion of the dynamic range is left for noise measurement (below the dynamic range is the noise floor of the RF spectrum analyzer). Therefore the noise floor of the measurement system is usually quite high for RF spectrum analyzer method.

2.4.2 Demodulation method

Another important method is the demodulation method which is widely used in signal processing and H. Tsuchida first adopted it to measure the noise of a pulse train [51] and later R. P. Scott provided a detailed description of this method [46]. This method is now widely used by the commercial signal source analyzers (SSA), e.g., Agilent E5202B [54] and Rohde & Schwarz FSUP26 [55], to measure the phase noise and RIN of a periodic signal.

Here we briefly introduce the mathematical background of the demodulation method. It should be mentioned first that the demodulation method is designed for measuring the noise of electrical signal with single carrier frequency (not like pulse train which has many frequency components in the RF spectrum). Suppose the input electrical signal is given in Eq.(2.31)

$$V_{in} = (1+\Delta a)\cos(\omega_0 t + \Delta\varphi) = (1+\Delta a)\cos[\omega_0 (t+\Delta t)] \tag{2.31}$$

where $\omega_0 = 2\pi f_R$ is the carrier angular frequency, Δa is the relative intensity noise, $\Delta\varphi$ is the phase noise of the carrier frequency (for laser that is repetition rate) and $\Delta t = \Delta\varphi / \omega_0$ is the timing jitter. We do not use Eq.(2.20) because that equation is to model the noise of a pulse train whereas here we model the noise of a single carrier frequency. To measure the phase noise, we generate a local oscillation with same frequency and $\pi/2$ delay, that is $\cos(\omega_0 t + \pi/2) = -\sin(\omega_0 t)$. This local oscillation signal is mixed with the input signal and the low frequency part after mixing is filtered out with a low pass filter, see Eq.(2.32)

$$\begin{aligned} V_{mix} &= K(1+\Delta a)\cos(\omega_0 t + \Delta\varphi)\cdot(-\sin\omega_0 t) \\ &= K/2\cdot(1+\Delta a)[\sin\Delta\varphi - \sin(2\omega_0 t + \Delta\varphi)] \\ &\quad filter + amplifier \Rightarrow (1+\Delta a)\sin\Delta\varphi \approx \Delta\varphi \end{aligned} \tag{2.32}$$

Thus the phase noise is obtained. This process is illustrated in Fig. 2.3 (a).

To measure the RIN, one method is to downconvert the signal to an intermediate frequency ω_{IF} and then split the signal into two paths and multiply together to realized self-mixing. In this case, the measured noise is $2\Delta a$, see Eq.(2.33) and Fig. 2.3 (b).

$$\begin{aligned} V_{mix} &= K(1+\Delta a)^2\cos^2(\omega_{IF} t + \Delta\varphi) \\ &= K/2\cdot(1+\Delta a)^2[1+\cos(2\omega_{IF} t + 2\Delta\varphi)] \\ &\quad filter + amplifier \Rightarrow (1+\Delta a)^2 \approx 1+2\Delta a \end{aligned} \tag{2.33}$$

An even simpler method is to consider RIN as a weak amplitude modulation (AM) at a certain carrier frequency. Then the RIN can be extracted by a standard AM envelope demodulator which is a diode cascaded by a grounded capacitor, as

shown in Fig. 2.3 (c). But this method is not suitable to measure the RIN of a pulse train because the pulse duration is usually too short to fully charge the capacitor to the target voltage.

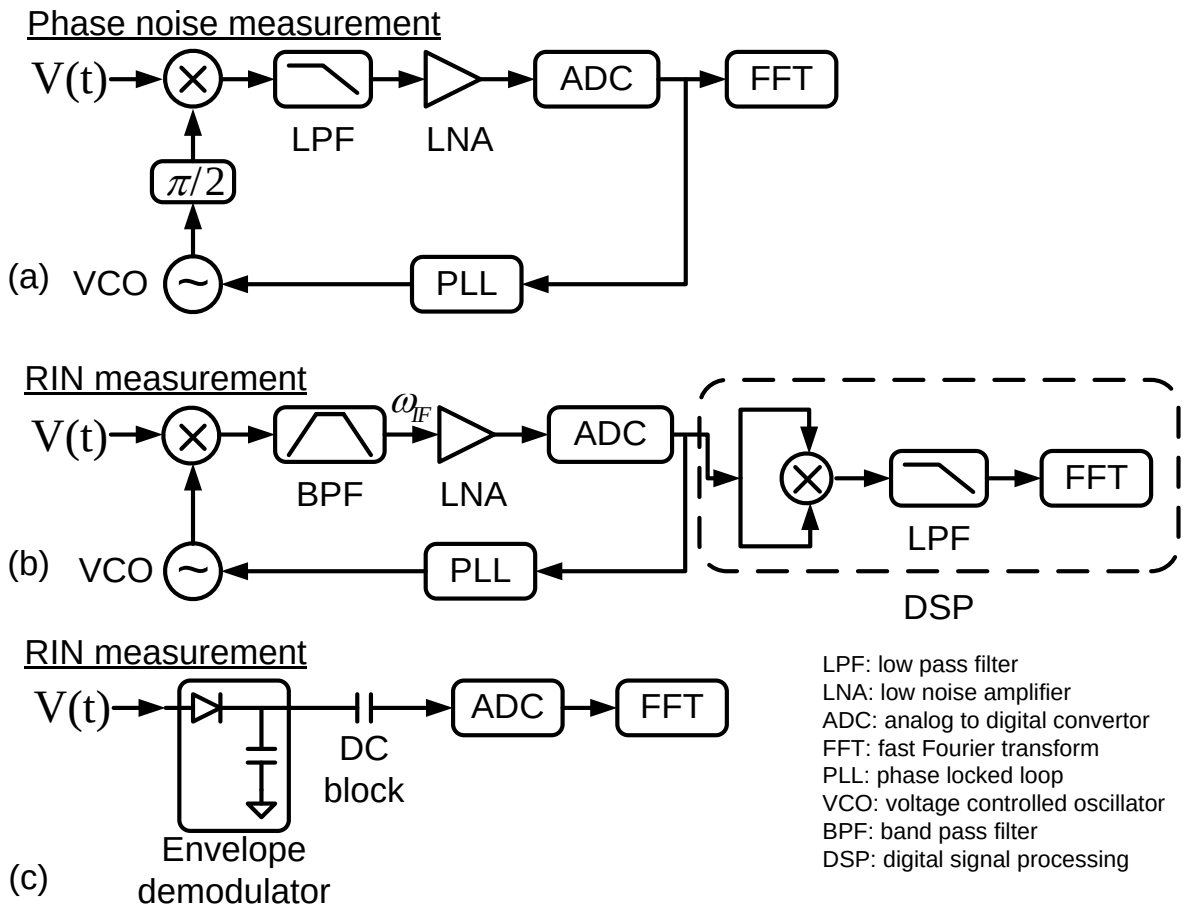

Fig. 2.3 Measurement setup for (a) phase noise with phase locked loop (b) RIN with phase locked loop and self mixing and (c) RIN with envelope demodulator

Demodulation method effectively suppresses the carrier power by using phase locked loop (PLL) to generate a local oscillation and downconvert the target signal to the baseband (typically from DC to a few tens of MHz). Due to the suppression of the carrier power, the whole dynamic range of the analyzer can be used to measure the noise power and the precision baseband measurement can be easily done with a low speed sampling system. However, this method is originally

designed for sine wave signal. For a pulse train contains many harmonic frequency components, the PLL cannot work properly unless a filter is applied before the signal entering the measurement system to filter out one harmonic frequency. Due to the analysis given in the RF spectrum analyzer method, one can find that timing jitter and RIN of the pulse train can be measured at any harmonic frequency.

2.4.3 Cross-correlation method

The third method of noise measurement is cross-correlation method. For the demodulation method we have previously discussed, it suffers from the electrical noise limitation set by the shot noise and the thermal noise due to its low RF power from the photodetector. This leads to a minimum noise floor in the phase noise PSD at around -160 dBc/Hz [14]. Cross-correlation method can overcome this problem because it measures the phase noise in optical domain and thus its noise floor in the phase noise PSD is set by the optical shot noise which can be as low as -200 dBc/Hz [53]. A traditional optical cross-correlation method was discussed in Jiang's work [43]. Here we briefly introduce this method. Jiang's setup is shown in Fig. 2.4 (a). A mode-locked laser generates a pulse train under test. The pulse train is then split into two paths. One path introduces a time delay of T equals to N pulse periods. The two pulse trains meet together and generate second harmonic signal through a nonlinear crystal. The second harmonic signal is finally sent to a photo multiplier tube (PMT) for measurement. The translation stage is to scan the cross-correlation trace. This setup is very similar to an autocorrelation (AC) measurement setup except for a fix time delay of T. The principle of such a measurement is that by introducing delay in one path 1st pulse interacts with N-th pulse at nonlinear crystal and generates a signal containing the information of pulse-to-pulse jitter. Fig. 2.4 (b) illustrates this

process. The autocorrelation trace of the original pulses has the smallest pulse width. The AC trace of the pulses after delay is wider due to the pulse broadening induced by fiber dispersion. The cross-correlation trace is even wider due to the existence of pulse-to-pulse timing jitter.

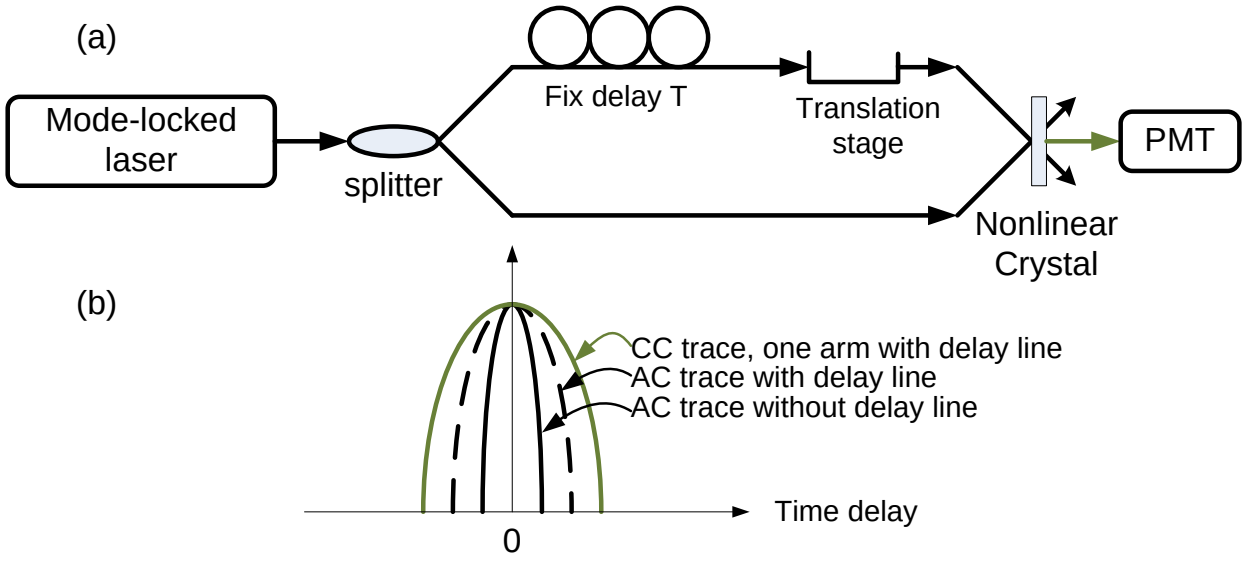

Fig. 2.4 (a) Experimental setup of Jiang's cross-correlation (CC) method; (b) Measured autocorrelation (AC) and CC traces

The mathematical analysis is given as follows: suppose the original relative timing jitter in time domain is $J(t)$, the cross-correlation setup generates a new jitter expression in time domain $\Delta J(t) = J(t) - J(t-T)$. Its autocorrelation function is given by

$$\begin{aligned} G_{\Delta J}(T) &= \langle \Delta J(t) \Delta J(t-T) \rangle \\ &= 2G_J(T) - G_J(t-T) - G_J(t+T) \end{aligned} \tag{2.34}$$

The power spectral density is the Fourier transform of the autocorrelation function and is given by

$$S_{\Delta J}(f) = 2(1-\cos 2\pi fT) S_J(f) \tag{2.35}$$

The root-mean-square (RMS) timing jitter is given by

$$\Delta t^2 = \int_{-\infty}^{+\infty} S_{\Delta J}(f)df = \int_{-\infty}^{+\infty} 2(1-\cos 2\pi fT)S_J(f)df \tag{2.36}$$

Since cosine function approaches to 1 when T is close to 0, the cross-correlation measurement is not accurate for small T. Usually, the cross-correlation measurement measures the timing jitter faster than 1/(4T), or equivalently the integration region in Eq.(2.36) is 1/(4T) to infinity. The RMS timing jitter is linked to the measurement results by

$$\Delta t^2 = \sigma_{CC}^2 - \sigma_{AC}^2 \tag{2.37}$$

where σ_{CC}^2 and σ_{AC}^2 are the standard deviations of the cross-correlation and averaged autocorrelation traces. However, Eq.(2.37) is only valid for Gaussians pulses and Gaussian timing jitter probability density function and has error for other pulse profiles [43].

Later Kartner and Kim invented an improved setup called balanced optical cross-correlation [44, 53, 56]. This setup linearly maps the timing jitter between two input pulses with orthogonal polarization to voltage which can be easily analyzed with electrical equipment. With this jitter-to-voltage mapping, the timing jitter PSD can be easily obtained by measuring the PSD of the voltage from the balanced optical cross-correlation. In this way, the noise floor originally set by the electrical shot noise and thermal noise can be replaced by the optical shot noise which can be as low as < -200 dBc/Hz [53]. Also, by using two mode-locked lasers with almost the same design, we can avoid the usage of a long delay line to decorrelate the pulses in the two arms at the cost of a more complicated setups [56].

We would like to give a summary of three methods of noise measurement as follows

Table 2.2 Summary of three methods of noise measurement

	RF spectrum analyzer method	Demodulation method	Cross-correlation method
Setup	Very simple, only requires an RF spectrum analyzer	Slightly complicated, but there are commercial products available	Complicated, especially when using two almost same mode-locked lasers to avoid using a long delay line
Accuracy	Not very accurate due to limitation of theory, e.g., neglecting the correlation between RIN and phase noise	Accurate at low-offset frequency; the accuracy is dependent on the noise of the internal microwave oscillator	Quite accurate, only limited by the linearity of the balanced cross correlator
Noise floor	Dependent on the noise floor of the RF spectrum analyzer; Usually quite high >-140 dBc/Hz	Dependent on the electrical shot noise and thermal noise; Usually around -160 dBc/Hz	Dependent on the optical shot noise; Very low, usually below -200 dBc/Hz
Frequency range	From a few hertz (limited by the minimum resolution bandwidth of the analyzer) to a few hundred kilo-hertz (limited by the noise floor of the analyzer)	From very low frequency (dependent on the stability of the internal microwave oscillator) to a few tens / hundreds of mega-hertz (limited by the noise floor)	From a few kilo-hertz (could be even smaller when using two almost same mode-locked lasers to avoid using a long delay line) to Nyquist frequency

In short, RF spectrum analyzer method has the simplest setup only requiring an RF spectrum analyzer but also has low accuracy, high noise floor and limited frequency range. Demodulation method has slightly complicated setup but provides much better accuracy and lower noise floor as well as large frequency range. Cross-correlation method requires a dedicated setup for each measurement but can provide unprecedented low noise floor as well as good accuracy and large frequency range. All these three methods are being widely used in the present work due to their different advantages described above.

It is also worth mentioning how the integration frequency range for timing jitter and RIN calculation is chosen. The main considerations are 1) The range should cover the main structures in the noise spectra and 2) The contribution to the integration from the part outside the chosen frequency range should be small compared with that from inside the chosen frequency range. All the choice of frequency ranges in the thesis is based on this principle.

2.5 *Summary*

In summary, we first briefly introduce the definition of relative intensity noise and phase noise (timing jitter). Then we review the development of the theory of quantum noise of the mode-locked lasers. Haus's model was first proposed and originally used for describing the quantum noise of soliton mode-locked lasers. Namiki, Jiang, Menyuk and Pashotta have developed this model to describe the noise of any type of mode-locked lasers with no requirement of soliton operation and to analyze the laser phenomena such as relaxation oscillation and frequency pulling. Finally, we introduce and compare the three methods of noise measurement. RF spectrum analyzer method is most convenient but less accurate. This method can

only give some information of the strength of the noise but is inaccurate for detailed noise measurement. Demodulation method is most widely used method due to its slightly complicated setup but much more accurate measurement results than the RF spectrum analyzer method. But this method has a noise floor around -160 dBc/Hz due to the electrical shot noise and thermal noise. The balanced cross correlation method can measure to a very low noise floor as low as -200 dBc/Hz, but requires a complicated setup. Its accuracy is dependent on the linearity of the balanced cross correlator when mapping timing jitter to voltage.

3 Noise suppression of the mode-locked lasers

3.1 *Review on the technologies for laser noise reduction*

Based on the researches of laser noise, many techniques have been developed to obtain low-noise operation for the mode-locked laser. Most of these technologies are based on Haus and Meccozi's model and the others are based on some new devices. We briefly review some of these techniques as follows.

In 2002, Jiang *et al.* investigated the effect of intra-cavity filter in an actively mode-locked semiconductor laser. He achieved 47 fs (10 Hz-10 MHz) timing jitter by inserting 0.7nm band pass filter to limit Gordon-Haus jitter [33]. According to Haus and Meccozi's model, the frequency noise (random shift of central wavelength) will couple to the phase noise via dispersion. This coupling can be suppressed by inserting a band pass filter to enhance the cavity recovery force (τ_w^{-2}).

In 2007, Gee *et al.* utilized a specially designed slab coupled optical waveguide amplifier (SCOWA) as gain media in an actively mode-locked laser [50]. He discussed the combined effect of intra-cavity filter and feedback loop. When filter was removed from the cavity, the feedback loop worked better and suppressed the noise at low offset frequency greatly, which suggests that the effect of feedback loop and intra-cavity filter may conflict with each other. Gee achieved sub-femtosecond 0.66 fs jitter (0.9 Hz - 1 MHz).

In 2008, Jian Chen *et al.* studied the noise performance of pulse multiplication from a seed mode-locked laser [49]. Chen *et al.* used a 200MHz passively mode-locked laser as a seed laser. The 200MHz pulse train injected into a Fabry-Perot Filter whose transmission characteristic is a frequency comb structure.

Thus 200MHz is multiplied to 2GHz. A feedback loop is designed to control the repetition rate of seed laser. In the figure of RIN spectral density it can be clearly seen that the noise at low offset frequency has been suppressed. Chen achieved 27fs (1kHz-10MHz) timing jitter and 0.27% relative intensity noise (0.01Hz-10MHz).

In 2009, Prochnow *et al.* investigated the phase noise in an all-normal-dispersion cavity operating at 1060nm [57]. The cavity structure was complex and his experiment indicated that Haus and Meccozi's theoretical model would underestimate the quantum noise of the laser in this kind of cavity but Paschotta's simulation method worked well. This laser also operated at a quantum-noise-limit condition. The timing jitter of this laser is 90 fs (100 Hz – 10 kHz).

3.2 *Timing jitter reduction by optimization of cavity loss*

It is generally believed that a low cavity loss would result in low phase noise and timing jitters because of the reduction of spontaneous emission. However, when we look into Haus and Mecozzi's quantum noise model in Eq.(2.8), we find that the phase noise or timing jitter can be minimized by properly increasing cavity loss. The experimental observations support the theoretical prediction.

3.2.1 Theoretical analysis

Haus and Mecozzi's model in Eq.(2.8) is used for analysis. For the convenience of reading, we give again Eq.(2.8) as follows in Eq.(3.1). The meaning of all the notations is the same as Eq.(2.8).

$$L(f) = (2\pi f_R)^2 \left[\frac{D^2 D_p}{T_R^2} \frac{1}{(2\pi f)^2((2\pi f)^2 + \tau_p^{-2})} + \frac{D_t}{(2\pi f)^2} \right]$$

$$= (2\pi f_R)^2 \left[\frac{1}{(2\pi f)^2} \frac{4D^2 \theta h\nu}{3T_R^3 w_0 \tau^2} \frac{g}{(2\pi f)^2 + \frac{4g^2}{9\pi^4 T_R^2 \Delta f_g^4 \tau^4}} + \frac{1}{(2\pi f)^2} \frac{\pi^2 \tau^2 \theta h\nu}{3 w_0 T_R} g \right] \tag{3.1}$$

As discussed before, this equation indicates two mechanisms describing how spontaneous emission couples to timing jitter. The first term represents an indirect contribution to timing jitter coupled from the random shift of center frequency caused by spontaneous emission via group velocity dispersion. The second term represents a direct contribution to timing jitter (random shift of pulse position) caused by spontaneous emission. For high frequency region, first term in the square bracket decreases by a factor of f^{-4} because f^2 in the denominator is much greater than τp^{-2} and second term decreases by a factor of f^{-2}. Therefore, second term dominates at high frequency region and the phase noise spectrum exhibits a trend of f^{-2} decrease. For low frequency region, first term is dominant and decreases by f^{-2} when the dispersion is not very small. Moreover, at low frequency region, first term is inversely proportional to the gain coefficient g and second term is proportional to g. Therefore phase noise spectrum decreases when g increases. But the relation between g and phase noise spectrum at low frequency region is not monotone. When g further increases, the difference between first term and second term is reduced by a factor g^2. This means the values of first term and second term will finally become comparable and phase noise spectrum will no longer decrease with the increase of g.

For a steady operating mode-locked laser, gain compensates the cavity loss per round trip e^g(1-loss)=1. Therefore increasing cavity loss is equivalent to

increasing cavity gain per round trip as long as mode locking state is maintained. Considering that increasing cavity loss may also affect output power, total cavity energy, bandwidth and pulse duration. The relation of timing jitter and cavity loss could be even more complicated than a first-decrease-later-increase result in some cases.

In our calculation with Haus and Meccozi's model, gain bandwidth Δf_g is equal to 20nm. Output powers are measured in the experiments as -6.6dBm, -6.9dBm, -8.0dBm and -7.9dBm for 0dB, 1dB, 2dB and 3dB additional intracavity attenuation, respectively. In practical experiment, this tunable intracavity loss can be applied by inserting a tunable attenuator in the cavity. The calculated timing jitter is shown in Fig. 3.1. More details of the parameter values can be found in the next section of experimental setup. It can be seen that there is a minimum timing jitter at certain cavity loss.

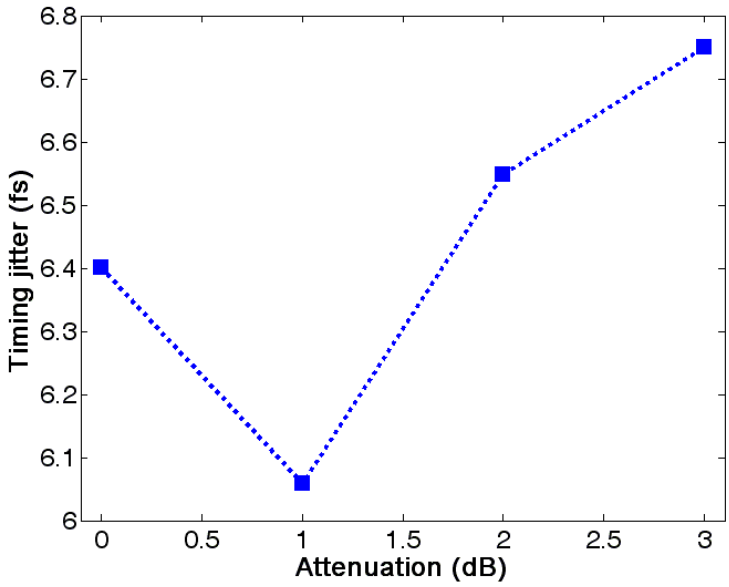

Fig. 3.1 Calculated timing jitters according to Haus and Meccozi's model with the integration region of 100 Hz ~ 20 kHz. The gain bandwidth Δf_g is equal to 20 nm. The output powers are -6.6 dBm, -6.9 dBm, -8.0 dBm and -7.9 dBm for 0 dB, 1 dB, 2 dB and 3 dB additional intracavity attenuation, respectively

`

3.2.2 Experiment

The experimental setup is a typical passively mode-locked fiber laser as shown in Fig. 3.2. Using ES1 transition in single wall carbon nanotubes (SWCNTs), SWCNTs can behave as a saturable absorber, i.e., pulse peak with high instant intensity experiences lower loss than pulse wing with low instant intensity [58]. Also the low saturation intensity of SWCNTs ensures the low self starting power of mode locking. In our experiment, the SWCNTs are embedded in a new type of polymer film called carboximethyl cellulose (CMC) [59]. The film is cut into small pieces and then manually put on the fiber end with tweezers, as shown in the inset of Fig. 3.2. SWCNTs enable very low self starting threshold for pump power, typically 18~28 mW in our laser. The total cavity loss without additional attenuator is estimated to be ~3.3 dB. The total cavity length is ~10.6 m and the corresponding fundamental repetition rate is ~18.8 MHz. The length of single mode fiber is ~7 m with dispersion -0.02 ps^2/m. The length of Erbium doped fiber is ~3.6m with dispersion 0.01 ps^2/m. Thus the total dispersion is ~ -0.1 ps^2. A RF spectrum analyzer (R&S FSUP26, which is also a signal source analyzer) is used to measure the phase noise spectrum of output pulse train from passively mode-locked laser after optical-electrical conversion by a 2 GHz photodetector. To guarantee the measurement accuracy of the noise spectrum, the offset frequency range (100 Hz – 20 kHz) is chosen so that the laser noise is well above this noise floor induced by the RF spectrum analyzer.

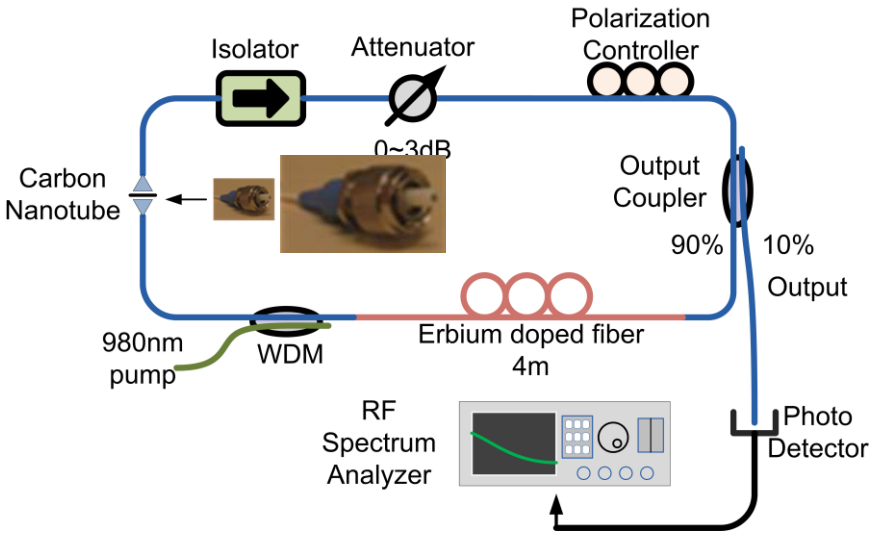

Fig. 3.2 Experimental setup of passively mode-locked fiber ring laser. Inset: photo of carbon nanotube film on the fiber connector end

The experimental results are shown in Fig. 3.3 (a) when different additional attenuation is added into the laser cavity. The RF spectrum analyzer has a noise floor around -118 dBm at a resolution bandwidth of 30 Hz. It can be seen that all four curves exhibit -20dB/decade decrease at higher frequency (e.g., f > 8 kHz), which is a typical characteristics of mode locked lasers [44, 57]. When a 1 dB fixed attenuator is added into the cavity, the phase noise spectrum (red dotted line) decreases at lower frequency region and increases at higher frequency region, compared with the original curve (black solid line). If we further increase the attenuation to 2 dB, the phase noise spectrum (green solid line) decreases more at lower frequency region and increases more at higher frequency region. When the total additional attenuation increases to 3 dB, the phase noise spectrum (magenta dashed line) behaves differently. The phase noise at lower frequency region increases and phase noise at higher frequency region remain nearly unchanged compared with the 2 dB attenuation case. This change indicates that further increase cavity loss by adding more additional attenuation will not help to improve the phase

noise. Moreover, the laser can hardly be mode locked if the additional attenuation is greater than 3 dB. The calculated timing jitters using Eq.(3.2) are shown in Fig. 3.3 (b).

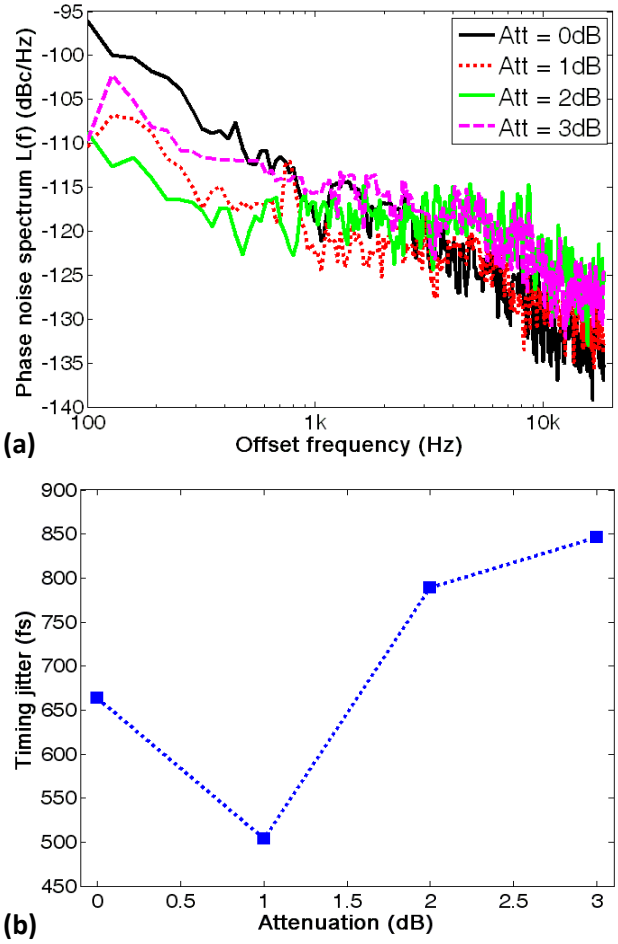

Fig. 3.3 (a) Phase noise spectrum with respect to different additional attenuation added into the cavity; (b) calculated timing jitters according to (a) with integration range of 100 Hz ~ 20 kHz

$$\Delta t = \frac{1}{2\pi f_R}\sqrt{2\int_0^{f_R/2} L(f)df} \tag{3.2}$$

The experimental results shown in Fig. 3.3(a) are obtained with polarization controller remaining unchanged when different attenuators are added. Output powers are -6.6 dBm, -6.9 dBm, -8.0 dBm and -7.9 dBm for 0 dB, 1 dB, 2 dB and 3 dB attenuation, respectively. Since the intra-cavity power is reduced due to higher

cavity loss, the nonlinear effect is weaker and hence phase delay in the cavity has been changed. This means the laser may have been detuned from its most stable mode-locked state. By adjusting the cavity birefringence induced by polarization controller, the change of phase delay can be compensated and a most stable state can be achieved (usually the state with lowest mode locking threshold). Following this understanding, a few mode-locked states are measured at each value of attenuation. The best results are summarized in Fig. 3.4 (a) for each cavity loss. The corresponding pump powers are 18 mW, 23 mW, 28 mW and 28 mW for 0 dB to 3 dB attenuation, respectively. These powers are to maintain the best mode locking state for each cavity loss. Very similar behaviors of curves can be seen compared with those in Fig. 3.3 (a). The calculated timing jitters and corresponding optical spectrums are shown in Fig. 3.4 (b) and Fig. 3.5, respectively.

It can be seen that the timing jitters for 2 dB and 3 dB attenuation cases have been improved. The minimum timing jitter is obtained at 1 dB attenuation, which is 24% smaller than the value at 0 dB attenuation. The spectral shifts in Fig. 3.5 are due to two main reasons. The first is the drift of gain window. It is well known that the gain window in a laser cavity will drift to shorter wavelength when the cavity loss is high due to the weaker re-absorption of the emitted light. The second is the balance of phase delay. When the cavity loss is higher, the pulse energy is lower and the phase delay caused by the nonlinearity is also lower. To balance the reduced phase delay, the dispersion induced phase delay should also be lower. The single mode fiber has a smaller dispersion at shorter wavelength so the mode locking spectra moves to a shorter wavelength.

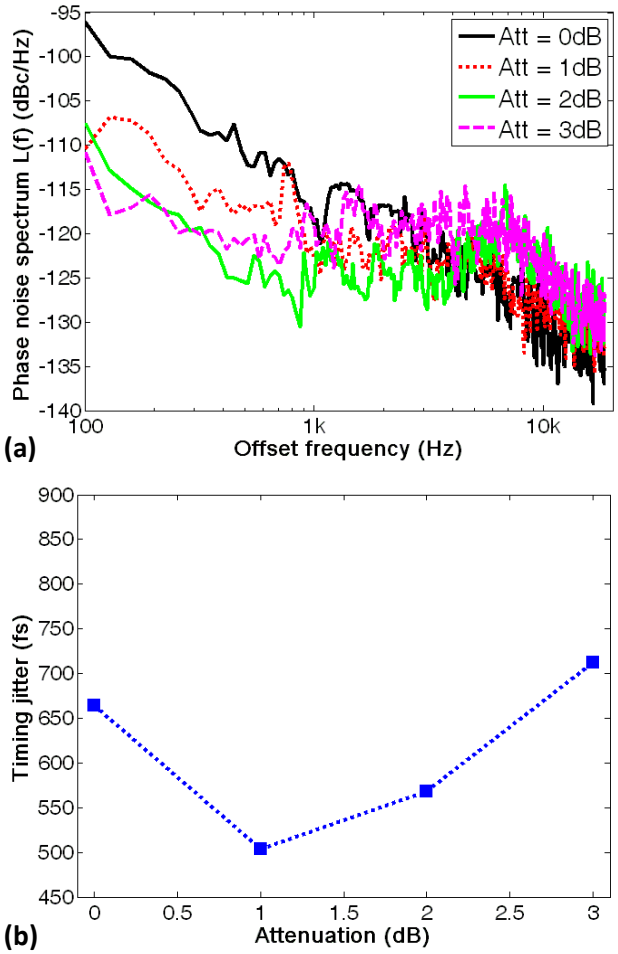

Fig. 3.4 (a) Best results of phase noise spectrum with respect to different additional attenuation added into the cavity; (b) calculated timing jitter according to (a) with integration range of 100 Hz ~ 20 kHz

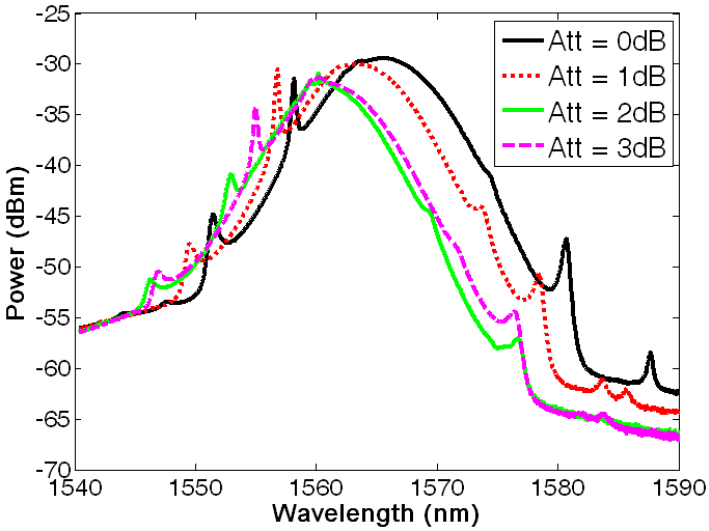

Fig. 3.5 Optical spectra with respect to different additional attenuation added into the cavity when best timing jitters are obtained by adjusting polarization controller

It is also worth mentioning that in our experiment, better operation stability does lead to better timing jitter because the best results shown in Fig. 3.4 are all obtained when the mode locking threshold is the lowest among a few possible mode locking states. The relative intensity noise (RIN) is also considered as shown in Fig. 3.6. It can be found that the RIN only increases 4% at 1 dB attenuation compared with the value at 0 dB attenuation. The peaks around 7-9 kHz of the curve at 2 dB and 3 dB attenuation cases are due to the relaxation oscillation associated with continuous wave (CW) background emission near 1560 nm in the spectrum [60]. The noise reduction at low offset frequency can also be observed similar to what has been observed in the phase noise spectra.

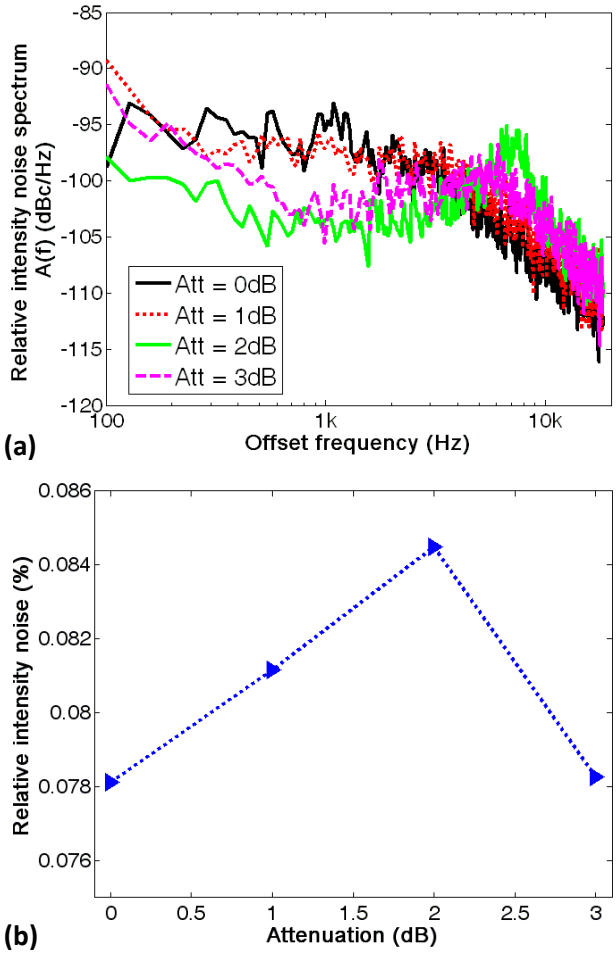

Fig. 3.6 (a) Relative intensity noise spectrum with respect to different additional attenuation when best phase noise performance is obtained in Fig. 3.4; (b) calculated RIN according to (a)

3.2.3 Discussion

Although very similar behaviors are found between the measured timing jitter values and the theoretically predicted values with respect to different cavity loss, discrepancy does exist. We find this is mainly due to the coupling from intensity noise to timing noise. By comparing the value of relaxation peak in the phase noise spectrum L(f) (at ~8 kHz in 2 dB curve in Fig. 3.4 (a) and that in the relative intensity noise spectrum A(f) (at ~8 kHz in 2 dB curve in Fig. 3.6 (a)), we find that there is a roughly -22 dB coupling ratio from A(f) to L(f). If we subtract the part generated by this coupling in the phase noise spectrum, the newly calculated timing jitter is 446 fs, 102 fs, 344 fs, 573 fs with respect to 0 dB, 1 dB, 2 dB, 3 dB cases. Another reason is the noise factor induced by Erbium doped fiber. Ref. [61] claimed that EDFA can easily contribute a noise factor of 5 under saturation conditions. Compared the EDF used in Ref.[61], our EDF provides even higher gain due to the higher cavity loss. Therefore the spontaneous emission from the EDF must be stronger than that in Ref.[61] and it is reasonable to consider a noise factor of 10 induced by our EDF used in the laser. For Haus and Meccozi's model, there have been a few reports showing that it sometimes may underestimate the timing jitter by ~10 dB in the phase noise spectrum. For example in Ref.[57], the laser setup had the comparable complexity with ours but the Haus and Meccozi's model under estimated the phase noise by ~10 dB. Therefore, we estimate that Haus and Meccozi's model causes similar underestimation in our laser and leads to another factor of 3~5 in timing jitter calculation.

However, when we want to further verify our observation in a laser mode locked with nonlinear polarization rotation (NPR), we find NPR based mode locking is much more sensitive to the cavity loss compared with SWCNT based mode

locking. NPR-based mode locking technique exploits the fiber Kerr nonlinearity to realize an artificial saturable absorber effect with a polarization dependent element in the laser cavity. Thus, the artificial saturable absorber is highly dependent on the pulse power and the intra-cavity loss greatly weakens the mode-locking mechanism of NPR. In our typical experiment, we used 1.5 m LIEKKI Er110 Erbium doped fiber (peak absorption at 1530 nm is 110 dB/m) and 9.6 m single mode fiber to configure a NPR-based passively mode-locked fiber laser. When all components were connected by splicing, the best timing jitter of fundamental mode-locking pulse was 559 fs with repetition rate of ~18 MHz. When we increased the intra-cavity loss of 0.4~0.5 dB by inserting an adaptor, the laser can hardly be mode locked with our 300 mW 976 nm pump and the mode-locking state, even obtained, was very unstable and couldn't be measured noise properties. So our observation by changing cavity loss may not be valid to the NPR based mode-locked laser.

It is also worth mentioning that it has been already known that passively mode-locked lasers are likely to have much smaller timing jitter (a few tens of fs) when the cavity net dispersion is close to zero. In out experiment, the cavity net dispersion -0.1 ps2 which is sufficiently large considering the dispersion of standard single mode fiber of -0.022 ps2. The purpose of our work is to demonstrate that by optimizing the cavity loss, the frequency jitter to timing jitter coupling via cavity dispersion can be minimized and leads to reduced timing jitter, which is predicted by Haus and Meccozi's model but has never been experimentally demonstrated before.

3.2.4 Summary

In conclusion, we experimentally demonstrate that the phase noise and timing jitter of a passively mode-locked fiber ring laser with carbon nanotube saturable absorber

can be improved by optimizing the cavity loss, due to the fact that higher cavity loss is helpful to suppress the coupling from random shift of central frequency caused by spontaneous emission to timing jitter. Although the phase noise spectrum at high frequency range tends to increase with the increase of cavity loss, the contribution to the integrated timing jitter is quite limited because of its quick decrease with a slope of -20 dB/decade. Further increasing cavity loss would make phase noise spectrum increase both at low frequency region and high frequency region simply because the direct coupling from spontaneous emission to random shift of pulse position in time domain becomes dominant. However our observation may not be valid for the mode locked lasers based on fiber nonlinearity, e.g. NPR-based lasers and figure 8 lasers, due to the high sensitivity to cavity loss of the mechanism of artificial saturable absorber. In our experimental results, the timing jitter has been reduced by 24% and another important noise, relative intensity noise has only been increased by 4%.

3.3 *Noise reduction by feedback control of laser repetition rate*

3.3.1 Drift of repetition frequency of mode-locked fiber lasers

As we have known, for fundamentally passively mode-locked fiber lasers, the period of the output pulse train equals to the round trip time of the cavity or $n_{eff}L$, where n_{eff} is the effective group refractive index and L is the physical length of the cavity fiber. Unfortunately, due to the disturbance from the temperature fluctuation, air flow, mechanical vibration and etc., neither n_{eff} nor L is stable with time and therefore the repetition frequency of a passively mode-locked fiber laser is not stable. We can define a fractional frequency instability as $\Delta f_R / f_R$ where f_R is the repetition frequency and Δf_R is the deviation of repetition frequency at a given

observation time. Now we provide a simple analysis on the value of fraction instability.

Since the repetition frequency is given by

$$f_R = \frac{c}{n_{eff} L} \tag{3.3}$$

The fractional instability is given by

$$\frac{\Delta f_R}{f_R} = \frac{\Delta(n_{eff} L)}{n_{eff} L} = \frac{\Delta n_{eff}}{n_{eff}} + \frac{\Delta L}{L} \tag{3.4}$$

The fractional instability induced by temperature fluctuation is given by

$$\frac{\Delta f_R}{f_R} = \left(\frac{1}{n_{eff}} \frac{\partial n_{eff}}{\partial T} + \frac{1}{L} \frac{\partial L}{\partial T} \right) \Delta T \tag{3.5}$$

For silica fiber, the thermo-optic coefficient is given by [62]

$$\frac{1}{n_{eff}} \frac{\partial n_{eff}}{\partial T} \approx 7.5 \cdot 10^{-6} / °C \tag{3.6}$$

And the thermal expansion coefficient of doped silica is given by [63]

$$\frac{1}{L} \frac{\partial L}{\partial T} \approx 0.55 \sim 1.5 \cdot 10^{-6} / °C \tag{3.7}$$

Therefore temperature induced instability is given by

$$\frac{\Delta f_R}{f_R} \approx 10^{-5} \Delta T \tag{3.8}$$

In a lab environment, temperature drift is usually less than 5 degrees. Similarly, fractional frequency instability induced by pressure is given by [64]

$$\frac{\Delta f_R}{f_R} = \left(\frac{1}{n_{eff}} \frac{\partial n_{eff}}{\partial P} + \frac{1}{L} \frac{\partial L}{\partial P} \right) \Delta P \tag{3.9}$$

The pressure induced physical length change is given by

$$\frac{1}{L} \frac{\partial L}{\partial P} = -\frac{1-2\mu}{E} \approx -9.4 \cdot 10^{-12} / Pa \tag{3.10}$$

where $\mu = 0.17$ is Poisson's ratio and $E = 7 \cdot 10^{10} Pa$ is Young's modulus. The pressure induced index change is given by [64]

$$\frac{1}{n_{eff}} \frac{\partial n_{eff}}{\partial P} = \frac{n_{eff}^2}{2E} (1-2\mu)(2p_{12} + p_{11}) \approx 6.7 \cdot 10^{-12} / Pa \tag{3.11}$$

where $p_{11} = 0.121$ and $p_{12} = 0.27$ are the components of strain-optic tensor. Therefore pressure induced instability is given by

$$\frac{\Delta f_R}{f_R} \approx 10^{-12} \sim 10^{-11} \Delta P \tag{3.12}$$

In a labobatory environment, the pressure drift is usually less than 10 Pa, which means the effect of pressure drift is much weaker than that of temperature drift. Therefore temperature fluctuation is the main source for the frequency instability. The feedback control scheme applied should be able to compensate this frequency deviation. The most common way is to apply a piezoelectric transducer (PZT) to mechanically stretch the fiber.

3.3.2 Feedback control scheme

A feedback control scheme is applied to track the output of a certain system with respect to a reference. A typical feedback control scheme is given in Fig. 3.7.

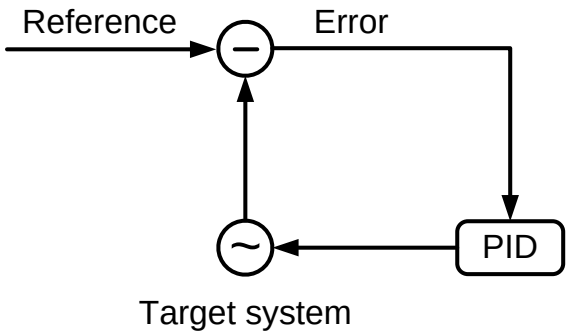

Fig. 3.7 A typical feedback control scheme

The output of the target system is compared with a reference and an error signal is then generated and used to control the output of the target system until the error goes to zero. Usually Proportional–Integral–Derivative (PID) method is applied to control the target system with respect to the error signal. Suppose the error ε is the difference between the output of the target system and the reference, the output of a PID controller is given by

$$Output = K_P \varepsilon + K_I \int \varepsilon dt + K_D \frac{d\varepsilon}{dt} + offset \tag{3.13}$$

where K_P, K_I and K_D are the coefficients of proportional, integral and derivative terms respectively. A larger proportional coefficient K_P leads to a faster tracking of the error evolution but also higher overshoot and reduced stability, i.e., the system is easier to oscillate. Moreover if only proportional control is applied there exists a steady-state error due to the drift of the system with time. A larger integral coefficient K_I has similar effect of a larger K_P but can significantly reduce the steady-state error of the system. A larger derivative coefficient K_D with proper feedback loop delay increases the stability of the system but also increases the noise

due to the derivative calculation. For simplicity, we use proportional and integral (PI) control in our feedback control system.

Piezoelectric transducer (PZT) is usually applied to control the fiber length in the laser cavity. A piezoelectric material is a kind of materials that accumulate electrical charges in response to external mechanical strain or pressure applied which corresponds to a change of volume, area or length of the material. This piezoelectric effect is bi-directional. That means, if a voltage is applied, the piezoelectric material can change its volume, area or length accordingly. PZT is based on this principle. One of the most common types of fiber stretcher is made by winding fiber on the outside wall of a PZT tube which is a thin-walled tube made by piezoelectric material and can radial expand or contract when a voltage difference is applied onto the inside and outside faces of the wall. The radial displacement (expansion or contraction) is the result of the superposition of increase in the tangential contraction and wall thickness, given by

$$\frac{\Delta r}{r} = d_{31}\frac{V}{d} \tag{3.14}$$

where Δr is the displacement of the radius r of the PZT tube, $d_{31} \approx 3\cdot 10^{-10} m/V$ is the strain coefficient, d is the wall thickness and V is the voltage difference between the inside and outside faces of the wall. If the wall thickness d is 1 mm and the maximum voltage applied is 1 kV, the corresponding radial displacement is $\Delta r / r \approx 3\cdot 10^{-4}$. Since the temperature induced fluctuation of the repetition frequency is ~10^{-5}, at least ~1/10 of the fiber length in the laser cavity should be wound onto the PZT tube. In fact, due to the limited bandwidth of the high-voltage driver for PZT tube, the driving voltage on the tube is not fast enough to compensate

the fiber length fluctuation if only 1/10 of the fiber is wound on the tube. More fiber (e.g., 1/3) should be wound onto the tube for a stable operation. This is quite difficult for a mode-locked laser with short cavity. In this case, additional method of thermal isolation should be applied, for example, putting the laser cavity in a foam box.

3.3.3 Experiment and results

The experimental setup for feedback control of the repetition frequency of a passively mode-locked laser is given in Fig. 3.8. A phase locked loop or PLL is used. The principle of this scheme can be described as follows. The output of the passively mode-locked fiber laser is converted to electrical signal by a photodetector. One harmonic of the fundamental repetition frequency is mixed with a local oscillation (reference). The baseband signal is filtered out by a low pass filter after the output of the mixer and fed into the PI controller. The PI controller then generates a control signal to the high voltage amplifier and drives the PZT tube in the laser cavity to compensate the fluctuation of the effective cavity length (equal to effective index times physical cavity length).

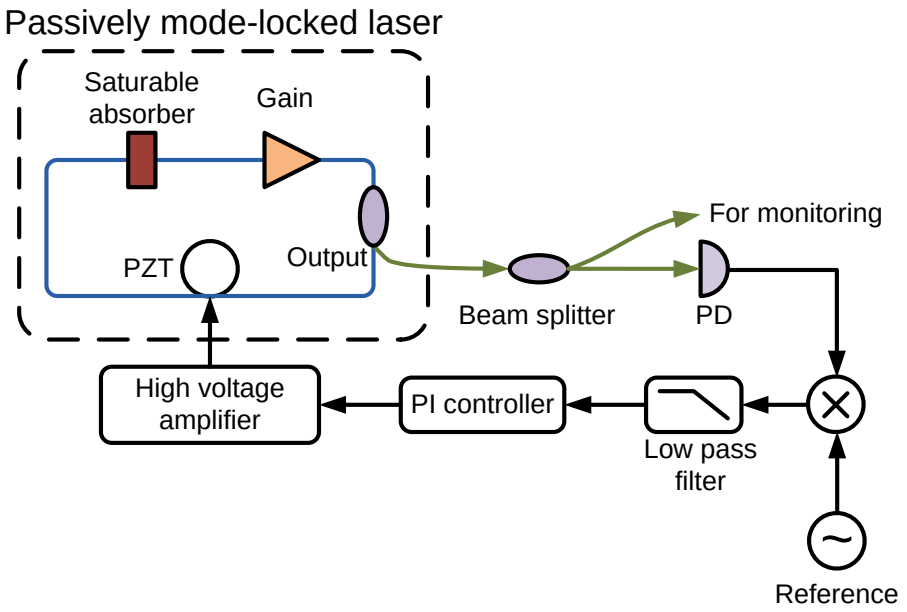

Fig. 3.8 Experimental setup for feedback control of the repetition frequency of a passively mode-locked laser

A simple mathematical analysis is performed. Suppose the signal after photodetection is given by

$$V(t)=\sum_{n=0}^{+\infty}V_n\cos(2\pi nf_Rt+\varphi_n) \tag{3.15}$$

And suppose the frequency of reference is mf_R, the signal after mixer is given by

$$\begin{aligned}V_{IF}(t)&=K_{mix}V_{REF}\cos(2\pi mf_Rt)\cdot\sum_{n=0}^{+\infty}V_n\cos(2\pi nf_Rt+\varphi_n)\\&=K_{mix}V_{REF}\sum_{n=0}^{+\infty}\frac{1}{2}V_n[\cos(2\pi(n-m)f_Rt+\varphi_n)+\cos(2\pi(n+m)f_Rt+\varphi_n)]\end{aligned} \tag{3.16}$$

If the bandwidth of low pass filter after the mixer is much smaller than the repetition frequency, only one term is left after the signal going through the filter, given by

$$V_{LPF}(t)=\frac{1}{2}K_{mix}V_{REF}V_m\cos(\varphi_m) \tag{3.17}$$

Therefore if the set point of the PI controller is zero, the harmonic frequency has a 90 degrees phase difference compared with the reference. In the experiment, the repetition frequency is 58.37 MHz and the 11th harmonic frequency 642.1 MHz is used to locked to the reference because the phase noise of the reference generated from a microwave signal generator with the power of 10 dBm is relatively low at this frequency. A 2 GHz photodetector (Thorlabs DET01CFC) is used for O/E conversion. The mixer has a 6 dB conversion loss with respect to the power of the input RF signal (that is ~-14 dBm at 642.1 MHz). So the IF signal has a power of ~-20 dBm or a peak-to-peak amplitude of 64 mV. The PI controller is from SRS (SIM960) with a bandwidth of 100 kHz and a rise time of ~3.5 μs. The high voltage amplifier (SVR 1000-1) and the PZT tube are from Piezomechanik GmbH. The high voltage amplifier has a maximum output voltage of 1 kV and a bandwidth of a few tens of kHz. The PZT tube has an outside diameter of 74 mm and a maximum diameter displacement of 5 μm. Roughly 1/5 of the fiber in the cavity is wound onto the PZT tube. The resonance frequency of the PZT tube is 13 kHz. Fig. 3.9 shows the output RF spectrum of the photodetector. The resolution bandwidth is 1 MHz.

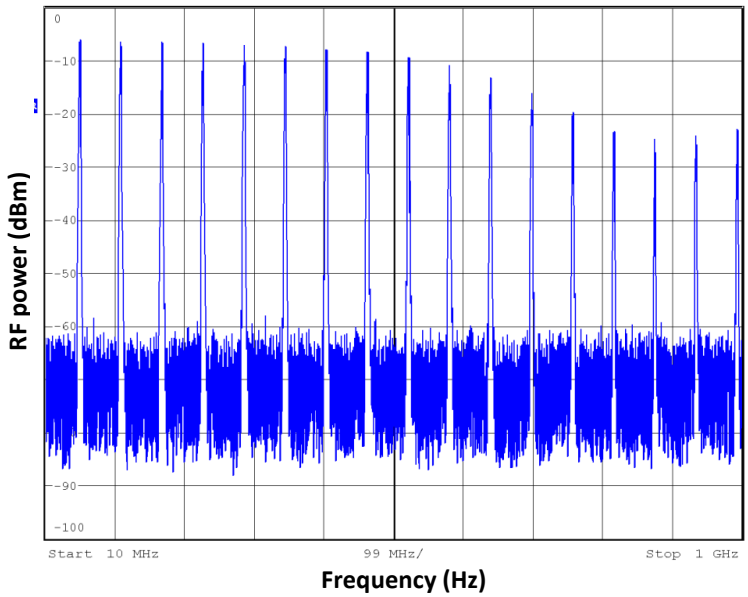

Fig. 3.9 Output RF spectrum of the photodetector. resolution bandwidth is 1 MHz

Fig. 3.10 shows the harmonic frequency at 642.1 MHz when the PLL is off. The measurement time is 30 minutes and the RF spectrum analyzer is set at 'max hold' mode. It can be seen that the frequency drifts approximately by 1 kHz. The spikes seen at ~4 kHz away from the center frequency are generated by knocking the optical table. These spikes are faster fluctuation compared with the slow drift induced by the temperature. For comparison, Fig. 3.11 shows the same frequency region when the PLL is on with the same measurement time and analyzer settings. It can be seen that the center frequency is stable compared with the case when PLL is off. The noise level near the center frequency is higher because the noise performance from the signal generator is not so good.

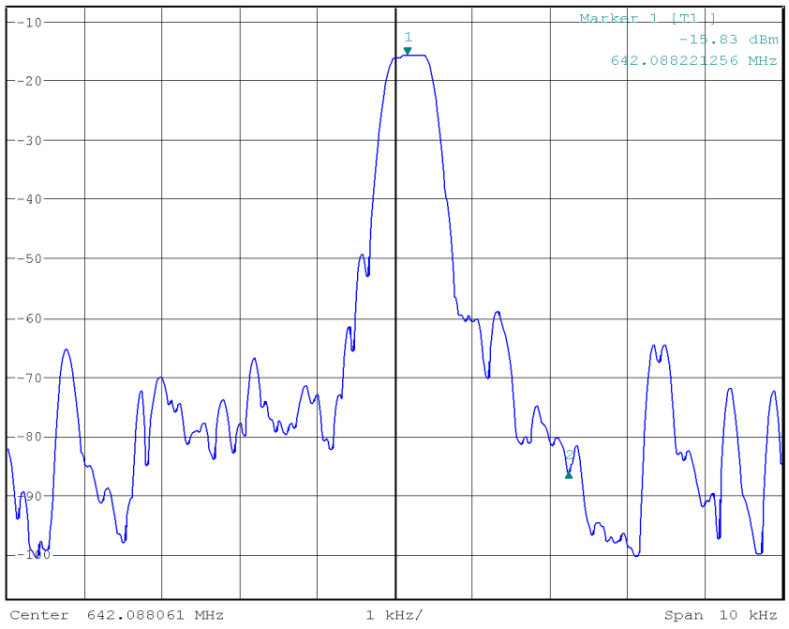

Fig. 3.10 The frequency stability at 642.1 MHz when the PLL is off. The measurement time is 30 minutes and the RF spectrum analyzer is set at 'max hold' mode.

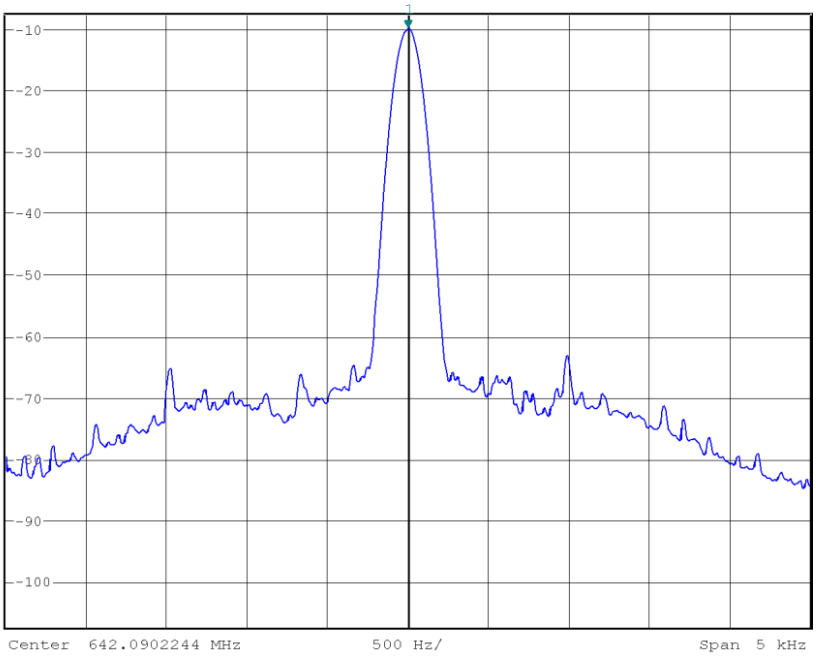

Fig. 3.11 The frequency stability at 642.1 MHz when the PLL is on. The measurement time is 30 minutes and the RF spectrum analyzer is set at 'max hold' mode.

Then we measure the phase noise power spectrum density (PSD) of the stabilized and un-stabilized signals at the same frequency, shown in Fig. 3.12. It can be seen that the phase noise at low offset frequency (< 2 kHz) has been suppressed after feedback control. Due to the poor noise properties of the signal generator, the noise level after feedback control is higher than the original one. The phase noise spectrum of the signal generator is found to show a plateau around -110 dBc/Hz from 100 Hz to 20 kHz which is just what we have observed when the laser is stabilized. The phase noise spectrum of the laser can be further reduced by using a quiet signal source as a reference such as an oven controlled oscillator (OCXO) or a low-noise frequency synthesizer with reference to an atomic clock [7].

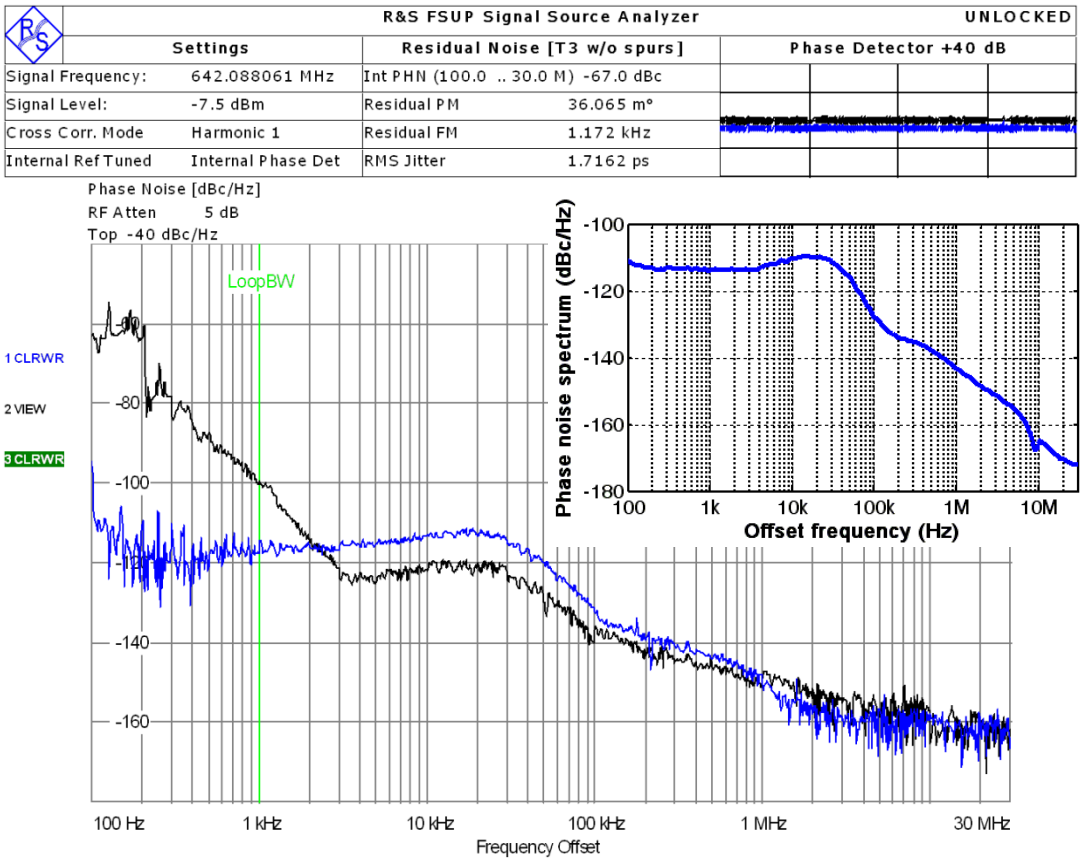

Fig. 3.12 Phase noise PSDs of the stabilized (blue curve) and unstabilized (black curve) signals at 642.1 MHz. Inset: Phase noise PSD of the signal generator.

For the 11th harmonic frequency, we tune the reference frequency slowly from 642.09366082 MHz to 642.0959496077 MHz. The feedback loop is able to adjust the repetition frequency of the mode-locked laser accordingly so as to track the change of the reference. The relative change of the frequency is ~$3.6\cdot10^{-5}$ which means the system is able to compensate a slow drift of frequency of ~$3.6\cdot10^{-5}$. Since the relative drift of laser repetition frequency is ~10-5 in laboratory condition, the feedback loop is able to stabilize the laser repetition frequency all the time once the loop is locked.

3.3.4 Summary

In summary, with theoretical analysis of the drift of the repetition frequency of a mode-locked fiber laser, the feedback control based on PZT is demonstrated. The drift of the repetition frequency is ~10^{-5} and the feedback control loop is able to stabilize the repetition frequency with respect to the external reference oscillator. Furthermore, by slowly tuning the frequency of the reference oscillator, we find that the feedback control loop is able to compensate a maximum drift of frequency of ~$3.6 \cdot 10^{-5}$.

3.4 *Noise suppression by using external incoherent addition structure*

3.4.1 Introduction

Most proposed methods to reduce the phase noise of a mode-locked laser are directly applied onto the laser design. An obvious question is that is there any external method to reduce the phase noise of an optical pulse train? H. Tsuchida has reported such an external structure by applying incoherent addition to reduce the phase noise of semiconductor laser diodes [19]. Compared to the other methods, this technique is simple in setup, flexible to be applied to some semiconductor laser diodes commercially available without any change in the source components. With this method, Tsuchida has successfully reduced the phase noise of semiconductor laser diodes. However, it is known that the original phase noise of semiconductor laser diodes is usually high due to their stronger spontaneous emission in the quantum well structure and higher sensitivity to the defects in the waveguide induced by the non-ideal fabrication. Therefore it is unknown whether Tsuchida's method is still effective for other mode-locked laser types with lower original phase

noise, e.g., mode-locked solid state lasers and mode-locked fiber lasers. Or in another word, to what levels of phase noise spectra of mode-locked lasers or optical pulse train can this incoherent addition method be applied so as to suppress the phase noise and timing jitter? In this section, we investigate this noise limitation of the method by using a low-noise passively mode-locked fiber laser as a reference and comparing the phase noise spectrum after the light passing through the incoherent addition structures. Two incoherent structures, Mach-Zehnder (MZ) and ring, are compared. It is found that the external MZ and ring structures are not suitable for the timing jitter reduction for the pulse train directly from the mode-locked fiber lasers due to their low phase noise property. But they are able to reduce the timing jitter for the pulse train after amplification which usually has a phase noise level higher than -130 dBc/Hz at high offset frequency range.

3.4.2 Theoretical analysis on incoherent addition

The basic incoherent addition structures are MZ and ring, shown in Fig. 3.13 (a) and (b), respectively. It can be seen that the MZ structure is very similar to an MZ interferometer. However, we do not use the term "interferometer" because interferometer refers to the coherent addition and our MZ structure refers to the incoherent structure, i.e., the delay between two arms is longer than the coherent length of the laser source. The delay time is set to the multiples of the period of the pulse train. Therefore the two pulse trains propagating in the two arms of the MZ structure combine with each other at the second coupler to give incoherent intensity addition. Similar design is applied to the ring structure. Precise optical length control can be realized by finely tuning the optical variable delay line (VDL). For practical

application, variable optical attenuator (VOA) is also needed to balance the power in the two arms.

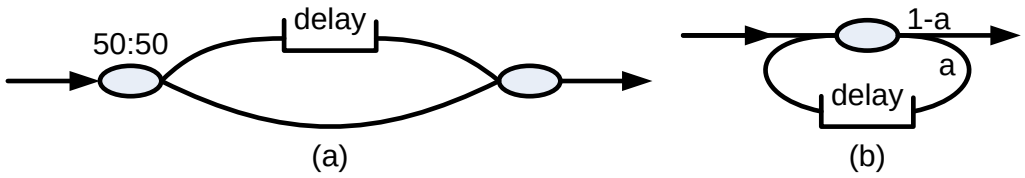

Fig. 3.13 Configurations for (a) MZ and (b) ring incoherent addition structure

For MZ structure shown in Fig. 3.13 (a), the phase noise power spectral density $S_{out}(f)$ of the output pulse train from the MZ structure can be derived as [19]

$$\begin{aligned} S_{out}(f) &= S_{in}(f)\left|1+e^{-j2\pi f\tau_d}\right|^2/4 \\ &= S_{in}(f)\cos^2(\pi f\tau_d) \end{aligned} \tag{3.18}$$

where $\tau_d = mT_R$ is the delay time between the two arms, m is a positive integer and T_R is the pulse train period. We can also define the suppression ratio as follows

$$Z(f) = \cos^2(\pi f\tau_d) \tag{3.19}$$

This equation implies that deep dips can be found at $f=(n+0.5)/\tau_d$, $n=0, 1, 2,\ldots$ in the phase noise spectrum which can be used for periodical phase noise suppression. It should be mentioned that Eq.(3.18) is derived in the best condition that the power levels in the two arms are well balanced. For a perfect power balance in the two arms, the dips of the phase noise suppression at $f=(n+0.5)/\tau$ can reach zero. If the power levels in the two arms are different, the dips introduced by the MZ structure lift up and become less 'deep'. This is the reason of using a VOA in one arm of the MZ structure. VDL usually introduces 2-3 dB loss and VOA is therefore

inserted in the other arm to balance the loss from VDL and the power difference from the 50:50 coupler.

The physical meaning of such a MZ structure is that, due to the phase noise or timing jitter of the optical pulse train, pulses randomly drift from their original positions. When one pulse adds to another delayed pulse after the MZ structure, the new pulse combined by these two pulses has a timing jitter equal to the average of the timing jitters of the two original pulses. And if we assume the timing jitter is a stationary random process, averaging process can reduce the total timing jitter.

A similar mechanism of phase noise suppression is also applied to the ring structure, shown in Fig. 3.13 (b). Fraction a of the input power is fed into the ring arm with a transmission of G. The delay time of the feedback path is also set to an integer multiple of the pulse repetition period to ensure the incoherent addition of the pulse trains at the output terminal of the coupler. The output phase noise PSD can be derived as

$$S_{out}(f) = S_{in}(f)\left|\frac{1-a+(2a-1)Ge^{-j2\pi f\tau_d}}{1-G(1-a)e^{-j2\pi f\tau_d}}\right|^2 \tag{3.20}$$

The corresponding suppression ratio is

$$Z(f) = \left|\frac{1-a+(2a-1)Ge^{-j2\pi f\tau_d}}{1-G(1-a)e^{-j2\pi f\tau_d}}\right|^2 \tag{3.21}$$

$S_{out}(f)$ shows minima at $f=(n+0.5)/\tau_d$, $n=0, 1, 2,\ldots$ We plot the suppression ratio $Z(f)=S_{out}(f) / S_{in}(f)$ for both MZ and ring structures in Fig. 3.14 (a). For ring structure, we assume $G=1$. It can be seen that, compared with the MZ structure, the ring structure provides a wider noise suppression bandwidth because more than two

pulse trains are incoherently added in the ring structure. But meanwhile MZ can reach a deeper dip than ring structure. We also calculated the integral suppression ratio defined as follows, shown in Fig. 3.14 (b).

$$Z_{\text{int}} = \frac{\int_0^{\infty} S_{out}(f)dt}{\int_0^{\infty} S_{in}(f)dt} \approx \int_0^{\infty} Z(f)dt \tag{3.22}$$

So the ring structure is supposed to achieve a better phase noise suppression than the MZ structure in ideal case.

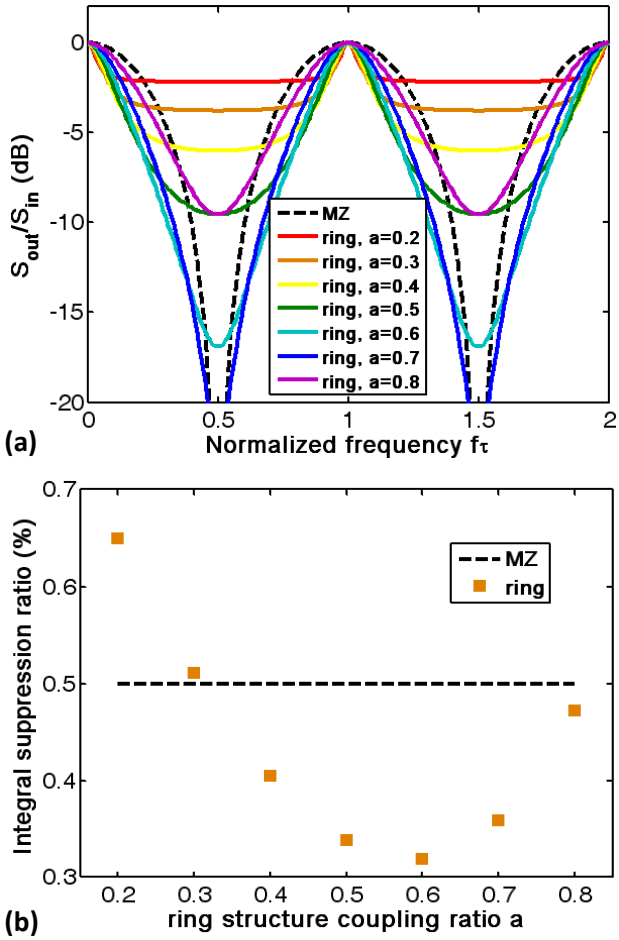

Fig. 3.14 (a) Suppression ratio for MZ and ring structures and (b) integral suppression ratio when the coupling ratio a varies from 0.2 to 0.8

For both the MZ and ring structures, different delay time influences the position of dips and a longer delay time leads to more minima in the phase noise spectrum and each minimum has a narrower noise reduction bandwidth. And both MZ and ring structures are not sensitive to polarization fluctuation because pulses are incoherently added and have no difference after photodetection.

3.4.3 Experiment

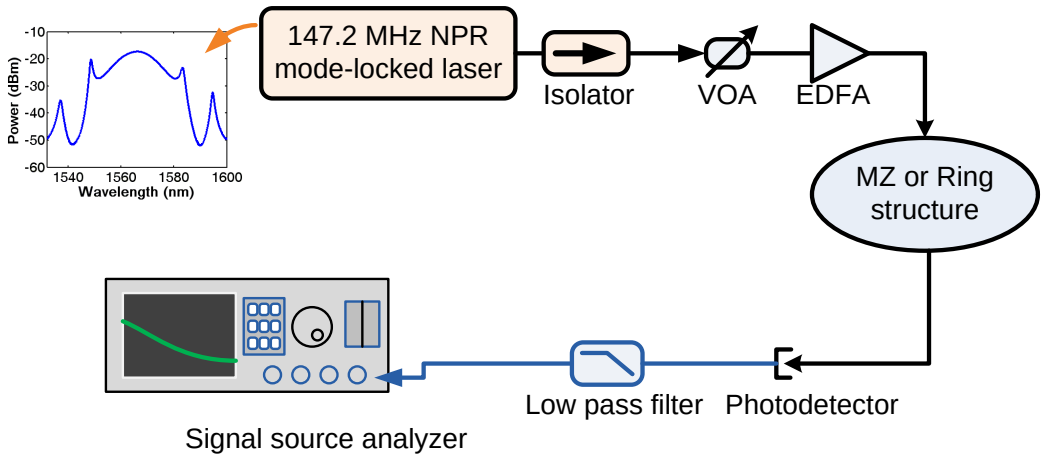

Fig. 3.15 Experimental setup for phase noise suppression with MZ or ring structure.

Fig. 3.15 shows the block diagram of the experimental setup. The laser source is a 1560 nm passively mode-locked fiber ring laser based on nonlinear polarization rotation (NPR). The laser has a repetition frequency of 147.2 MHz corresponding to a period of 6.8 ns, a pulse width of 390 fs and a bandwidth of 20 nm. Phase noise of the direct output is below -150 dBc/Hz measured in the offset frequency range from 100 kHz to 30 MHz. To test the effectiveness of the MZ and ring structures for different phase noise levels, a combination of VOA and Erbium doped fiber amplifier (EDFA) after the isolator is applied to adjust the output phase noise level at this frequency range. The principle of this setup is that when we set

VOA to a large value, i.e., the signal power incident into the EDFA is low, EDFA will contribute more phase noise at the output due to the amplified spontaneous emission. Five different background phase noise levels ranging from -112 dBc/Hz to -152 dBc/Hz can be obtained by controlling the incident power to the EDFA and its drive current. Four structure arrangements are tested in the experiment: MZ structures of 5T (1T represents the pulse train period of 6.8 ns, corresponding to a fiber length of 1.36 m) and 11T delay, ring structures of 6T (i.e., the length of the loop corresponds to a delay of 6 pulse train periods) and 12T delay. A coupling ratio 50:50 is used in the MZ structures, and 60:40 is used in the ring structures to optimize the performance. The pulse train at the output of the structure is fed into a signal source analyzer (SSA) for the measurement of phase noise. The system noise floor of the SSA is below -150 dBc/Hz at the frequency range from 1 MHz to 30 MHz. Typical phase noise power spectral densities, or phase noise spectra, are shown in Fig. 3.16 for the four different structures at an input phase noise spectra level of -112 dBc/Hz from the EDFA. The dashed lines are the theoretical estimation.

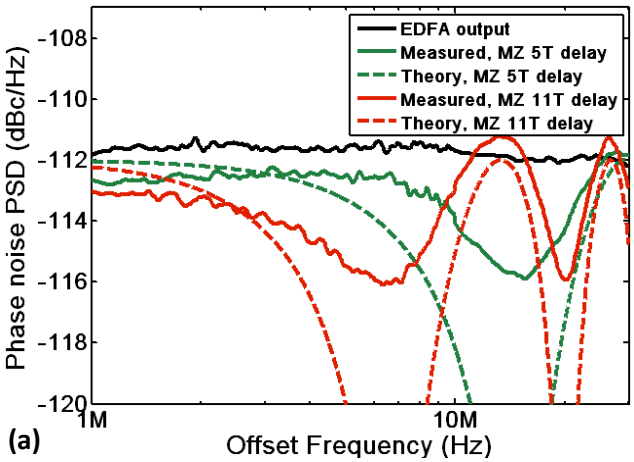

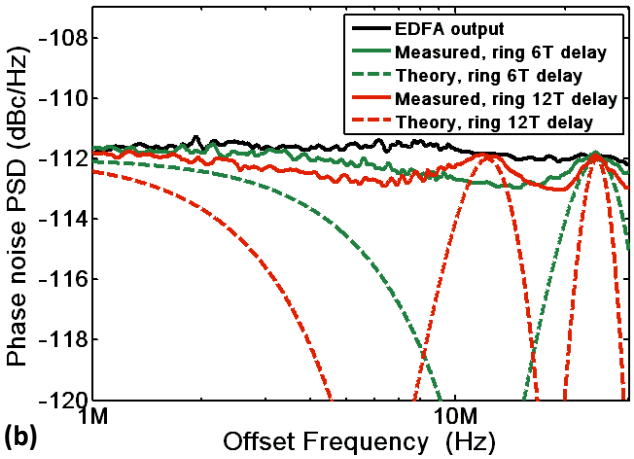

Fig. 3.16 Phase noise spectra at -112 dBc/Hz input phase noise level measured from 1 MHz to 30 MHz for (a) MZ structures and (b) ring structures

The predicted minima by the theory can be observed in the experimental results. However the values of minima in the measured phase noise spectra are much smaller than expected for both MZ and ring structures. There are two possible reasons for this observation. They are fiber dispersion and fiber length fluctuation. Dispersion causes the pulse broadening during the pulse propagation. For the MZ structure, pulses passing through longer arm experience more serious pulse broadening effect, e.g., for a 11T delay MZ structure, the pulses in the longer arm have an additional pulse broadening of 17 ps/(km·nm)*20 nm* 15 m=5.1 ps when standard single mode fiber is used. In this case, the broadened pulses from the longer arm do not totally overlap with the pulses from the shorter arm. For the same reason, the ring structures have much poorer performance compared with the theoretical estimation. The pulses circulate many (e.g., 6-7) round trips in the ring which makes the dispersion problem more serious. Also, it can be seen in Fig. 3.16 that the phase noise spectra at the MZ structure output may even have higher maxima compared to that directly from the EDFA output. Fiber length fluctuation means that fiber length experiences fluctuation due to the temperature drift, mechanical vibration and air

flow etc., which leads to the timing fluctuation of the pulses propagating in the fiber. As shown in the previous chapter, fiber length fluctuation is around ΔL/L=10-5 in the laboratory condition. For an 11T delay MZ structure, this means the corresponding relative drift of the pulse timing positions in the two arms is 11*6.8 ns*10^{-5}=748 fs. This value is comparable with the original pulse width of 390 fs and the pulse width after propagating through the MZ structure (a few ps). Therefore, fiber length fluctuation is a possible reason causing the fluctuation of relative timing positions of pulses and leading to smaller minima in the phase noise spectra. To verify the effect of dispersion, we replace the single mode fiber with a dispersion of 17 ps/(km·nm) in the delayed arm by HI1060 fiber with a lower dispersion of ~8 ps/(km·nm) while maintaining the same length for a 10T delay MZ structure, it can be seen that the maxima become lower. Further replacing the SMF with NZ-DSF may have better improvement for the MZ structure. However, due to the limited fiber available, we did not test this assumption. The change of dip depth is not very clear which may suggest that the effect of fiber length fluctuation is more important for the dip in a MZ structure. Unfortunately we are unable to isolate the effect of fiber length fluctuation with our current experimental facilities and environment.

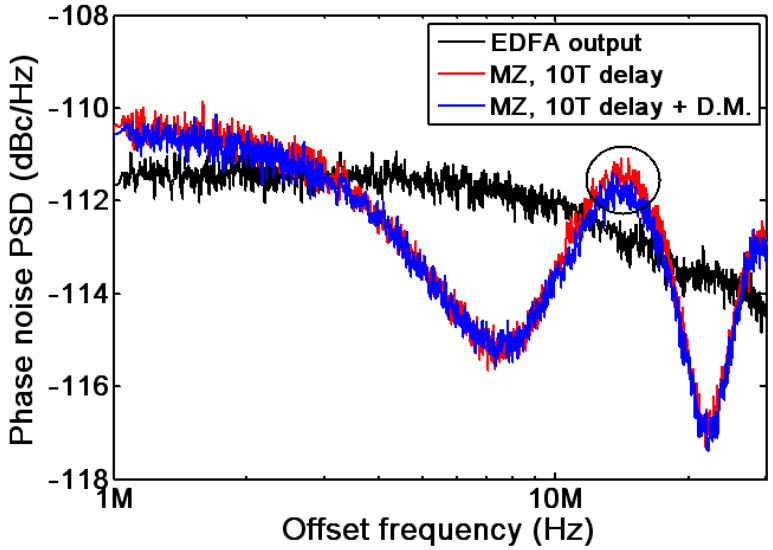

Fig. 3.17 Phase noise spectra with and without dispersion management for a 10T delay MZ structure. The spectrum directly from EDFA output is also given for reference.

Fig. 3.18 (a) shows the minima depths of phase noise suppression that the MZ and ring structures can reach at different input phase noise levels. The minima depths are measured with respect to the phase noise spectrum at the EDFA output. It can be seen that all four structures (5T delay MZ, 11T delay MZ, 6T delay ring, 12T delay ring) are less effective when the input phase noise level is low. Incoherent addition is found effective for the input phase noise levels above -130 dBc/Hz. Since dispersion is the same for a certain setup, e.g., a 5T delay MZ structure, the change of the minima depths with the input phase noise levels is likely due to the fiber length fluctuation which causes an unavoidable mismatch among pulses in the incoherent addition process and the role of this effect is obviously more serious when the original input phase noise is low which leads to a weaker effect of phase noise suppression.

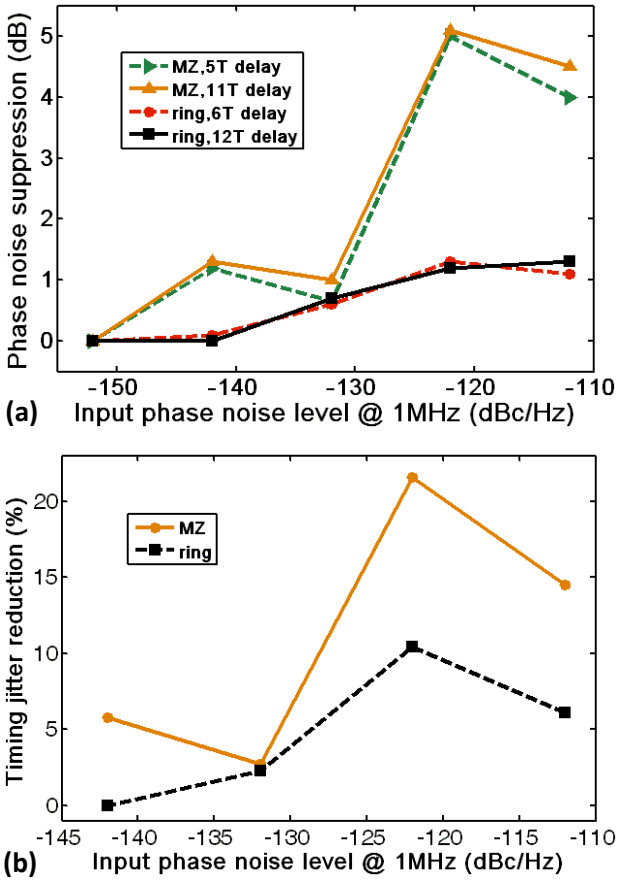

Fig. 3.18 (a) Phase noise suppression depths at minima point and (b) timing jitter reduction with respect to different input phase noise levels measured at 1 MHz offset frequency for MZ and ring structures

According to the theoretical analysis, same types of incoherent addition structures with different delay time should have the same amount of phase noise reduction, which is confirmed in the experiment. A maximum timing jitter reduction of ~21% is obtained at -122 dBc/Hz input phase noise level (integrated from 100 kHz to 30 MHz) when applying the MZ structure. The details of the timing jitter reduction are shown in Fig. 3.18 (b).

3.4.4 Discussion

It is meaningful to understand the effect of intensity mismatch of the pulses in the different arms of a MZ structure or the effect of a high loss in the ring structure.

Experiment on the intensity mismatch can help to verify how sensitive the MZ structure is to the unbalanced power levels or the ring structure is to the additional loop loss. In the experiment, VOA is set to different values to generate a controlled power difference for a MZ structure of 10T delay and a controlled loop loss for a ring structure of 8T delay. Fig. 3.19 shows the measured results for both structures. It can be seen that when the VOA varies from 0 dB to 10 dB, the dip varies from ~4 dB to ~0.5 dB accordingly. Similar results are also observed for the ring structure. The dip depth decreases from ~2.5 dB to nearly 0 dB when the loop loss increases from 0 dB to 10 dB. Therefore it is demonstrated that power balance in the two arms of a MZ structure or the loop loss of a ring structure play a very important role in achieving good phase noise suppression for the incoherent addition approach.

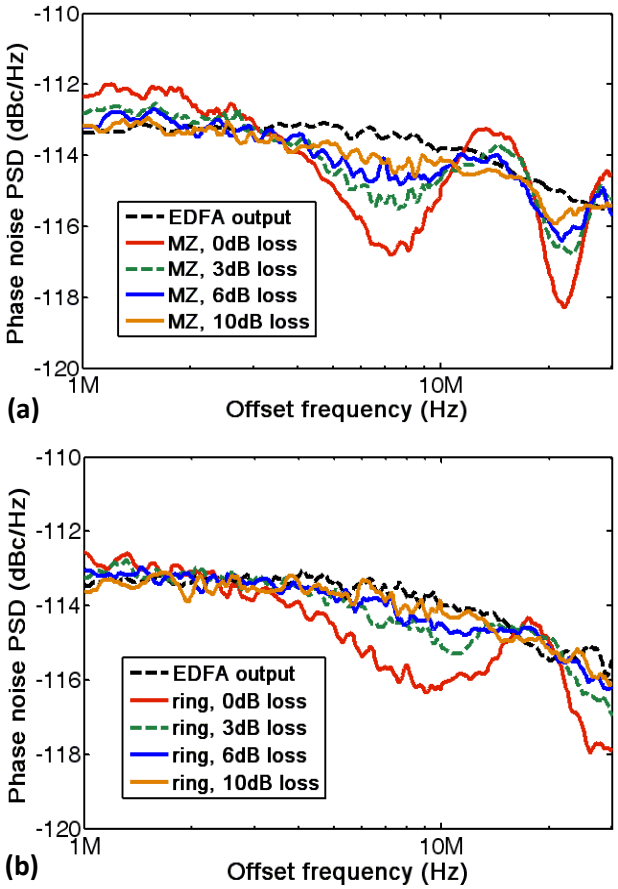

Fig. 3.19 Phase noise spectra with different loss for (a) 10T delay MZ structure and (b) 8T delay ring structure when the loss varies from 0 dB to 10 dB.

We have also tested the cascaded MZ structures, shown in the following figure. A 9T delay MZ structure is cascaded by a 4T delay MZ structure. The bandwidth of noise suppression is much wider in the cascaded MZ structures than in the single MZ structure. The dips at 8.2 MHz and 24.5 MHz for 9T delay MZ and at 18.4 MHz for 4T delay MZ can be clearly observed.

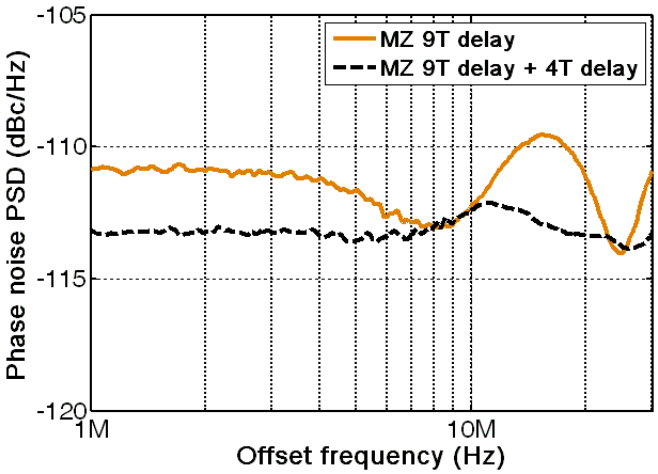

Fig. 3.20 Phase noise spectra for a single 9T delay MZ structure and for cascaded 9T delay + 4T delay MZ structures. Dips at 8.2 MHz and 24.5 MHz for 9T delay MZ and at 18.4 MHz for 4T delay MZ can be clearly observed.

Also, the MZ and ring structures apply incoherent addition of pulses, so the polarization does not affect the property of the system. Moreover, since incoherent addition provides an averaging mechanism by adding two different pulses in time domain. Similar dips can also be observed in the RIN spectrum.

Here we give a comparison between the MZ structure and ring structure in the following table

Table 3.1 Comparison between MZ and ring structures

	MZ structure	***Ring structure***
Phase noise suppression depth (theory)	the minima can reach zero when the power in the two arms are balanced	the minima cannot reach zero
Phase noise suppression depth (experiment)	the deepest minima depth is ~5 dB	the deepest minima depth is ~1.5 dB
Phase noise suppression bandwidth	narrow suppression bandwidth both in theory and in experiment	wide suppression bandwidth both in theory and in experiment
Maximum timing jitter reduction	~21% at -122 dBc/Hz input phase noise level	~10% at -122 dBc/Hz input phase noise level
Minimum phase noise level for observable phase noise suppression	~-130 dBc/Hz at high offset frequency range	~-130 dBc/Hz at high offset frequency range
Insertion loss	>6 dB, mainly due to the loss of the delay line and of the second coupler combing the two arms	>3 dB, mainly due to the loss of the delay line

3.4.5 Summary

In summary, we have investigated theoretically and experimentally the effectiveness of Mach-Zehnder and ring structures as an external configuration to suppress the phase noise of the optical pulse train. Measurement results show that effective phase noise suppression at specific spectrum positions can be achieved by both types of structures when the input phase noise level of the pulse train is above -130 dBc/Hz at high offset frequency range. The MZ structures can achieve a deeper phase noise suppression than the ring structures and therefore lead to a better timing jitter reduction for all different input phase noise levels in our experiment. A best timing jitter reduction of ~21% by MZ structures is obtained at an input phase noise level of

-122 dBc/Hz at high offset frequency range whereas the best reduction by ring structures is ~10% at the same input phase noise level. Dispersion compensation helps to reduce the pulse broadening effect for both structures and can further improve the effect of the incoherent addition. It should be mentioned that although the external MZ or ring structures may not be able to be directly applied to the pulse train directly from the mode-locked fiber lasers for timing jitter reduction due to its low phase noise level, they are still effective for phase noise suppression and timing jitter reduction for the pulse train after amplification which typically has a phase noise level higher than -130 dBc/Hz at high offset frequency range.

4 Linear noise conversion from the pump to the mode-locked fiber lasers

Low-noise mode-locked lasers are of importance in many research areas such as frequency metrology [5] and microwave signal synthesis [13]. Various studies have been done on their quantum noise limits [31, 36], noise reduction [23-24, 53, 65], and noise measurement [56] etc. It has been known that the relative intensity noise (RIN) of the pump converts to the RIN and phase noise of the mode-locked lasers through various mechanisms [36, 66-67]. It is important to understand quantitatively how the noise of mode-locked lasers is affected by the pump noise. With the knowledge of this noise conversion process, one can easily evaluate the noise of the laser induced by the pump which is helpful to achieve low-noise operation for various applications such as frequency metrology and timing distribution. The linear noise conversion from the pump RIN to the RIN and phase noise in Ti : Sapphire mode-locked lasers has been experimentally measured [67-68]. It was found that there is direct correlation between the pump noise and laser noise in a Ti : Sapphire laser. The noise conversion function was characterized by applying pump modulation technique. However, there is yet no work investigating the linear noise conversion from the pump RIN to the laser RIN and laser phase noise for the mode-locked lasers at 1.5 μm and no work on the comparison of the noise conversions for the lasers mode locked by different mechanisms, e.g., nonlinear polarization rotation (NPR) and semiconductor saturable absorber mirror (SESAM). It is also the first time that an excess noise conversion due to the slow saturable absorber effect of SESAM is reported.

4.1 *Principle and experimental setup*

In this section, we characterize the linear noise conversion from the pump RIN to the RIN and phase noise of the passively mode-locked lasers at 1.5 μm and two mode locking mechanisms, NPR and SESAM, are compared for the first time. Pump modulation technique is applied. Both lasers (named as NPR laser and SESAM laser) are mode locked in the soliton region. It is found that both the RIN and phase noise of the two lasers are dominated by the noise converted from the pump RIN, i.e., the RIN and phase noise power spectral densities (PSDs) can be predicted with the measured pump RIN PSD and noise conversion ratios, similar to what was observed in a Ti : Sapphire laser [67]. Also, different mode locking mechanisms, i.e., NPR and SESAM, exhibit similar conversion behavior from the pump RIN to the laser RIN but very different conversion behavior from the pump RIN to the laser phase noise. We attribute this difference to the slow saturable absorber effect of the SESAM causing an excess RIN to phase noise conversion in the SESAM laser.

The experimental setup is shown in Fig. 4.1 (a). The lasers are pumped by a 976 nm diode and the drive current of the pump diode is modulated to generate a controlled RIN of the pump. This pump RIN then transfers to the RIN and the phase noise of the lasers through various mechanisms, such as gain modulation effect [66]. After an isolator, the output of the lasers is fed into an acousto-optic modulator (AOM) and then into a 2 GHz photodetector (PD). AOM is used to evaluate the RIN-to-phase-noise conversion in the photodetector [16-17] to guarantee that this excess noise conversion induced by the PD is below the original noise in the laser and will not affect the measurement results in the experiment. A low pass filter (LPF)

and a low-noise amplifier (LNA) are used to extract the electrical signal at fundamental repetition frequency of the lasers for noise measurement by a signal source analyzer (SSA, R&S FSUP26). The schematics of the two lasers are shown in Fig. 4.1 (b) and (c) and the detailed parameters are listed in Table 4.1. The inset in Fig. 4.1 (a) shows the RF spectrum measured at the repetition frequency of the SESAM laser with 1 kHz pump modulation. The sidebands induced by the pump modulation can be clearly observed.

Due to the different mode locking mechanism and cavity design, it is very difficult to control the parameters of the two lasers to be close. In fact, since the measurement of pump RIN conversion is done for a single laser, there is no need to make two lasers have similar parameters.

Table 4.1 Details of the mode-locked lasers under test

	NPR laser	SESAM laser
Repetition frequency	66.1 MHz	163.4 MHz
Center wavelength	1560 nm	1581 nm
3-dB bandwidth	15.1 nm	10.4 nm
Intra-cavity power	17 mW	14 mW
Intra-cavity pulse energy	257 pJ	86 pJ
Net dispersion	-0.06 ps^2	-0.013 ps^2
Pump power	213 mW	59 mW
Pulse duration	130 fs	180 fs

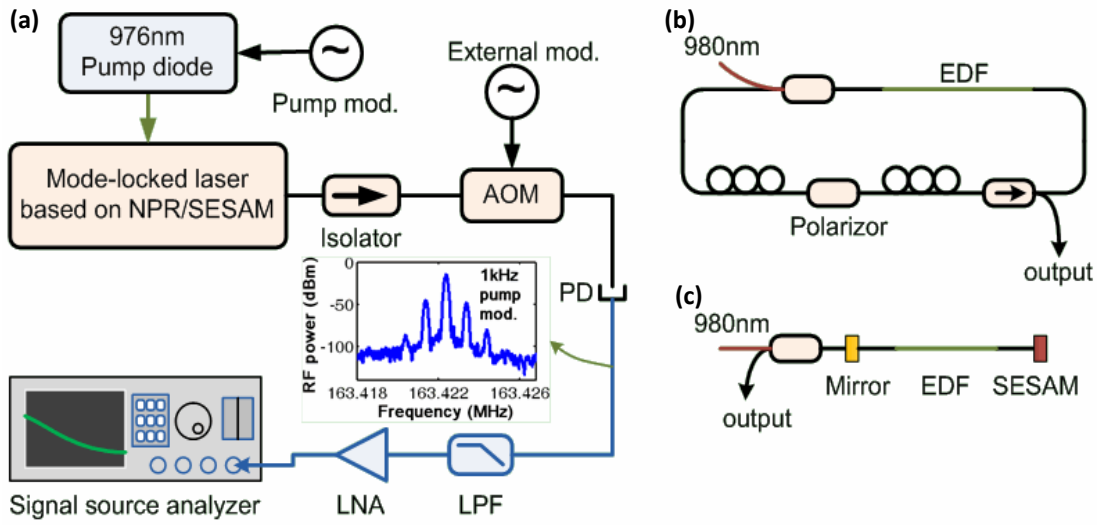

Fig. 4.1 (a) Setup for characterization of the noise conversion from the pump to the mode-locked fiber lasers; Inset: RF spectrum of the SESAM laser output after photodetection with 1 kHz pump modulation; (b) NPR laser setup; (c) SESAM laser setup

The noise conversion ratios are obtained with the following method. A modulation frequency f_M is applied to the drive current of the pump laser diode, thus generating a controlled pump RIN. The pump RIN $S_{Pump\text{-}RIN}$ at f_M (a spurious peak, with the units of dBc) is dominant by the pump modulation and measured by feeding the pump output to the PD with proper attenuation and then characterized by a baseband spectrum analyzer. The laser RIN S_{RIN} and phase noise S_{PN} at f_M (with the units of dBc) are characterized by the SSA. Then the noise conversion ratios from the pump RIN to the laser RIN, r_{RIN}, and to the laser phase noise, r_{PN} , are given by

$$r_{RIN}(f_M) = S_{RIN}(f_M) / S_{Pump-RIN}(f_M) \tag{4.1}$$

$$r_{PN}(f_M) = S_{PN}(f_M) / S_{Pump-RIN}(f_M) \tag{4.2}$$

It is also known that pump modulation introduces observable RF sidebands in the RF spectrum of the lasers after photodetection, e.g., the inset in Fig. 4.1 (a). And the power of these sidebands is equal to the sum of the RIN and phase noise of

the mode-locked lasers based on the theory of RF spectrum analyzer method we have discussed in section 2.4.1. That is

$$P(f_R \pm f_M) / P(f_R) = S_{RIN}(f_M) + S_{PN}(f_M) \tag{4.3}$$

where $P(f_R \pm f_M) / P(f_R)$ represents the relative RF power of the sidebands. So if we define the conversion ratio from the pump RIN to the relative RF power of the sidebands, r_{RF}, as follows

$$r_{RF}(f_M) = P(f_R \pm f_M) / P(f_R) / S_{Pump-RIN}(f_M) \tag{4.4}$$

By substituting Eq.(4.1), (4.2) and (4.4) into Eq.(4.3), we have the following relation at all modulation frequencies

$$r_{RF} = r_{RIN} + r_{PN} \tag{4.5}$$

The left hand side, r_{RF}, is measured by the RF spectrum analyzer and the right hand side, r_{RIN} and r_{PN}, are measured by the demodulation method in the signal source analyzer. Therefore this relation between the RF sidebands and RIN and phase noise can be used to verify the validity of the method we have described to characterize the noise conversion from the pump RIN to the laser RIN and phase noise.

4.2 *Measurement results of the linear noise conversion ratios*

Fig. 4.2 (a) shows the three conversion ratios r_{RIN}, r_{PN} and r_{RF} measured for the NPR laser. The $1/f^2$ line is also drawn for reference. Very good agreement with Eq. (4.5) can be found; this confirms the validity of our method. Thus with the knowledge of noise conversion ratios r_{RIN} and r_{PN} , and pump RIN PSD, we can predict the RIN and phase noise PSD of the lasers according to Eq.(4.1) and (4.2). As shown in Fig.

4.2 (b), the noise PSDs predicted this way agree well with the measured noise PSDs, also indicating that the laser RIN and phase noise are dominated by the noise converted from the pump RIN. The disagreement for the offset frequencies greater than 20 kHz is due to the noise floor of the measurement system. Caused by the shot noise and thermal noise, the measurement system has a noise floor around -140 dBc/Hz for phase noise PSDs and -130 dBc/Hz for RIN PSDs.

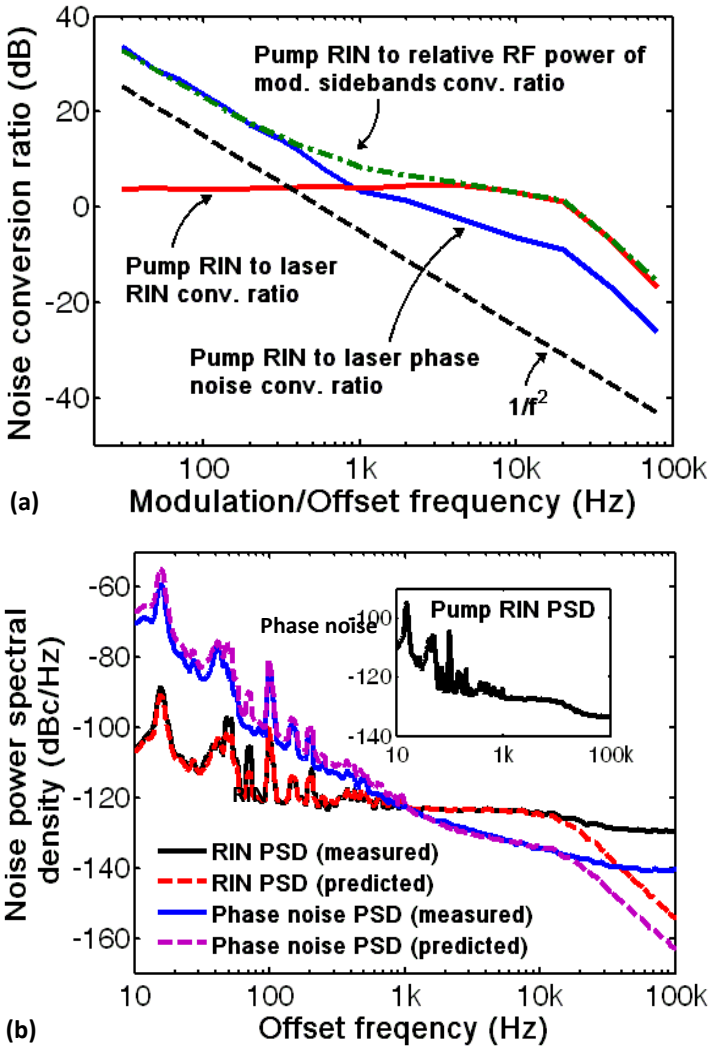

Fig. 4.2 (a) Noise conversion ratios r_{RIN}, r_{PN} and r_{RF} measured for the NPR laser; (b) measured and predicted PSDs of RIN and phase noise of the NPR laser. Inset: PSD of the pump RIN.

Similarly, Fig. 4.3 shows the measured noise conversion ratios and PSDs for the SESAM laser. Again, good agreement can be observed. The measurement results for two mode-locked lasers indicate that the RIN and phase noise for both lasers are dominated by the pump RIN and therefore can be predicted by the measured pump RIN PSD and noise conversion ratios.

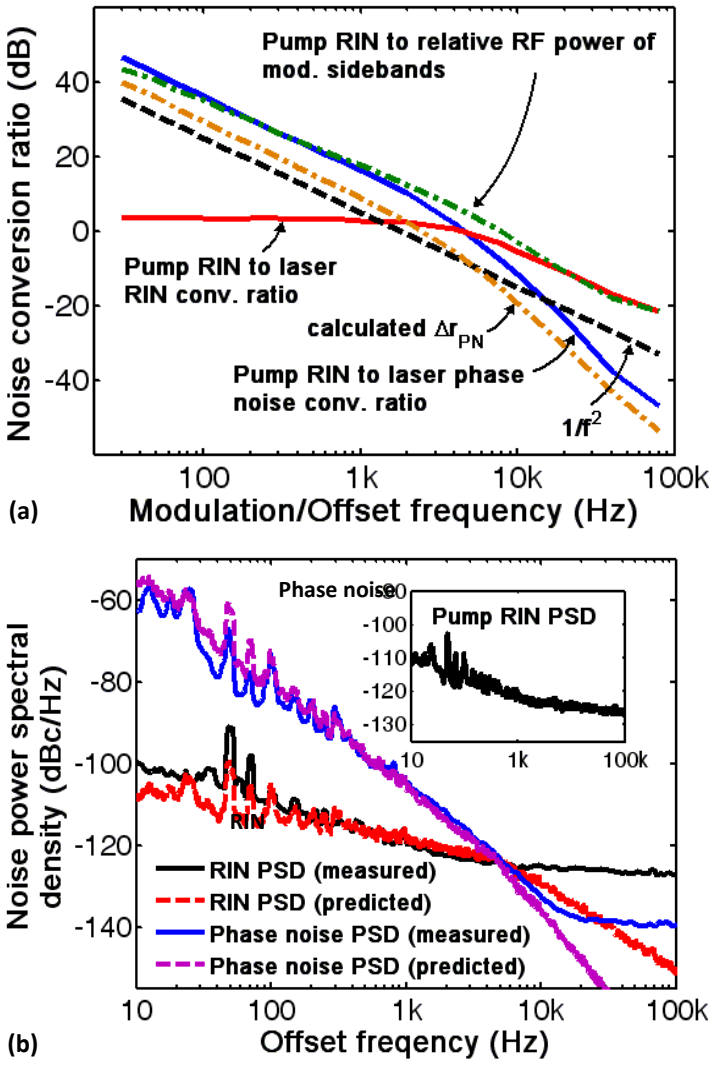

Fig. 4.3 (a) Noise conversion ratios r_{RIN}, r_{PN} and r_{RF} measured for the SESAM laser and the calculated excess phase noise Δr_{PN} based on Eq.(4.8); (b) measured and predicted PSDs of RIN and phase noise of the SESAM laser. Inset: PSD of the pump RIN.

4.3 *Discussion*

It can be noticed that, both for the NPR and SESAM lasers, the RIN noise conversion ratio r_{RIN} exhibits a plateau in the low-offset frequency region and then a rapid decay in the high-offset frequency region. This behavior represents a pump induced fluctuation of the intra-cavity pulse energy [68]. However, the phase noise conversion ratio r_{PN} shows a very different behavior for the two lasers under test. For NPR laser, r_{PN} is very similar to the one measured in a Ti : Sapphire mode-locked laser [67], which shows a -20 dB/decade decay in the low-offset frequency region (<1 kHz) due to the thermo-optic effect and finally a -40 dB/decade decay due to the pump induced timing fluctuation via Kerr nonlinearity [68]. One should note that in Ref.[68] the measured curves were all referred to the amplitude of the noise whereas our measurement presented here is referred to the power of the noise. So the slope of the decay rate in Ref.[68] should be timed by 2 when compared with our results. The following figure shows the fit curves for the measured pump RIN to laser RIN and laser phase noise conversion ratios of the NPR laser. The detailed derivation of the pump RIN to laser RIN conversion can be found in the Appendix A and the pump RIN to laser phase noise conversion can be found in Ref.[68].

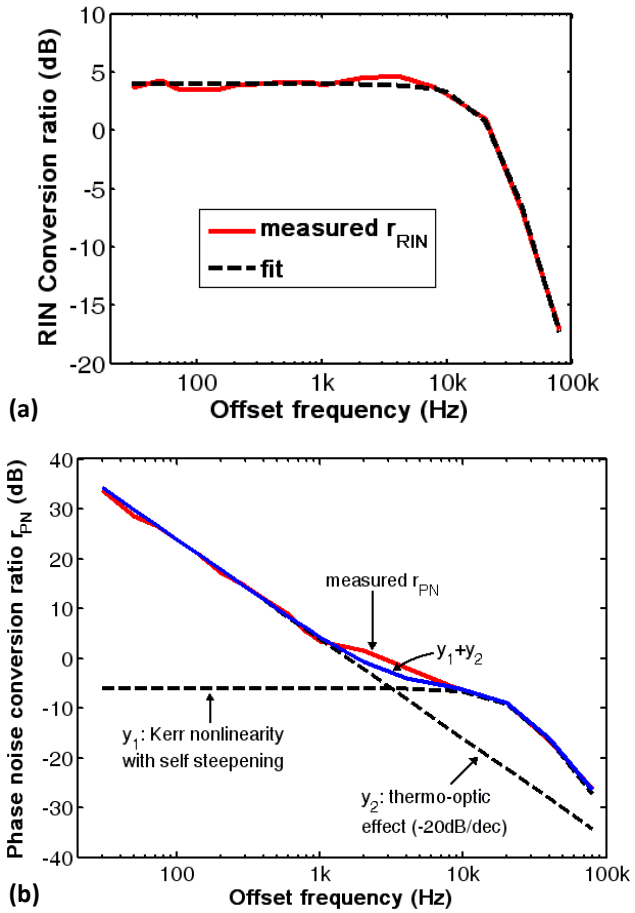

Fig. 4.4 Measured results and fit curves for pump RIN to (a) laser RIN and (b) laser phase noise of the NPR laser. The knee frequency is around 20 kHz

However, for the SESAM laser, r_{PN} is much greater in the low-offset frequency region and then quickly decays in the high-offset frequency region (see Fig. 4.3 (a)). Kerr nonlinearity and the difference of the intra-cavity pulse energy in the two lasers is not likely to be the reason because the pulse energy of ~257 pJ for the NPR laser and ~86 pJ for the SESAM laser would indicate that RIN to phase noise conversion via Kerr nonlinearity in the cavity should be higher in the NPR laser [36]. It is noted that the SESAM is a slow saturable absorber and causes an excess noise conversion effect from the laser RIN to the laser phase noise [36]. This is due to the slow response time of the SESAM. When a pulse enters the SESAM, the SESAM is not fast enough to instantly change its transmission. Therefore, the

rising edge of the pulse experiences a fixed loss. However, the SESAM gradually increases its transmission due to the saturable absorption and therefore the falling edge of the pulse experiences lower loss than the rising edge. This effect tilts the pulse shape and changes the pulse timing position. Moreover, the change of the SESAM loss is dependent on the energy of the incident pulse. Thus the fluctuation of the incident pulse energy leads to the fluctuation of the pulse timing after passing the SESAM. The saturation parameter *s* for the SESAM laser, defined as the ratio of intra-cavity pulse energy and saturation energy of SESAM, is ~2. Then the excess RIN to phase noise conversion due to the slow saturable absorber effect is given by (see Eq. (29) in Ref. [36] for more details)

$$\Delta S_{PN}(f) = \left(\frac{{f_R}^2}{f} \frac{\partial \Delta t}{\partial s} s \right)^2 S_{RIN}(f) \tag{4.6}$$

where f_R is the repetition frequency, $\partial \Delta t / \partial s \approx 1.05 \times 10^{-13} s$ is the pulse shift induced by the slow saturable absorber; this parameter is proportional to the modulation depth of the SESAM. So we have the following relation in the logarithmic scale

$$\Delta S_{PN}(f) \approx 65 - 20 \cdot \lg f + S_{RIN}(f) \tag{4.7}$$

Note that r_{RIN} and r_{PN} are related to S_{RIN} and S_{PN} by Eq.(4.1) and (4.2). Eq.(4.7) can also be applied to r_{RIN} and r_{PN} where we use Δr_{PN} to represent the excess phase noise conversion ratio from the laser RIN. That is

$$\Delta r_{PN} \approx 65 - 20 \cdot \lg f + r_{RIN} \tag{4.8}$$

The calculated Δr_{PN} based on Eq.(4.8) is shown in Fig. 4.3 (a). It can be seen that Δr_{PN} is almost the same as r_{PN} except a ~5 dB difference which may be due to an error in the estimation of saturation parameter *s* and the intra-cavity pulse energy.

Therefore it can be concluded that in the SESAM laser under test, the phase noise is mainly caused by the noise conversion from the laser RIN due to the slow saturable absorber effect. It is also the first time, to our knowledge, this effect is experimentally reported. To further confirm the slow saturable absorber effect. We measured the phase noise PSD of another SESAM laser with similar repetition frequency but smaller modulation depth (~5%) of the SESAM, shown in Fig. 4.5. Current SESAM has a modulation depth ~15%. So the theoretical reduction of the phase noise PSD is 20lg(15/5)=9.5 dB which is very close to the measurement result, i.e., the phase noise PSD value at 1 kHz is ~-100 dBc/Hz for the current SESAM laser in Fig. 4.3 (b) and ~-110 dBc/Hz for the SESAM laser with the small modulation depth in Fig. 4.5. NPR mode-locking is based on Kerr nonlinearity which is a fast saturable absorber with nearly instant response time and thus does not have this excess noise conversion effect.

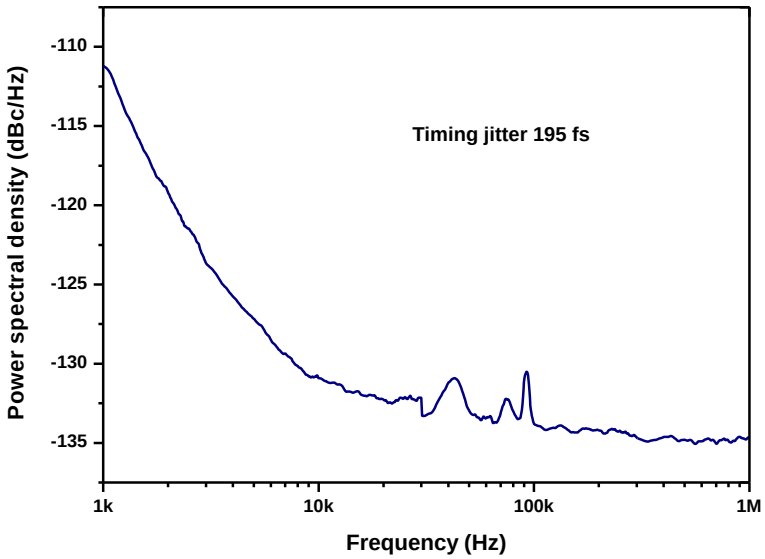

Fig. 4.5 Measured phase noise PSD for a SESAM laser with similar repetition frequency and a smaller modulation depth of ~5% for the SESAM. The phase noise at low offset frequency range is 10 dB better which is predicted by our analysis

Also, since these noise conversion effects are due to the laser dynamics, changing to a low-noise pump source (e.g., diode pumped solid state lasers) will not help to eliminate these effects themselves. But of course, low-noise pump source will cause weaker excess noise due to these effects.

Regarding the role of quantum noise discussed in section 3.2 and pump RIN conversion discussed here, which one is stronger depends on the laser design. For our setup in section 3.2, the laser cavity has a large net dispersion which makes quantum noise much higher than the cavity with nearly zero dispersion. For the setup in this chapter, both laser cavities for NPR laser and SESAM laser have much smaller dispersion (close to zero) and higher pulse energy which all make quantum noise low and therefore the excess phase noise due to the pump RIN conversion is dominant.

4.4 *Summary*

In summary, we have experimentally characterized the linear noise conversion from the pump RIN to the RIN and phase noise of passively mode-locked fiber lasers at 1.5 μm. Two mode locking mechanisms, NPR and SESAM, are compared. It is found that the RIN and phase noise in both lasers (NPR laser and SESAM laser) are dominated by the noise converted from the pump RIN and thus can be predicted with the measured noise conversion ratios and pump RIN. Both lasers show similar noise conversion ratios from the pump RIN to the laser RIN with a plateau in the low-offset frequency region and a rapid decay in the high-offset frequency region. However, for the noise conversion ratio from the pump RIN to the laser phase noise, NPR laser exhibits a behavior similar to that for Ti : Sapphire lasers whereas

SESAM laser shows a much higher phase noise conversion ratio; the reason for this is found to be the slow saturable absorber effect of the SESAM.

5 Nonlinear noise conversion of the relative intensity noise from the pump to the mode-locked lasers

5.1 *Introduction*

As we have discussed, low noise mode-locked fiber lasers are compact and economical sources for frequency metrology [6], optical analog-digital conversion [8] and drift-free optical timing distribution [9]. The dynamics of mode-locked lasers has been widely investigated [24, 31-32, 34, 45, 69]. Properties of the relative intensity noise (RIN) have also been discussed by many researchers [70-75]. Dogru first proposed a theoretical model of RIN in a mode-locked hybrid soliton laser where a chirped fiber Bragg grating (CFBG) was used as a reflection mirror [70]. Lee experimentally examined the RIN characteristics of a frequency stabilized grating-coupled mode-locked semiconductor laser [71]. Newbury and his colleagues McFerran, Washburn and Swann have reported a series of analytical and experimental studies on noise in fiber-laser based frequency combs [73-74, 76]. Budunoglu also discussed the RIN of mode-locked fiber lasers with respect to different cavity dispersions maps [75].

Due to the noise coupled from the electrical circuits, the pump laser has been identified as a major source of noise for the mode-locked lasers. It has been reported that the RIN coupling from pump to laser can significantly deteriorate the noise performance of mode-locked lasers [49]. In the previous section, we have investigated the linear noise conversion from the pump RIN to the laser RIN. This linear noise conversion model can be described in Eq.(5.1)

$$S_{RIN}(f)=\frac{\sigma^2}{1+\frac{\gamma_{sp}^2-2\omega_{sp}^2}{\omega_{sp}^4}\omega_m^2+\frac{\omega_m^4}{\omega_{sp}^4}}S_{Pump-RIN}(f) \tag{5.1}$$

where $S_{RIN}(f)$ is the laser RIN power spectral density (PSD), $S_{Pump\text{-}RIN}(f)$ is the pump RIN PSD, the definition of other parameters can be found in Appendix A. The physical meaning of a linear noise conversion model is that the pump RIN at a given offset frequency f_M will only convert to the laser RIN at the same offset frequency f_M with a certain coefficient determined by Eq.(5.1). The laser RIN at other offset frequency will not be affected. This model is simple and easy for analysis and has been shown the validity and accuracy to predict the laser RIN and laser phase noise with measured pump RIN and linear noise conversion ratios when the pump RIN is the dominant noise source for the mode-locked lasers [67-68]. However, it is still meaningful to investigate the nonlinear noise conversion from the pump RIN to the laser RIN when the noise power in the pump RIN is high enough, e.g., the spurious peaks induced by the power line at the multiples of 50 Hz or by the electrical circuit of the pump diode driver at the multiples of a few kilo-Hertz.

This Chapter is the extension of Chapter 4. It discusses the nonlinear noise conversion phenomenon from the pump to the lasers. While the linear noise conversion in Chapter 4 explains how the low-power noise couples from the pump to the laser, the nonlinear noise conversion in Chapter 5 explains how the high-power noise spurs, e.g., due to the power line or other electrical noise, couples to the laser. In this Chapter, we investigate this nonlinear noise conversion effect by pump modulation, i.e., modulating the drive current of the pump diode, which has been verified as an effective method to study the RIN coupling phenomena [51]. The purpose of this work is to understand how a noise at f_M in the pump RIN converts to the noise at multiples of f_m in the laser RIN and why it behaves like this.

5.2 *Experimental setup and measurement results*

Single wall carbon nanotubes (SWCNTs) have been recently emerged as a versatile saturable absorber device for passively mode-locked lasers [25, 59, 77-80]. The laser under study is shown in Fig. 5.1. The SWCNTs used as saturable absorbers for mode locking operation are integrated into the cavity on the end of the fiber connector, as shown in the inset of Fig. 5.1. The individual SWCNTs are embedded in carboximethyl cellulose (CMC) film with special treatment [80]. Such composite provides a high damage threshold and low pump power for a self-started mode locking [59]. The transmittance at low optical power is ~39% and the saturable absorption is 12%~15% from the total loss. The relaxation time is ~300 fs [81]. A hybrid component integrating the functionalities of tap output (10%), isolator and 980/1550 WDM is utilized to simplify the cavity structure. The total cavity length is ~3.4 m and the corresponding fundamental repetition rate is ~58.7 MHz. The length of the single mode fiber is ~2.8 m with a dispersion of -0.022 ps^2/m. The length of Erbium doped fiber (LIEKKI Er110) is ~0.6 m with a dispersion of 0.012 ps^2/m. Thus the total dispersion is ~ -0.054 ps^2. The drive current of the pump (DC bias current in Fig. 5.1) is 170.1 mA, corresponding to a pump output power of 67 mW. The output power is -3.1 dBm with spectral width of 6.6 nm. The mode locking at fundamental repetition frequency can be maintained at the pump drive current from ~148 mA to ~200 mA, corresponding to the pump power of 52 mW to 78 mW. Modulation current (AC modulation current in Fig. 5.1) is applied to the 976 nm pump diode to simulate the pump RIN. A signal source analyzer (SSA, Rohde & Schwarz FSUP26) is used to measure the RIN spectrum of the laser output after optical-electrical conversion by a 2 GHz photo detector. To maintain the laser operation, the modulation current is adjusted from 1 mA to 6 mA, corresponding to

0.6~3.5% power fluctuation of the pump diode. The pump RIN is measured with the baseband noise measurement module of the SSA.

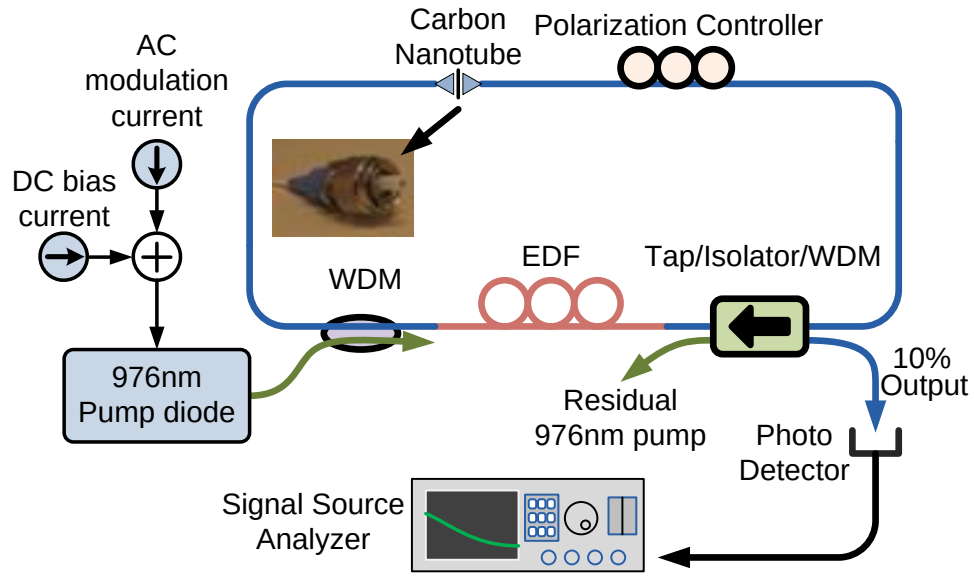

Fig. 5.1 Experimental setup of passively mode-locked fiber laser and pump modulation. A hybrid component integrating the functionalities of tap output (10%), isolator and 980/1550 WDM is utilized to simplify the cavity structure.

We first investigate the frequency response of the laser by modulating a sine wave to the pump bias current with different frequencies f_M. Due to the nonlinear response of the pump diode output with respect to the modulation signal, a given modulation current will generate a slightly different peak power at each f_M and some harmonics of f_M are generated. Therefore the pump noise generated by current modulation is a frequency comb noise, rather than a single frequency noise. The modulation frequency is experimentally varied from 2.5 kHz to 80 kHz with the modulation current fixed at 6 mA.

The RIN measurement results of the pump and the laser at 2.5 kHz and 20 kHz modulation are shown in Fig. 5.2 (a). It can be seen that different peak values are present for different f_M in the pump RIN PSD, together with harmonic

generation, which verifies the nonlinear response of the pump diode. Strong harmonics can be observed in the laser RIN PSD both for f_M = 2.5 kHz and f_M = 20 kHz, which suggests a nonlinear enhancement of the harmonic noise.

We define the total RIN conversion ratio as follows

$$C_{Tot}(kf_M) = S_{RIN}(kf_M) / S_{Pump-RIN}(f_M) \tag{5.2}$$

where $S_{RIN}(f)$ is the laser RIN PSD and $S_{Pump\text{-}RIN}(f)$ is the pump RIN PSD. The total RIN conversion ratio is the combined effect of the linear conversion ratio $C_{Lin}(f)$ and the nonlinear conversion ratio $T_{Nonlin}(f)$. The linear conversion ratio $C_{Lin}(f)$ is defined by

$$C_{Lin}(f_M) = S_{RIN}(f_M) / S_{Pump-RIN}(f_M) \tag{5.3}$$

And it is independent on the noise power by definition in the pump as shown in the previous chapter. The nonlinear conversion ratio $T_{Nonlin}(f)$ is noise power dependent. The total RIN conversion ratio at each harmonic frequency kf_M is summarized in Fig. 5.2 (b) for various values of f_M. It can be observed that the total RIN conversion ratio at a given frequency differs for varying harmonic orders, e.g. the 2nd harmonic frequency in the 2.5 kHz curve and the fundamental frequency in the 5 kHz curve have different total RIN conversion ratio. Thus, we can conclude that nonlinear conversion exists together with the linear conversion.

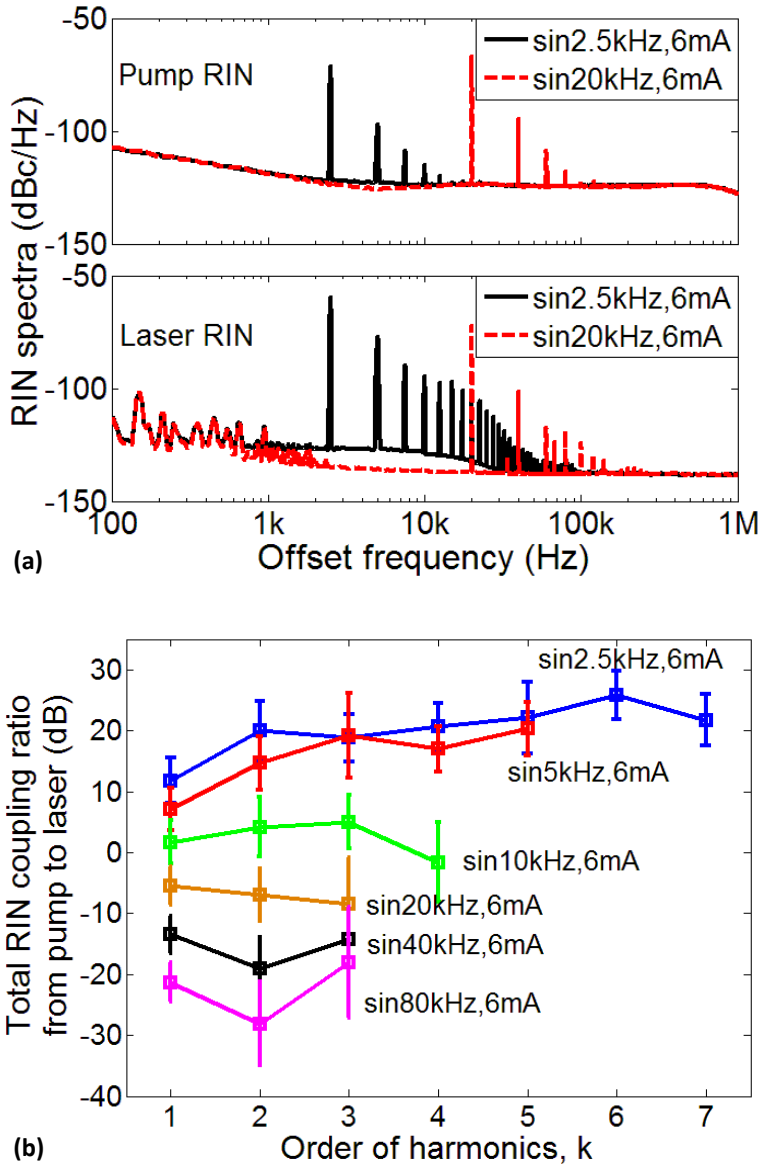

Fig. 5.2 (a) RIN spectra of the pump and the mode-locked laser when different modulation frequencies are applied to the pump; (b) Total RIN conversion ratio from pump to laser for different modulation frequencies and their harmonics

To investigate the linear RIN conversion and the nonlinear RIN conversion separately, we measure the total conversion ratio at 5 kHz sine wave modulation with different modulation currents, as shown in Fig. 5.3 (a). It can be seen that $C_{Tot}(f)$ at f_M (i.e., k = 1) is independent of the noise power (modulation current) and therefore the linear RIN conversion ratio $C_{Lin}(f_M)$ can be obtained based on the data from Fig. 5.2 (b) (values for k = 1 in each curve) and is summarized in Fig. 5.3 (b).

It is clearly observed that the linear conversion ratio decreases with the modulation frequency from 2.5 kHz to 80 kHz, which is consistent with the results we have got in the previous section. Similar phenomenon of the RIN conversion is also observed in the Ti : Sapphire mode-locked lasers and it is found this phenomenon is due to the pump induced fluctuation of the intracavity pulse energy [67-68]. When we further increase the modulation frequency to 1 kHz, even with very small modulation depth, the laser is strongly disturbed and the mode locking state will be broken very easily.

Square wave modulation is applied to further demonstrate the nonlinear RIN conversion in the mode-locked laser. For an ideal square wave with 50% duty-cycle, the power of even-order harmonics is naturally suppressed. A typical pump RIN spectrum for 5 kHz square wave modulation is given in Fig. 5.4 (a). The ~5dB steps at 100 kHz and 300 kHz offset frequencies are due to the finite resolution of the SSA, which can only be set to 300 Hz in the range of 100 kHz~300 kHz. It can be clearly observed that the power of even-order harmonics is suppressed by ~30 dB as compared to the adjacent odd-order harmonics in the pump RIN. However, after coupling to the laser RIN PSD in Fig. 5.4 (a), the power of even-order harmonics has been significantly enhanced. The total RIN conversion ratio with different modulation currents is summarized in Fig. 5.4 (b). The high total conversion ratio for even-order harmonics further confirms the nonlinear conversion from the pump RIN. For low modulation current, e.g., 1 mA, (corresponding to lower noise power), the total RIN conversion ratio is very similar to the linear RIN conversion ratio in Fig. 5.3 (b).

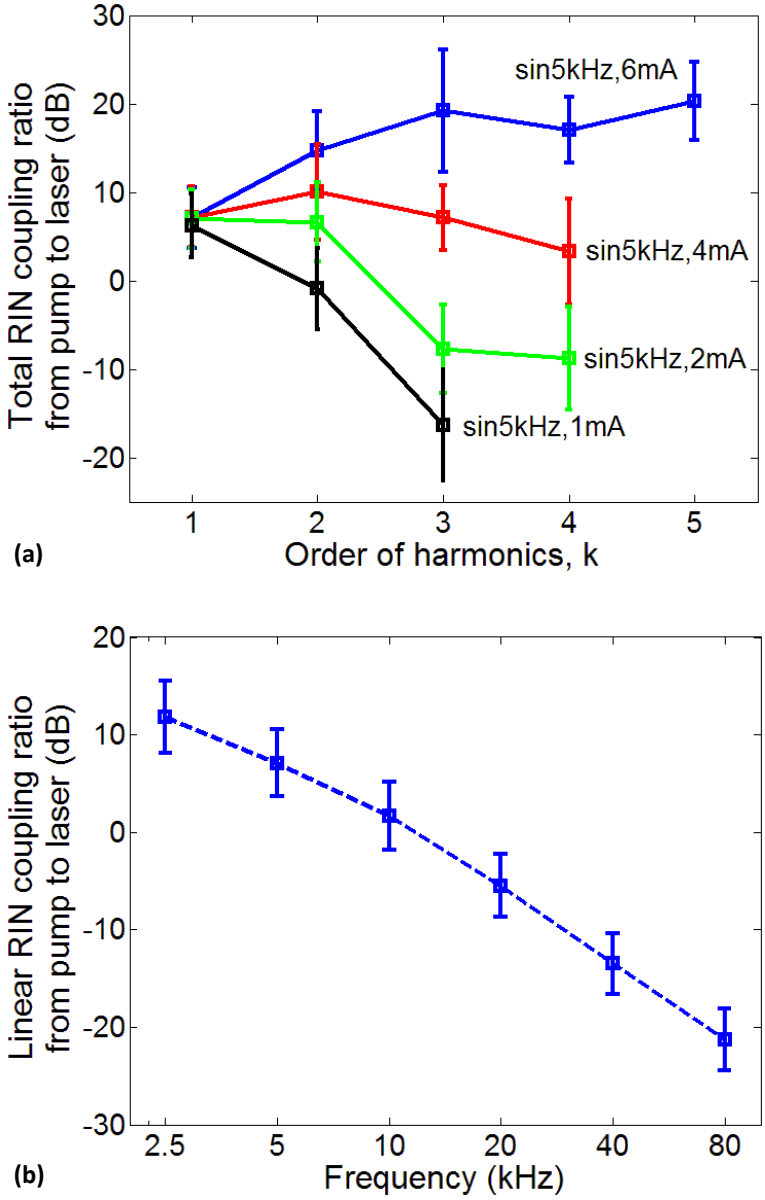

Fig. 5.3 (a) Total RIN conversion ratio from pump to laser at 5 kHz modulation for different modulation currents; (b) Linear RIN conversion ratio from pump to laser for different modulation frequencies

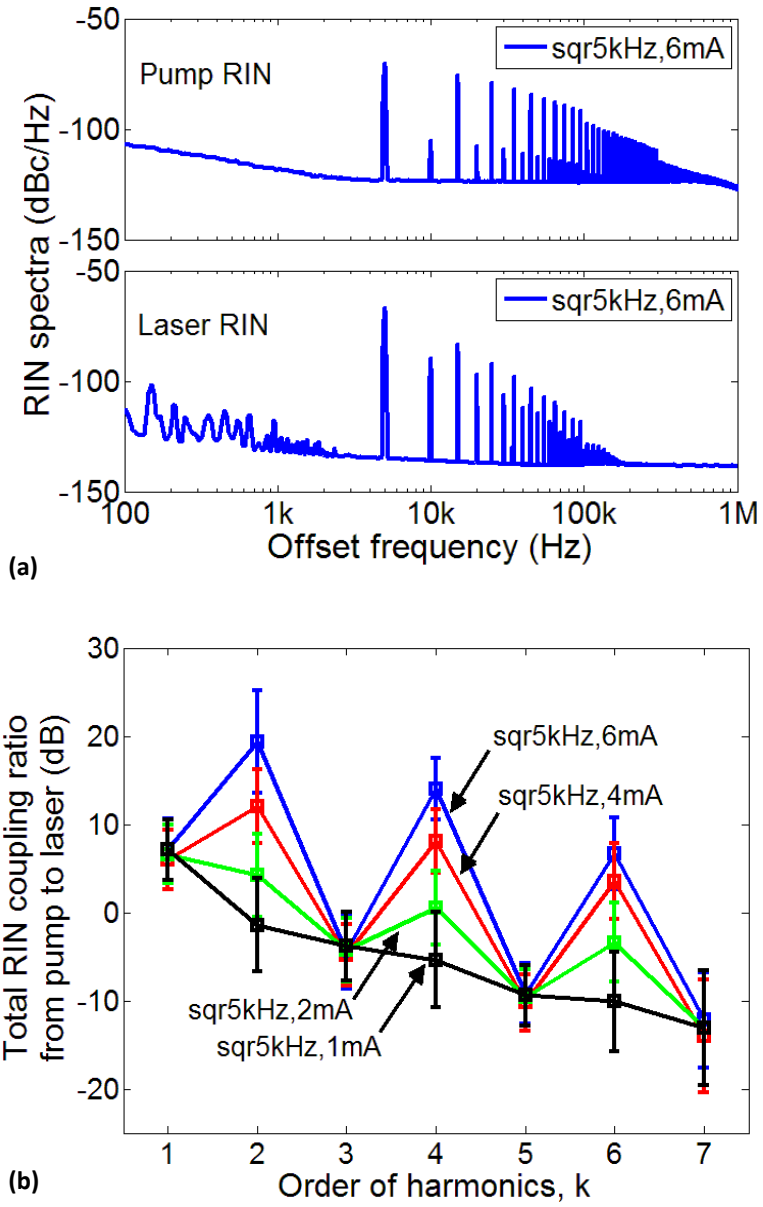

Fig. 5.4 (a) RIN spectra of pump and laser when square wave modulation is applied to the pump; (b) Total RIN conversion ratio from pump to laser with respect to different modulation current in a square wave modulation

5.3 *Model and physical explanation*

Here we propose an exponential decay model in order to describe the nonlinear RIN conversion from pump to laser. We only consider the nonlinearity generated by the fundamental modulation frequency in our model, whereas the effects of harmonics

are neglected due to their lower power levels. The effect of pump RIN on laser RIN can be described as follows

$$S_{RIN}(kf_M) = C_{Lin} \cdot S_{Pump-RIN}(kf_M) + T_{Nonlin}(kf_M) \cdot S_{Pump-RIN}(f_M) \tag{5.4}$$

where k=2,3,4… is the order of the harmonic frequency, $C_{Lin}(f_M)$ is the linear conversion ratio as depicted in Fig. 5.3 (b), $T_{Nonlin}(kf_M)$ is the nonlinear conversion ratio from the modulation frequency f_M to its harmonic frequency kf_M. The linear conversion ratio $C_{Lin}(f_M)$ has been fully studied in the previous chapter and can be expressed with a knee frequency [73]. The nonlinear conversion ratio $T_{Nonlin}(kf_M)$ can be expressed with an exponential decay model as follows

$$T_{Nonlin}(kf_M) = \eta e^{-\alpha k} \tag{5.5}$$

where η and α represent the basic conversion ratio and decay rate of the noise conversion, respectively. Both η and α are dependent on the noise power and the noise frequency. T_{Nonlin} can be obtained by subtracting the contribution of linear noise conversion in the laser RIN. Fig. 5.5 (a) gives the residual RIN contributed from nonlinear conversion and the values of η and α can be obtained by linear fit of each curve. The slope of the square-wave-modulation curves is smaller than that of the sine-wave-modulation curves because the power contained in the harmonics of the former is much higher than in the latter, resulting in greater nonlinear conversion from the harmonics in the former. The fitting lines of the exponential decay model (dashed lines) based on Eq.(5.4) and Eq.(5.5) are shown in Fig. 5.5 (b), which agree well with the experimental data (solid lines). If the power at f_M is low, the nonlinear RIN conversion term in Eq.(5.4) is then negligible and the RIN conversion becomes

a well-known linear point-to-point mapping process in Eq.(5.1) [73]. The extracted values of η and α are listed in Table 5.1.

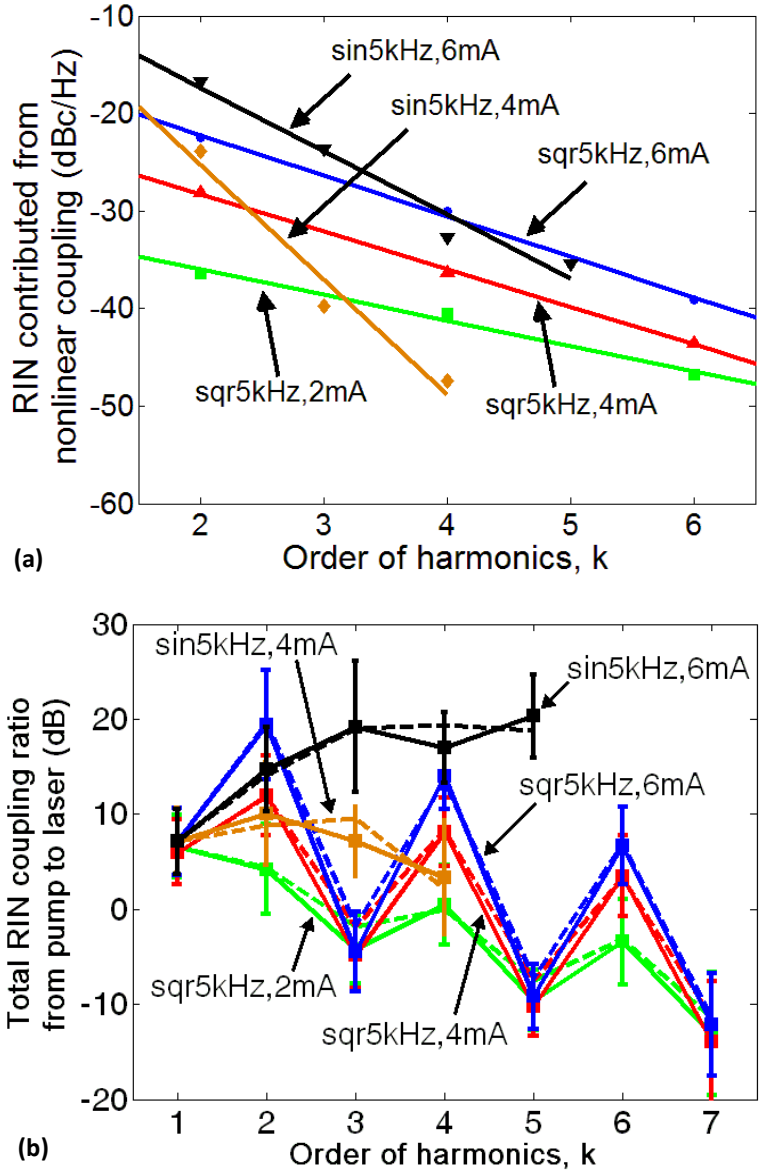

Fig. 5.5 (a) Residual RIN contributed from the nonlinear noise conversion. Markers are experimental data; solid lines are linear fit; (b) Fitting of exponential decay model (dashed lines) of the total RIN conversion ratio from pump to laser based on Eq.(5.4) and Eq.(5.5) and the experimental data (solid lines) of conversion ratio

Table 5.1 Values of η and α under different modulation waveform and modulation depth

Modulation	sin5kHz,6mA	sin5kHz,4mA	sqr5kHz,6mA	sqr5kHz,4mA	sqr5kHz,2mA
η	1.94	3.51	0.213	0.0459	0.00438
α	1.50	2.71	0.957	0.886	0.601

Here we give an explanation of the physical basis of nonlinear noise conversion phenomenon. For a three-level pumping scheme, the gain coefficient can be given by

$$g = \sigma(N_2 - N_1) \tag{5.6}$$

where σ is the transition cross section and N_2 and N_1 are the densities in the two energy states [4]. A weak modulation of the pump can be treated as a perturbation of the gain coefficient and modeled as a linear modulation of the gain coefficient as follows

$$g = g_0(1 + \varepsilon \sin 2\pi f_M t) \tag{5.7}$$

where g_0 is the gain coefficient without pump modulation, ε is the modulation depth and f_m is the modulation frequency. Then, for simplicity, the total gain for an EDF can be given by

$$G = \exp(g) = \exp(g_0 + \Delta g) = G_0 + \Delta G \tag{5.8}$$

where gain fluctuation ΔG can be further expanded as follows

$$\Delta G / G_0 = \exp(\Delta g) - 1$$
$$= g_0 \varepsilon \sin 2\pi f_M t + \frac{1}{2}(g_0 \varepsilon \sin 2\pi f_M t)^2 + \frac{1}{6}(g_0 \varepsilon \sin 2\pi f_M t)^3 + ... \quad (5.9)$$

It can be clearly seen that nonlinear terms exist. The direct calculation of the coefficients of the frequency components at kf_M (k=1, 2,…) is not very easy because, for example, $\sin^3 2\pi f_M t$ will also generate $\sin 2\pi f_M t$ term as well as $\sin 6\pi f_M t$ term. Numerically, Fourier series will help to determine the values of these coefficients. The calculated coefficients are plotted in Fig. 5.6 when the modulation depth ε varies from 0.01 to 0.1. Note that the modulation depth of pump modulation is 0.006~0.035 in our experiment. The vertical axis is plotted in logarithm scale. These coefficients show very good linearity and therefore verify the validity of the exponential decay model we have proposed in Eq.(5.5). Compared with the data of sine wave modulation in Fig. 5.5 (a), the behaviors of curves at different modulation depth are very similar. For sine wave modulation, basic coupling ratio η is mainly determined by the gain fiber properties and is nearly unchanged with the modulation depth ε. Decay rate α will inversely increase with the decrease of modulation depth ε. For square wave modulation, the mechanism is the same, but the power of odd-order harmonics is high enough to cause additional nonlinear noise conversion. A standard treatment is to calculate the noise coupling at each harmonic frequency independently and sum them together. For simplicity, we can also use an exponential decay model to fit the data at even-order frequency components. The fitting results in Fig. 5.5 (b) have demonstrated the accuracy of this simplified fitting treatment.

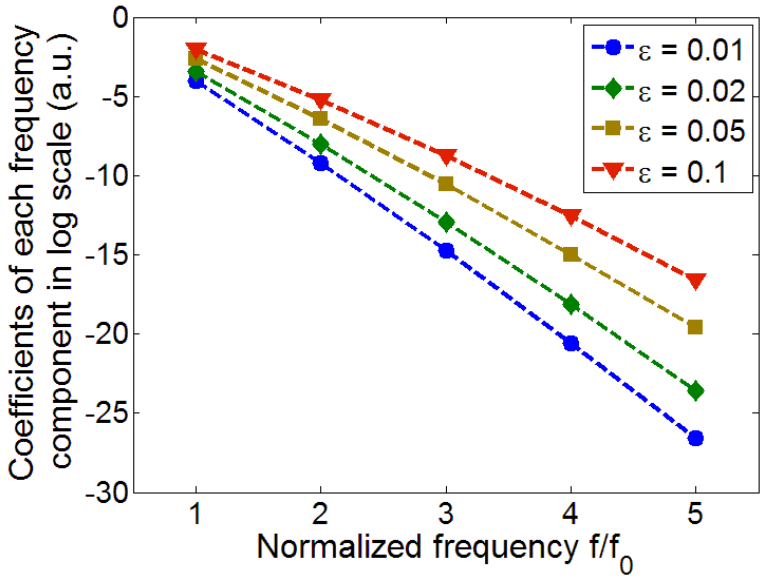

Fig. 5.6 Coefficients of each frequency component based on Eq.(5.9) at different modulation depth ε. The vertical axis is plotted in logarithmic scale. The coefficients show very good linearity which verifies the validity of the exponential decay model we have proposed in Eq.(5.5)

5.4 *Discussion*

From the theoretical analysis above, we also notice that this nonlinear noise conversion phenomenon is due to the properties of gain media. This means the nonlinear noise conversion we have observed in the fiber laser mode locked with carbon nanotubes may also be applied to the other kinds of lasers mode locked with different mechanisms. We demonstrate this assumption in an anomalously dispersive fiber laser mode locked at 1560nm with nonlinear polarization rotation (NPR). The square wave modulation is used and the results are shown in Fig. 5.7. The drive current of the pump is 238.7mA, corresponding to the pump power of ~103 mW. The modulation current is 1mA and the modulation depth is therefore 0.4%. The modulation depth is very small compared with the values we use in the CNT mode-locked laser because the NPR mode locking is very sensitive to the pulse power and the fluctuation of gain will significantly affect the NPR mode locking

operation. The offset frequency range in Fig. 5.7 is set from 1 kHz to 30 kHz because the modulation depth is so small that the laser RIN noise spurs after 30 kHz can hardly be observed. In Fig. 5.7, the values of the pump RIN at even-order harmonic frequencies are ~30 dB smaller than their adjacent odd-order harmonic frequencies. However the difference of the NPR laser RIN values between even order and adjacent odd order frequencies is less than 15 dB, which clearly demonstrates the existence of nonlinear noise conversion from the pump RIN.

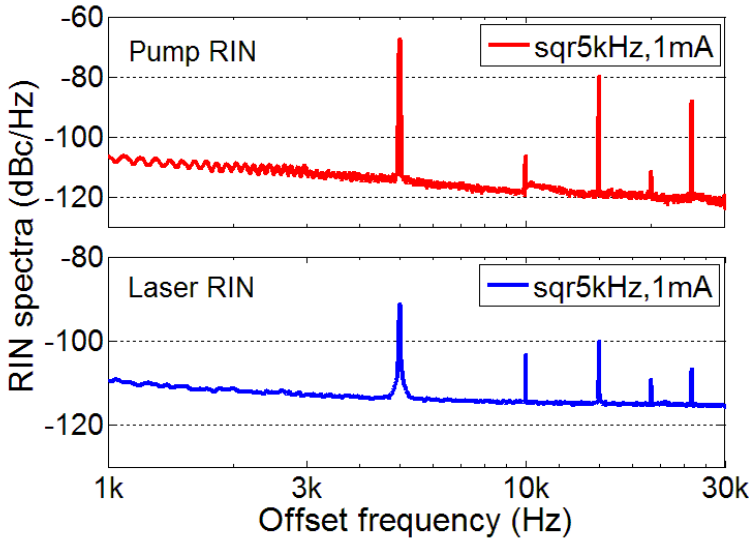

Fig. 5.7 RIN spectra of pump and NPR laser when square wave modulation is applied to the pump. The offset frequency range is set from 1kHz to 30kHz because the modulation depth is very small and laser RIN noise spurs after 30kHz are too small to be characterized.

Our theoretical and experimental results show that a periodic noise converted from the pump RIN will not only generate a periodic noise with same frequency in the RIN of the mode-locked lasers, but will also generate a bunch of harmonic frequency noise, and therefore significantly deteriorate the RIN of the mode-locked lasers. For high-precision applications of mode-locked lasers, this effect will surely limit the performance of the system, e.g., to reduce the accuracy of frequency metrology, the effective number of bit in optical sampling and the timing precision

in timing distribution system. The source of the periodic noise can be from the noise in power line, the internal noise from the drive circuit and/or the noise coupled from the free space.

5.5 *Summary*

In summary, the nonlinear RIN conversion from the pump to the CNT-based mode-locked laser is investigated with the pump modulation technique. The linear RIN conversion ratio from the pump to the mode-locked laser is independent of the noise power which is consistent with our results described in the previous chapter. The nonlinear RIN conversion generates additional noise power at various harmonics kf_M with respect to the fundamental modulation frequency f_M. The nonlinear conversion ratio is determined by the noise power at f_M, and exponentially decreases with an increase in harmonic number k. A square wave pump modulation clearly illustrates this nonlinear noise conversion phenomenon. An exponential decay model is proposed to describe the behavior of the nonlinear RIN conversion. Physical explanation of the nonlinear noise conversion effect from the view of gain modulation is presented. The theoretical analysis demonstrates the existence of nonlinear noise coupling and verifies the validity of exponential decay model.

6 Excess phase noise conversion induced by photodetectors

6.1 *Introduction*

Low-noise mode-locked lasers have attracted intense interest for various applications including optical sampling [8], low-noise microwave signal synthesis [11, 15, 82-84] and high-precision clock distribution [9-10]. Many researchers have discussed the noise in the mode-locked lasers [31-32, 34-36, 45]. Based on their work, various techniques have been proposed to reduce the noise in the mode-locked lasers. These techniques include the use of a slab coupled optical amplifier, cavity filter, optimization of cavity loss, optimization of cavity dispersion and mode locking state, etc. [23-24, 35-36, 53, 57, 65, 85]. Meanwhile, noise measurement has become more and more accurate [46, 66, 82-83] and the latest optical cross correlation method can provide attosecond accuracy [44, 56] and -200 dBc/Hz equivalent phase noise level in the phase noise spectrum [53].

To makes our work more comprehensive regarding the application of low-noise mode-locked lasers, we discuss the low-noise microwave synthesis from the mode-locked lasers in this chapter. When we use a mode-locked laser to generate microwave signal, the noise of microwave signal does not only depend on the laser noise but also the noise from the photodetectors (PDs). It is well known that photodetectors introduce excess noise due to the power dependent pulse broadening and pulse delay [83]. The power dependent pulse broadening leads to the noise conversion from the optical relative intensity noise (RIN) to the electrical pulse width jitter (PWJ) and to the electrical relative amplitude noise (RAN). The power dependent pulse delay leads to the noise conversion from the optical RIN to the

electrical phase noise. The RIN-to-phase-noise conversion has been discussed both in time domain and in frequency domain [16, 86-87]. Here, the electrical RAN includes the electrical RAN of the pulse amplitude and the electrical RAN of the signal at repetition frequency $f_{R.}$ The electrical RAN of the pulse amplitude means the amplitude noise of the pulse peak voltage and the electrical RAN at f_R means the amplitude noise of the component at repetition frequency f_R (the amplitude at f_R can be obtained as the square root of the RF power at f_R). These two RANs are not the same because the electrical PWJ also contributes to the electrical RAN at f_R which is the RAN that can be experimentally measured.

In the above context, many novel designs have been proposed to overcome the excess phase noise and these have demonstrated a residual timing jitter of the extracted RF signals as low as a few femtoseconds [11-12]. However, the RIN-to-PWJ (here and subsequent mentions of PWJ refer to the PWJ of the electrical pulses) and RIN-to-RAN (including the electrical RAN of the pulse amplitude and the electrical RAN of the signal at repetition frequency $f_{R,}$ or RAN at f_R for short) conversion are not fully understood yet. Also, the relation between the electrical RAN of the pulse amplitude and the electrical RAN at f_R is unclear. Further, previous work on PWJ measurement of the optical pulses focuses on pulse widths larger than the rise time of the photodetectors and neglects the excess noise in the photodetectors [40, 42, 88]. Due to the ultralow quantum limited noise of the femtosecond lasers, the mode-locked lasers used in microwave signal synthesis usually have a pulse width much shorter than the rise time of the photodetectors which means the output of the photodetector can be regarded as its impulse response. Therefore it is meaningful to develop a method that can completely characterize these kinds of noise conversion from photodetectors, that is, RIN-to-PWJ, RIN-to-

RAN (the electrical RAN of the pulse amplitude), RIN-to-RAN (the electrical RAN at f_R) and RIN-to-phase-noise conversion, for microwave signal synthesis application based on femtosecond mode-locked laser. Also, it is still unclear how the pulse width and peak power of the incident optical pulses affects these 4 kinds of noise conversion. Moreover, we notice that in many applications of femtosecond lasers in microwave signal synthesis, a wideband photodetector is usually used. This may inherently suggest that a wideband photodetector should have a low RIN-to-phase-noise conversion. However, our comparison of two photodetectors with 10 GHz and 2 GHz bandwidth respectively, shows that this is not necessarily true and the saturation power of the photodetectors may play an even more important role to achieve low RIN-to-phase-noise conversion.

In this chapter, we discuss the detailed characterization of RIN-to-PWJ, RIN-to-RAN (including the electrical RAN of the pulse amplitude and the RAN at f_R) and RIN-to-phase-noise conversion in the photodetectors when detecting the optical pulses from femtosecond mode-locked lasers. The noise conversion ratios are experimentally determined by analyzing the electrical pulse profiles and measuring the power at f_R under different input optical powers. Theoretical analysis which considers the pulse asymmetry and uses the Fourier series analysis, is also performed to describe the relation among all these noise conversion ratios and to enable one to predict the electrical RAN and phase noise power spectral densities (PSDs). The effect of the incident optical pulse width and peak power of the optical pulses and the effect of the saturation power of the photodetectors are also investigated. Finally, the results of the above studies are used to provide many useful guidelines for low-noise photodetection for microwave signal synthesis application. The discussion in this paper is limited to the condition that the optical

pulse width is much smaller than the rise time of the photodetectors and therefore the output of the photodetector can be regarded as its impulse response.

6.2 *Theoretical model of a noisy electrical pulse train*

A noisy electrical pulse train obtained from photodetection of an optical pulse train can be expressed by

$$V = V_0 \sum_{n=-\infty}^{+\infty} (1+\Delta a_n) f\left(\frac{t - nT_R + \Delta t_n}{\tau + \Delta \tau_n}\right) \tag{6.1}$$

where V_0 is the pulse amplitude (voltage), $f(t/\tau)$ is the normalized amplitude profile of a single pulse, τ is the average pulse width, T_R is the time period, Δa_n is the electrical RAN of pulse amplitude, Δt_n is the timing jitter and $\Delta\tau_n/\tau$ is the relative electrical PWJ. Eq.(6.1) can be Taylor expanded so that

$$V / V_0 = \left(\sum_{n=-\infty}^{+\infty} f\left(\frac{t-nT_R}{\tau}\right)\right)(1+\Delta a(t)) + \left(\sum_{n=-\infty}^{+\infty} \dot{f}\left(\frac{t-nT_R}{\tau}\right)\right)\frac{\Delta t(t)}{\tau}$$
$$-\left(\sum_{n=-\infty}^{+\infty} \dot{f}\left(\frac{t-nT_R}{\tau}\right)\frac{t-nT_R}{\tau}\right)\frac{\Delta \tau(t)}{\tau} \tag{6.2}$$

where $\Delta t(t)=\Delta t_n$, $(nT_R\text{-}T_R/2) < t \leq (nT_R+T_R/2)$, is the continuous expression of Δt_n and the same definition can be applied to $\Delta\tau(t)$ and $\Delta a(t)$, and $\dot{f}$ is the derivative of the normalized time $x = t/\tau$. So we have $\dot{f} \equiv df(x)/dx = \tau df(t/\tau)/dt$ (for simplicity, we use Δt, $\Delta\tau$ and Δa to represent the corresponding time varying quantities in the subsequent expressions). All higher order noise terms have been neglected and only first order noise terms are considered. More details of the derivation of Eq.(6.2) can be found in the works of von der Linde [45] or L. P. Chen

[37]. The pulse profile is not symmetric and we need to consider both the even part (defined as f_e) and the odd part (defined as f_o) of the pulse profile f, where $f = f_e + f_o$. The periodicity of the terms in Eq.(6.2) means that these can be expanded into a Fourier series as follows:

$$\sum_{n=-\infty}^{+\infty} f_e(\frac{t-nT_R}{\tau}) = \frac{a_0}{2} + \sum_{k=1}^{+\infty} a_k \cos k\omega_R t \tag{6.3}$$

$$\sum_{n=-\infty}^{+\infty} \dot{f}_e(\frac{t-nT_R}{\tau})\frac{1}{\tau} = -\sum_{k=1}^{+\infty} a_k k\omega_R \sin k\omega_R t \tag{6.4}$$

$$\sum_{n=-\infty}^{+\infty} \dot{f}_e(\frac{t-nT_R}{\tau})\frac{t-nT_R}{\tau} = -\frac{a_0}{2} + \sum_{k=1}^{+\infty} (c_k - a_k)\cos k\omega_R t \tag{6.5}$$

$$\sum_{n=-\infty}^{+\infty} f_o(\frac{t-nT_R}{\tau}) = \sum_{k=1}^{+\infty} b_k \sin k\omega_R t \tag{6.6}$$

$$\sum_{n=-\infty}^{+\infty} \dot{f}_o(\frac{t-nT_R}{\tau})\frac{1}{\tau} = \sum_{k=1}^{+\infty} b_k k\omega_R \cos k\omega_R t \tag{6.7}$$

$$\sum_{n=-\infty}^{+\infty} \dot{f}_o(\frac{t-nT_R}{\tau})\frac{t-nT_R}{\tau} = \sum_{k=1}^{+\infty} (d_k - b_k)\sin k\omega_R t \tag{6.8}$$

where $\omega_R = 2\pi f_R = 2\pi/T_R$ is the fundamental repetition angular frequency. The definition and calculation of the Fourier coefficients a_k to d_k are given in the Appendix. The final expression of a noisy electrical pulse train can be written as

$$\begin{aligned} V/V_0 &= \frac{a_0}{2}(1 + \Delta a + \frac{\Delta\tau}{\tau}) + \sum_{k=1}^{+\infty} (I_k \cos k\omega_R t - Q_k \sin k\omega_R t) \\ &= \frac{a_0}{2}(1 + \Delta a + \frac{\Delta\tau}{\tau}) + \sum_{k=1}^{+\infty} A_k \cos(k\omega_R t + \varphi_k) \end{aligned} \tag{6.9}$$

where I_k and Q_k are the amplitudes of two orthogonal frequency components respectively and their expressions are given by

$$I_k = a_k(1+\Delta a) - (c_k - a_k)\frac{\Delta\tau}{\tau} + b_k\omega_R\Delta t \tag{6.10}$$

$$Q_k = -b_k(1+\Delta a) + (d_k - b_k)\frac{\Delta\tau}{\tau} + a_k k\omega_R\Delta t \tag{6.11}$$

The total amplitude A_k and phase φ_k can then be calculated as

$$\begin{aligned} A_k &= \sqrt{I_k^2 + Q_k^2} \\ &= \sqrt{(a_k^2 + b_k^2)(1+2\Delta a) + (a_k^2 - a_k c_k + b_k^2 - b_k d_k)\frac{2\Delta\tau}{\tau}} \\ &\approx \sqrt{a_k^2 + b_k^2}\left(1 + \Delta a + \frac{a_k^2 - a_k c_k + b_k^2 - b_k d_k}{a_k^2 + b_k^2}\frac{\Delta\tau}{\tau}\right) \\ &\equiv \sqrt{a_k^2 + b_k^2}\left(1 + \Delta a + C_a\frac{\Delta\tau}{\tau}\right) \end{aligned} \tag{6.12}$$

$$\begin{aligned} \varphi_k &= \tan^{-1} Q_k / I_k \\ &= \tan^{-1}\frac{-b_k(1+\Delta a) + (d_k - b_k)\frac{\Delta\tau}{\tau} + a_k k\omega_R\Delta t}{a_k(1+\Delta a) - (c_k - a_k)\frac{\Delta\tau}{\tau} + b_k\omega_R\Delta t} \\ &\approx \tan^{-1}\left(-\frac{b_k}{a_k}\right) + k\omega_R\Delta t + \frac{a_k d_k - b_k c_k}{a_k^2 + b_k^2}\frac{\Delta\tau}{\tau} \\ &\equiv \tan^{-1}\left(-\frac{b_k}{a_k}\right) + k\omega_R\Delta t + C_\varphi\frac{\Delta\tau}{\tau} \end{aligned} \tag{6.13}$$

where the relation $d\tan^{-1}(x)/dx = 1/(1+x^2)$ is used. The two coefficients C_a and C_φ are defined as:

$$C_a = \frac{a_k^2 - a_k c_k + b_k^2 - b_k d_k}{a_k^2 + b_k^2} \tag{6.14}$$

$$C_\varphi = \frac{a_k d_k - b_k c_k}{a_k^2 + b_k^2} \tag{6.15}$$

Since A_k (k=1) in Eq.(6.12) represents the amplitude of the signal at f_R, the noise terms in A_k (k=1) represent the electrical RAN at f_R. As mentioned earlier, Δa is the electrical RAN of the pulse amplitude and $\Delta\tau/\tau$ is the electrical PWJ. Therefore Eq. (6.12) indicates that

$$RAN_R = RAN_P + C_a \cdot PWJ \tag{6.16}$$

where RAN_R is the electrical RAN at f_R and RAN_P is the electrical RAN of the pulse amplitude. If we denote the RIN-to-RAN (RAN at f_R) conversion ratio as r_{RAN_R}, RIN-to-RAN (pulse amplitude) conversion ratio as r_{RAN_P} and RIN-to-PWJ conversion ratio as r_{PWJ}, Eq.(6.16) can be written as

$$r_{RAN\_R} = r_{RAN\_P} + C_a r_{PWJ} \tag{6.17}$$

The expressions for r_{RAN_R}, r_{RAN_P} and r_{PWJ} are given by

$$r_{RAN\_R} = \frac{dV_R / V_R}{dP / P} = \frac{P}{V_R}\frac{dV_R}{dP} \tag{6.18}$$

$$r_{RAN\_P} = \frac{dV_P / V_P}{dP / P} = \frac{P}{V_P}\frac{dV_P}{dP} \tag{6.19}$$

$$r_{PWJ} = \frac{d\tau / \tau}{dP / P} = \frac{P}{\tau}\frac{d\tau}{dP} \tag{6.20}$$

where V_R is the amplitude at f_R, P is the input optical power, V_P is the electrical pulse amplitude and τ is the electrical pulse width. The values of V_P and τ can be obtained by analyzing the electrical pulse profiles measured using a high-speed oscilloscope and V_R can be obtained as the square root of the RF power at f_R measured by an RF spectrum analyzer. That means the left hand side and the right hand side of Eq.(6.17) can be obtained independently. Thus one can verify the validity of Eq.(6.17).

Suppose the PSD of the laser RIN is S_{RIN_laser}. Then the PSD of the electrical RAN at f_R, the PSD of the electrical RAN of pulse amplitude, and the PSD of PWJ are given by

$$S_{RAN\_R} = r_{RAN\_R}^2 S_{RIN\_laser} \tag{6.21}$$

$$S_{RAN\_P} = r_{RAN\_P}^2 S_{RIN\_laser} \tag{6.22}$$

$$S_{PWJ} = r_{PWJ}^2 S_{RIN\_laser} \tag{6.23}$$

In a similar manner, the phase at f_R consists of three parts: 1) a pulse-profile-related term $\tan^{-1}(-b_k/a_k)$ – since the pulse profile is related to the input optical power, this term in fact contains the information about the laser RIN; 2) the original phase noise (or timing jitter) of the laser; and 3) the PWJ induced noise with a coefficient C_φ. It has been shown that the RIN-to-phase-noise conversion ratio r_{PN} can be obtained by Fourier transformation of the electrical impulse response of a photodetector to extract the phase and then differentiating the phase with respect to the input optical power [16]. Therefore, the expression for r_{PN} (with the units of rad) is given by

$$r_{PN} = \frac{d\varphi}{dP/P} = -P\frac{d\tan^{-1}(b_k/a_k)}{dP} \approx -P\frac{d(b_k/a_k)}{dP} \tag{6.24}$$

where the timing jitter and the PWJ in Eq.(6.13) are assumed zero because we use the average phase of the electrical pulses. The measured electrical phase noise PSD is then given by

$$S_\varphi = S_{\varphi\_laser} + (r_{PN} + C_\varphi r_{PWJ})^2 S_{RIN\_laser} \tag{6.25}$$

For microwave signal synthesis applications, femtosecond mode-locked lasers are generally chosen as the pulse sources due to their ultra-low quantum limited noise. Therefore, we are more interested in the pulses with a duty cycle $\sigma = \tau/T$ less than 1%. Under this condition, the Fourier coefficient a_k is much greater than the remaining three coefficients b_k to d_k at f_R, i.e., k=1, and thus the coefficient $C_a \approx 1$ and $C_\varphi \approx 0$. Eqs.(6.17) and (6.25) can thereby be simplified as

$$r_{RAN\_R} = r_{RAN\_P} + r_{PWJ} \tag{6.26}$$

$$S_\varphi = S_{\varphi\_laser} + r_{PN}^2 S_{RIN\_laser} \tag{6.27}$$

An example of C_a and C_φ values at f_R calculated from the measured electrical pulse profiles for different input optical powers entering a 10 GHz photodetector is shown in the inset of Fig. 6.2 in the next section.

6.3 *Measurement of RIN-to-PWJ, RIN-to-RAN and RIN-to-Phase-Noise conversion ratios*

The impulse response method proposed by J. Taylor [16] has been proven to be an effective method to characterize the RIN-to-phase-noise conversion in the photodetectors. As shown in Fig. 6.1, we use a similar setup to measure the RIN-to-PWJ and RIN-to-RAN (including the electrical RAN of pulse amplitude and the electrical RAN at f_R) conversion in the photodetectors. A homemade 66.1 MHz mode-locked fiber laser centered at 1566 nm is used as the pulse source generating a pulse train with a spectral width of ~11 nm and an average optical power of 2.5 mW. A variable optical attenuator (VOA) controls the optical power incident on a 10 GHz InGaAs photodetector (EOT ET3500F). The temporal profile of the electrical pulses after photodetection is measured by a high-speed real-time oscilloscope (LeCroy

SDA820Zi-A) with a bandwidth of 20 GHz. The oscilloscope has a real-time sampling rate of 40 Gsamples/s and works under RIS mode which has an equivalent sampling rate of 200 Gsamples/s, corresponding to a time interval of 5 ps. The timing accuracy of the oscilloscope is ~250 fs. The nonlinearity in the amplitude response of the oscilloscope is found to be small by comparing the waveforms obtained with and without a 10 dB electrical attenuator between the photodetector and the oscilloscope. The RIN and phase noise at the repetition frequency are measured by a signal source analyzer (SSA, R&S FSUP26). A low pass filter (LPF) and low noise amplifier (LNA) are inserted before the SSA in order to extract the frequency component at the repetition frequency and to provide enough input power for SSA noise measurement. The noise floor of SSA is below -155 dBc/Hz at high frequency range for the conditions in our experiment. So the equipments used in the experiment can provide reliable measurements.

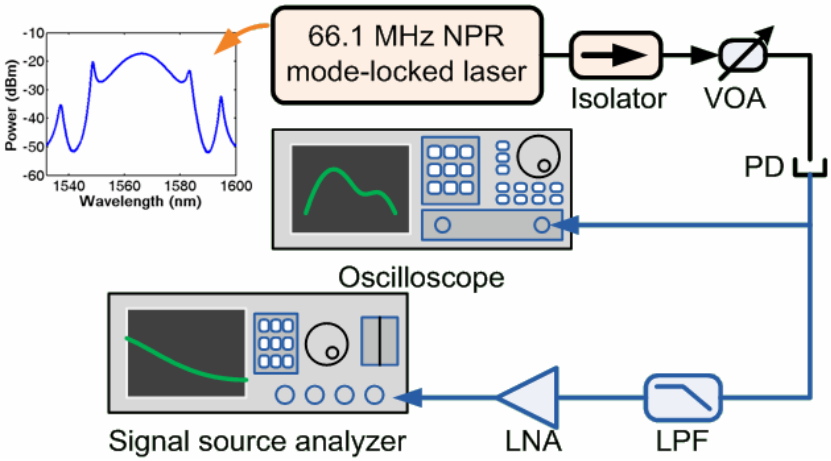

Fig. 6.1 Experimental setup for the measurement of noise conversion in the photodetector. VOA: variable optical attenuator; PD: photodetector; LPF: low pass filter; LNA: low noise amplifier

6.3.2 RIN-to-PWJ and RIN-to-RAN conversion

The measured electrical pulse profiles are shown in Fig. 6.2 as the input optical power varies from 0.1 mW to 2.1 mW. The inset in Fig. 6.2 shows the calculated coefficients C_a and C_φ at f_R, confirming that $C_a \approx 1$ and $C_\varphi \approx 0$ for all values of input power. Fig. 6.3 (a) shows the corresponding electrical pulse width and electrical pulse amplitude values. With these data, the RIN-to-PWJ and the RIN-to-RAN (pulse amplitude) ratios r_{PWJ} and r_{RAN_P} can be calculated according to Eq.(6.20) and (6.19), respectively; the results are shown as red and green curves in Fig. 6.3 (b). The derivatives required in Eq.(6.20) and (6.19) are calculated using the central difference of the data in Fig. 6.3 (a). The smooth curves for the conversion ratios are obtained by using third-order polynomial fit. The signal amplitude at f_R is measured using an RF spectrum analyzer and the RIN-to-RAN ratio at f_R, r_{RAN_R}, calculated according to Eq.(6.18), is shown as dashed black curve in Fig. 6.3 (b). It can be seen that the measured values of r_{RAN_R} are very similar to those calculated by summing r_{PWJ} and r_{RAN_P} according to Eq.(6.26) (blue curve); this confirms the validity of the analysis presented in the theoretical part. The discrepancy in the two sets of values of r_{RAN_R} arises due to two reasons: one is the measurement error of the electrical pulse profiles and the input optical powers because the dP term in the denominator of Eqs.(6.18) - (6.20) amplifies the error in P and the P in the numerator amplifies the errors in $d\tau/\tau$ and dV/V when P is large. This explains the relatively larger discrepancy for P > 1.5 mW. The other reason is the bandwidth limitation (~17 GHz) set by the oscilloscope. The inset in Fig. 6.3 (a) shows the envelope of the RF spectra of the electrical signal from the photodetector at 0.1 mW and 2 mW input powers. It can be seen that for 0.1 mW input power, the RF power levels at 15 GHz ~ 20 GHz are still comparatively high; the suppression of these power levels

leads to pulse broadening and thus an underestimation of the PWJ. On the other hand, for 2 mW input power, the RF power levels after 2 GHz decrease quickly. Therefore, the bandwidth limitation effect is stronger when the input power is low. One more example of r_{RAN_R}, r_{RAN_P} and r_{PWJ} calculations is given in Fig. 6.8 in the next section in which the values of the optical powers are recorded with a higher accuracy (1 μW) and a better match between r_{RAN_R} and $r_{RAN\_P}+r_{PWJ}$ is found at high input power range (0.6 mW ~ 2 mW). The discrepancy at input power less than 0.6 mW still exists due to the limitation of the oscilloscope.

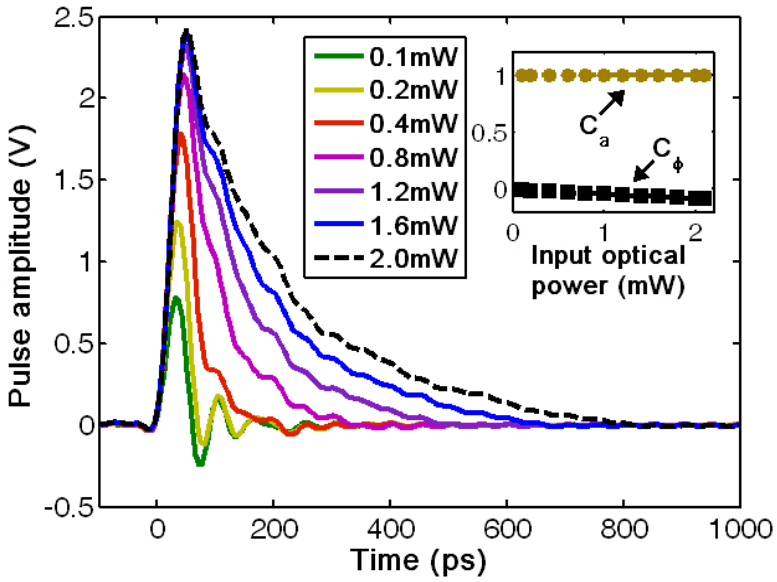

Fig. 6.2 Electrical pulse profiles for different input optical powers entering the 10 GHz photodetector. Inset: Coefficients C_a and C_φ at repetition frequency f_R for different input optical powers

Since the values of r_{RAN_R} calculated by summing r_{PWJ} and r_{RAN_P} are more sensitive to the measurement error than the one directly obtained from the measurement of the RF power at f_R, we use the latter to estimate the laser RIN PSD from the measured electrical RAN PSDs at f_R at various input optical powers based on Eq.(6.21). The estimated laser RIN PSD is shown in Fig. 6.4 and the PSD values at 1 kHz and 10 kHz offset frequencies are also plotted for comparison. With the

laser RIN PSD known, one can easily calculate the PSD of PWJ and RAN of pulse amplitude using Eq.(6.22) and (6.23). As can be seen, good agreement is obtained between the calculated and measured values.

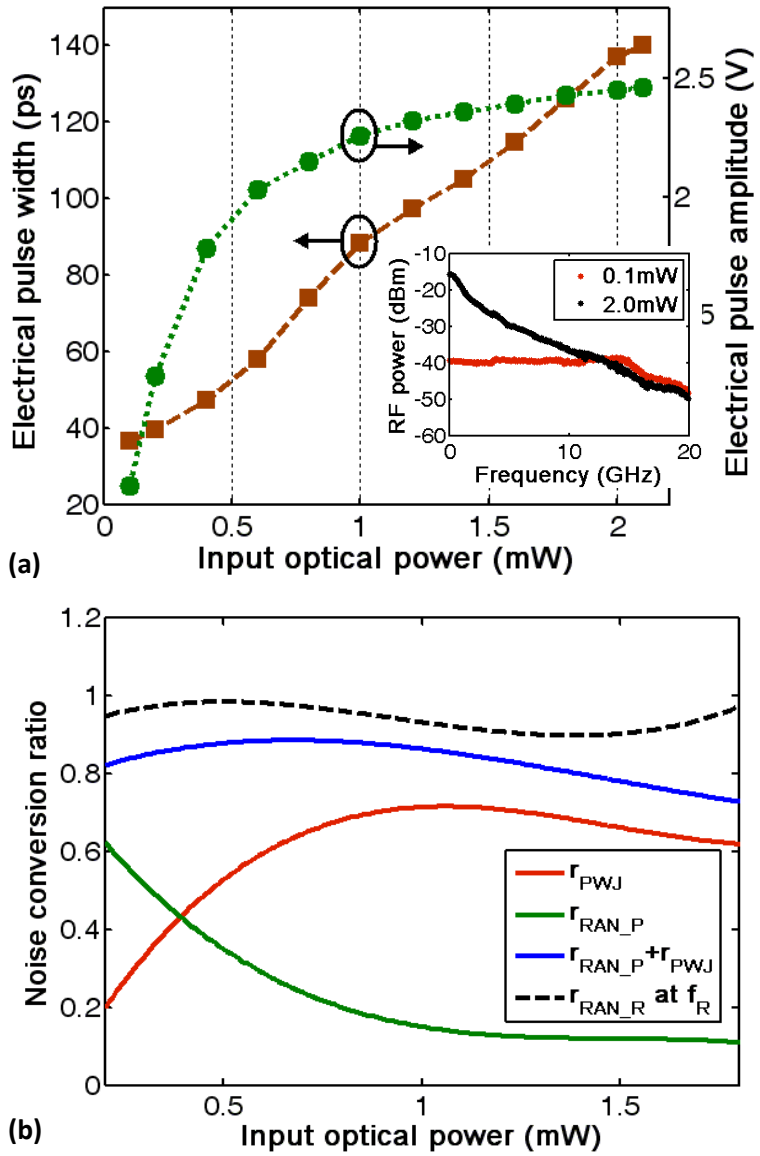

Fig. 6.3 (a) Electrical pulse widths and amplitudes. (b) Noise conversion ratios RIN to PWJ (r_{PWJ}), RIN to RAN of pulse amplitude (r_{RAN_P}) and RIN to RAN at f_R (r_{RAN_R}). Inset in (a) is the envelope of the RF spectra of the electrical signals from the photodetector at 0.1 mW and 2 mW input power

The output electrical power of the photodetector is determined by the input optical power and the quantum efficiency (or responsivity) of the photodetector.

This limits the total output power of the photodetector to a few milli-watts considering a quantum efficiency of 1 and a maximum allowed input power of 10 mW. The power levels at each frequency component are thus even lower. Also, the power levels at lower frequencies increase quickly with the increasing input power whereas the power levels at higher frequencies increase very slow or even decrease due to the photodetector saturation effect (see inset of Fig. 6.3 (a)). Therefore if one wants to get high output power at a certain frequency one may increase the input optical power at the expense of a higher RIN-to-phase-noise conversion (will be discussed in the next section) and a low-noise post-amplifier may also be required.

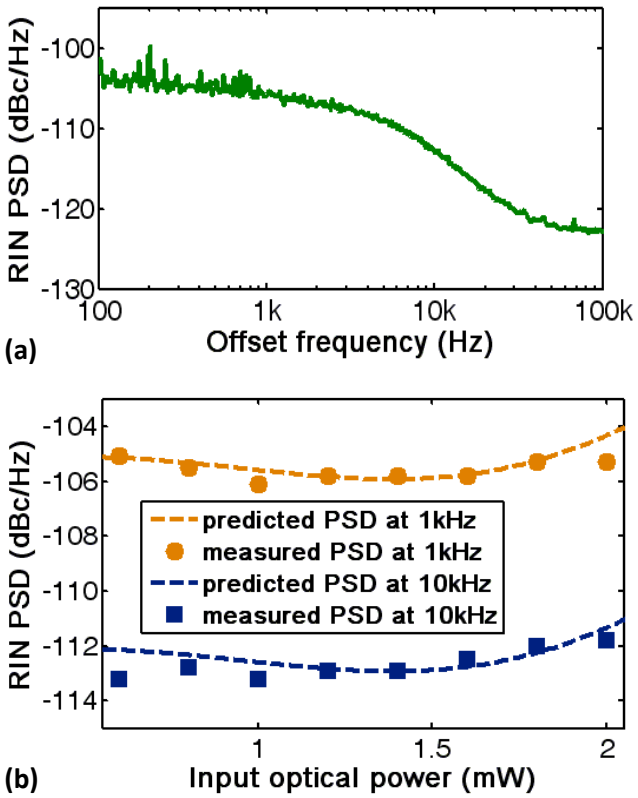

Fig. 6.4 (a) Laser RIN power spectral density and (b) the PSD values at 1 kHz and 10 kHz offset frequencies (circle and square markers) compared with the predicted values (dashed lines) with different input optical powers. The predicted curves are calculated by using r_{RAN_R} obtained from the measurement of RF power at f_R and Eq.(6.21).

6.3.3 RIN-to-phase-noise conversion

The RIN-to-phase-noise conversion ratio can be obtained by analyzing the phase values of the electrical pulses measured for different input power levels. The phase values calculated by Eq.(6.13) (note that the timing jitter and PWJ terms in Eq. (6.13) are assumed zero because we are considering the average phases) are shown in Fig. 6.5 (a). We calculate the phase values for frequencies ranging from the repetition frequency f_R = 66.1 MHz to the 151th harmonic 151f_R = 9.98 GHz. Then we use a fourth-order polynomial to fit the phase values and calculate the corresponding RIN-to-phase-noise conversion ratios r_{PN} (absolute values) based on Eq.(6.24); these results are shown in Fig. 6.5 (b). Fig. 6.5 (c) gives three examples of the RIN-to-phase- noise conversion ratios at 66.1 MHz, 1983 MHz and 9981.1 MHz, respectively, which correspond to the three dashed lines in Fig. 6.5 (b). These ratios are exactly the same as the ones calculated by the method of direct Fourier transformation of the pulse profiles used in Ref. [16].

Knowing the RIN-to-phase-noise conversion ratio r_{PN}, we can predict the measured phase noise PSD according to Eq.(6.27). The laser phase noise PSD is the PSD measured at low input power where the value of r_{PN} is very small and therefore the noise term converted from the laser RIN is negligible. Fig. 6.6 (a) shows an example of phase noise PSD prediction at an input power of 1.4 mW. The ratio r_{PN} is 0.051, corresponding to a decrease of laser RIN PSD of ~25.8 dB. Fig. 6.6 (b) shows the predicted and measured phase noise PSD values at 1 kHz and 10 kHz offset frequencies under different input powers. It can be seen that the predicted and measured values match well.

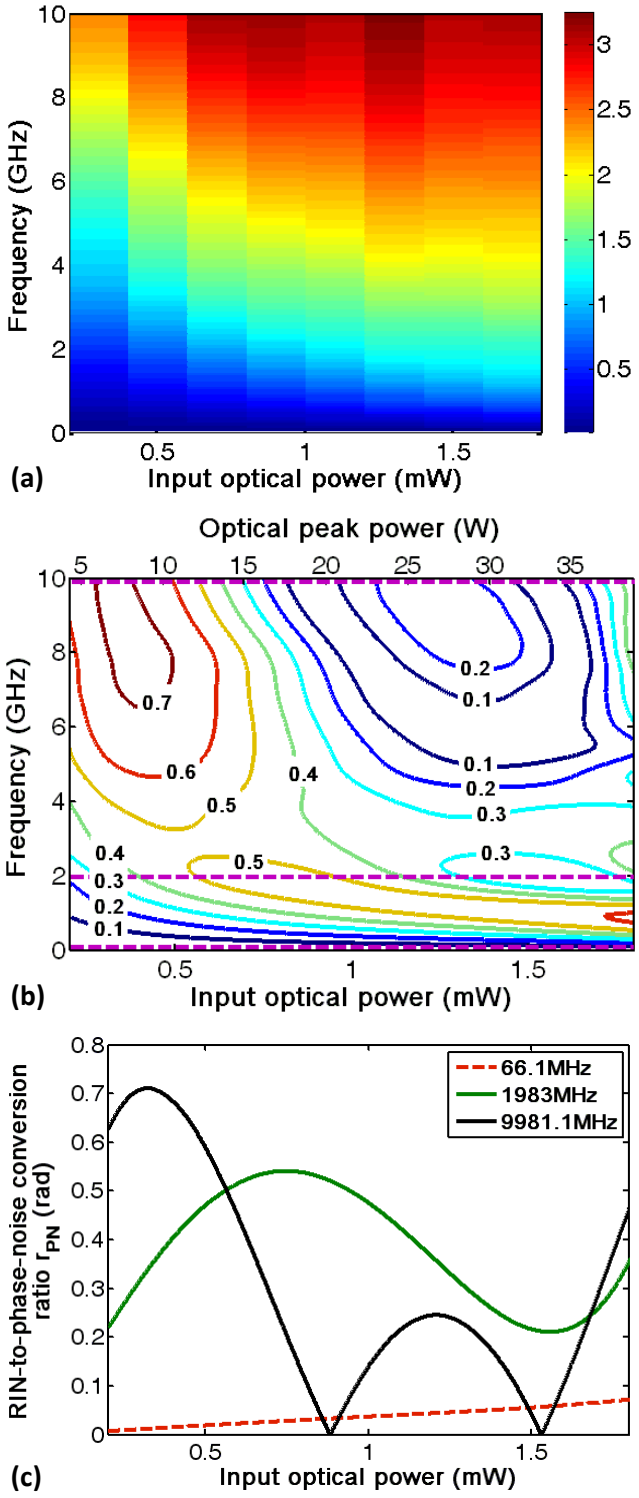

Fig. 6.5 (a) Phase values in radians as a function of frequency and average input optical power levels (b) RIN-to-phase-noise conversion ratio r_{PN} in radians after the fourth-order polynomial fit of the phases in (a). Note the different optical peak powers corresponding to different input optical powers. (c) Three examples of the RIN-to-phase-noise conversion ratios corresponding to the three dashed lines in (b)

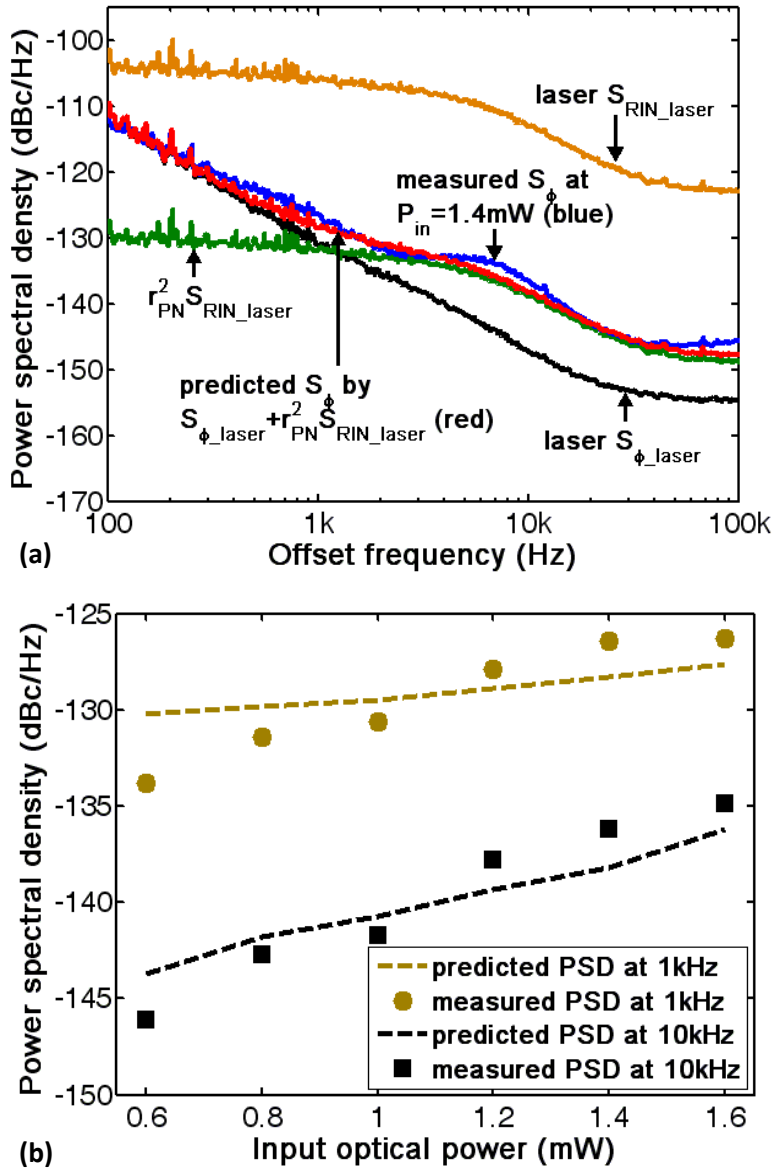

Fig. 6.6 (a) Phase noise PSD prediction at an input power of 1.4 mW. (b) Predicted and measured phase noise PSD values at 1 kHz and 10 kHz offset frequencies under different input optical power.

6.4 *Effect of pulse width and peak power of the incident optical pulses*

Previous research has shown that the impulse response of the photodetectors is also affected by the peak power (and thereby the pulse width) for a given average power of the incident optical pulses [89]. We now investigate this effect in the context of small pulse width by inserting a certain length of single mode fiber (SMF) between the VOA and the photodetector in Fig. 1. The pigtails of the VOA are 2 m SMF.

Four different SMF lengths 2 m, 4 m, 12 m and 22 m are considered and the measurements are carried out at 1.8 mW input power. These fiber lengths result in increased optical pulse widths of 0.7 ps, 1 ps, 2.1 ps, 3.6 ps, respectively, and a corresponding decrease in the incident peak power. The pulse widths are quite insensitive to the input power injected into the SMF. A decrease of input power from 1.8mW to 0.2mW leads to a less than 10% increase of pulse widths. Fig. 6.7 gives an example of measured pulse profiles at two input power levels of 0.4 mW and 1.4 mW for different SMF lengths (VOA is used to compensate the different values of the insertion loss of the SMF and fiber connectors). It can be seen that the optical pulses with a wider pulse width (and lower peak power) typically generate electrical pulses with lower amplitudes and narrower pulse widths; this in turn leads to a change in the noise conversion ratios. Fig. 6.8 shows the calculated noise conversion ratios r_{PWJ}, r_{RAN_P} and r_{RAN_R} with a 4 m SMF which confirms the validity of Eq.(6.26). Fig. 6.9 summarizes the ratios r_{PWJ} and r_{RAN_R} for all four different lengths of SMF. Compared with the ratios measured with 2 m SMF, the change is less than 0.15 in both r_{PWJ} and r_{RAN_R}, indicating that the effect of changing incident optical pulse width and peak power is very limited on r_{PWJ} , r_{RAN_P} and r_{RAN_R}.

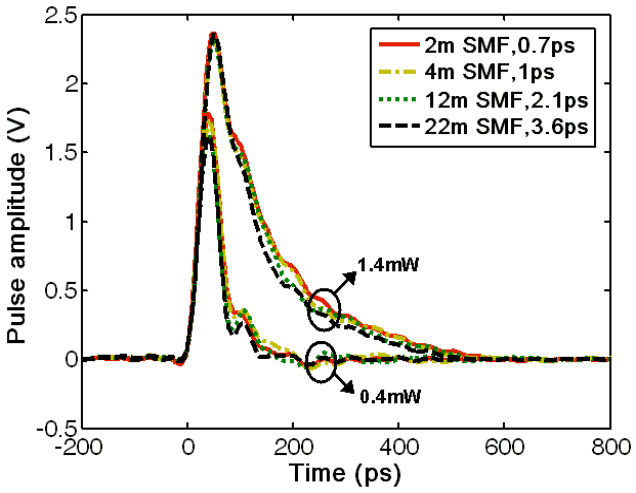

Fig. 6.7 Electrical pulse profiles measured at two input optical power levels of 0.4 mW and 1.4 mW for different SMF lengths and pulse widths.

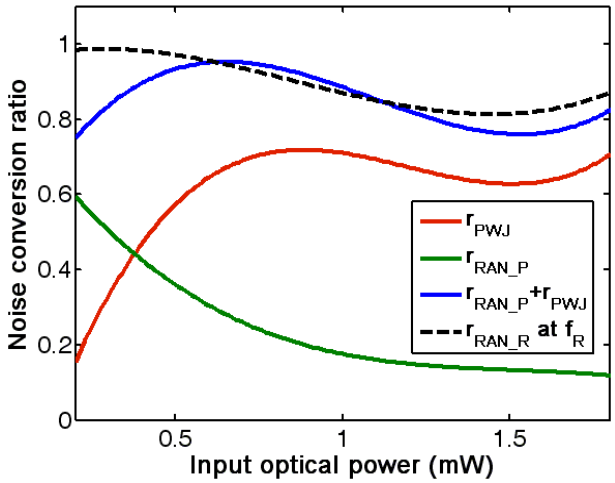

Fig. 6.8 Noise conversion ratios with 4 m SMF (1 ps pulse width)

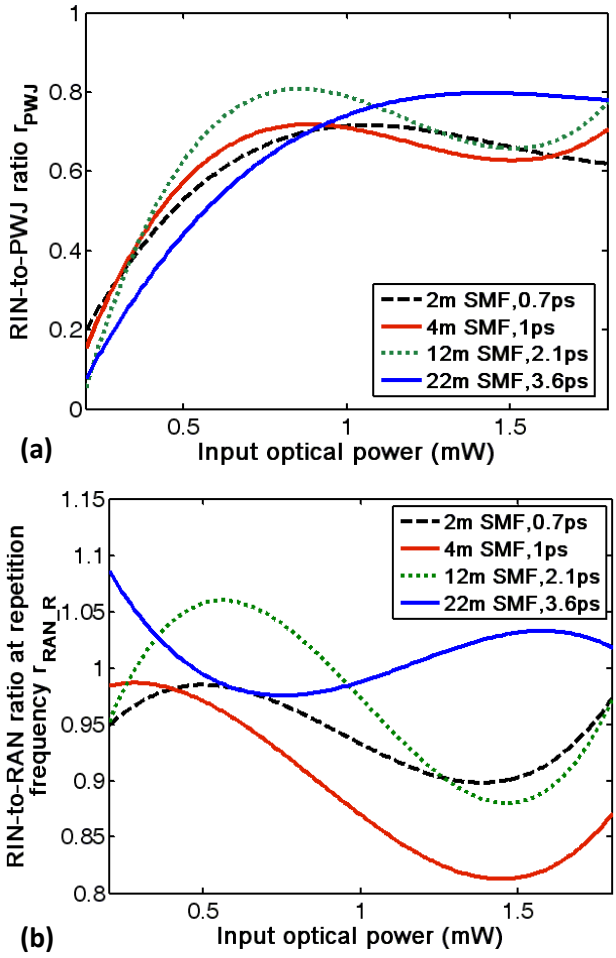

Fig. 6.9 (a) RIN-to-PWJ conversion ratio r_{PWJ} (b) RIN-to-RAN (RAN at f_R) conversion ratio r_{RAN_R} for different SMF lengths and pulse widths.

The RIN-to-phase-noise conversion ratio values measured for different SMF lengths are also considered and shown in Fig. 6.10. It can be seen that a change in the incident optical pulse width (and peak power) leads to a change of r_{PN} especially when the frequency is higher than 2 GHz. This suggests that the optical-pulse-width-dependent (or peak-power-dependent) impulse response of the photodetector is mainly due to the response at high frequency components. Also, it seems to be more convenient to use incident optical pulse width rather than the previously used optical peak power to describe this effect because the pulse width is quite insensitive to the input power injected into the SMF before photodetector due to the weak fiber nonlinear effect whereas peak power is directly affected both by the input power and pulse width. This means the pulse width and input power can be treated as two independent and "orthogonal" variables which can be controlled individually for actual microwave signal synthesis application. For the 10 GHz photodetector, it is found that the ratios r_{PN} in Fig. 6.10 (b) and (c) are nearly identical which indicates that an increase in optical pulse width beyond 2.1 ps (corresponding to 12 m SMF) has very limited effect on the RIN-to-phase-noise conversion ratios for a given frequency and input optical power.

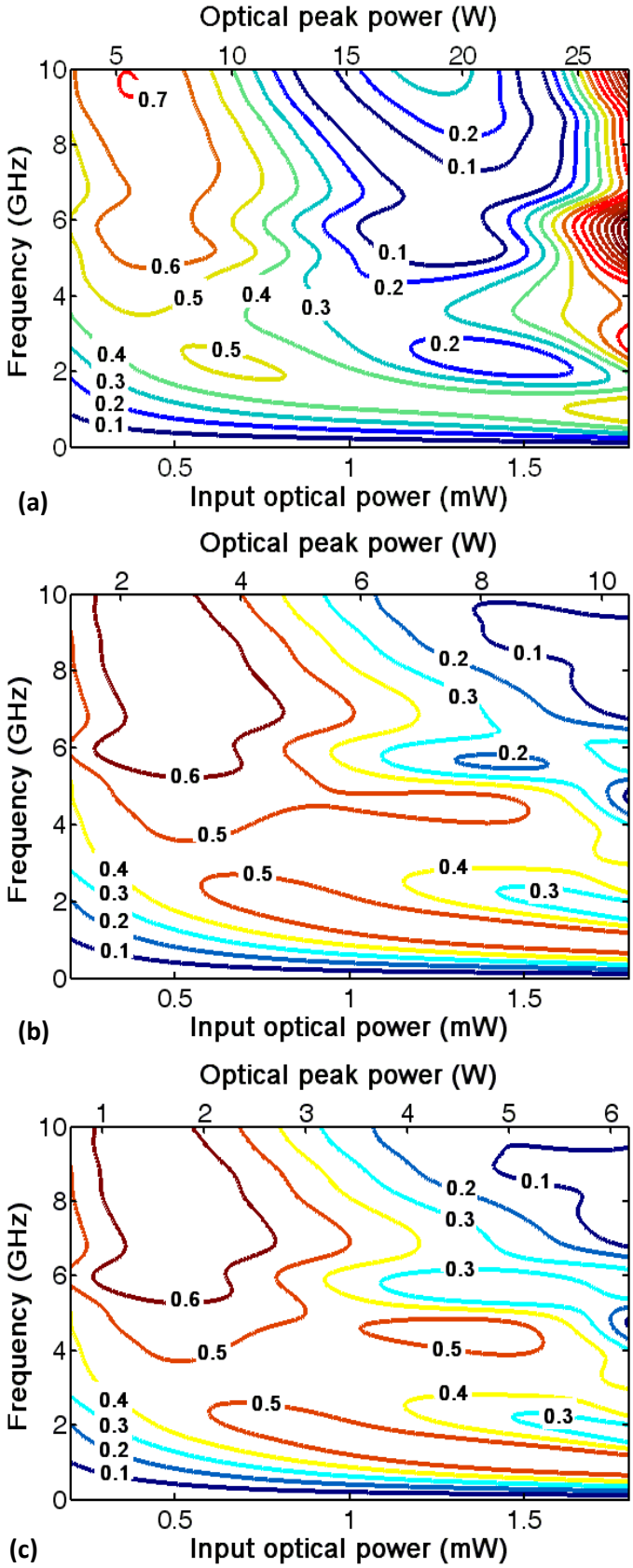

Fig. 6.10 RIN-to-phase-noise conversion ratios r_{PN} (in radians) for different SMF lengths (a) 4 m (1 ps pulse width), (b) 12 m (2.1 ps pulse width) and (c) 22 m (3.6 ps pulse width) for the 10 GHz photodetector. Note the different optical peak power levels corresponding to average input optical power levels for each SMF length.

For low-noise microwave signal synthesis applications, a proper operating point of the photodetectors should be chosen to achieve low RIN-to-phase-noise conversion. For example, if we use the 10 GHz photodetector to generate a signal at 10 GHz and define an acceptable range of r_{PN} as 0~0.1 (corresponding to a maximum RIN-to-phase-noise conversion ratio of -20 dB in PSD), the corresponding acceptable input power ranges according to Fig. 6.5 (b) and Fig. 6.10 are 0.82-0.96 mW & 1.45-1.60 mW for 2 m SMF (0.7 ps optical pulse width) and 0.84-0.96 mW & 1.48-1.56 mW for 4 m SMF lengths (1 ps optical pulse width) and none for the remaining two SMF lengths. It is worth mentioning that a wider optical pulse width (or a lower peak power) does not necessarily lead to a lower r_{PN} and a wider acceptable input power range. One can see that for 10 GHz frequency, acceptable input power ranges are wider for narrower optical pulse widths; on the other hand the input power range can also be wider for wider optical pulse widths at other frequencies, e.g., 9 GHz.

6.5 *Effect of the saturation power of photodetectors*

In many applications of low-noise microwave signal synthesis, a wideband photodetector is used. This may implicitly suggest that a wideband photodetector should have a low RIN-to-phase-noise conversion. However, our comparison of two photodetectors with 10 GHz and 2 GHz bandwidth respectively, shows that this is not necessarily true and the saturation power of the photodetectors may play an even more important role to achieve low RIN-to-phase-noise conversion. We show in Fig. 6.11 the measured impulse response of a 2 GHz photodetector (Thorlabs DET01CFC) for various input optical powers. The experimental conditions are exactly the same as those for the 10 GHz photodetector covered in section 0 RIN-to-

phase-noise conversion ratio r_{PN} is shown in Fig. 6.12 (a). For comparison, we re-plot the r_{PN} contours of the 10 GHz photodetector for frequencies below 2 GHz in Fig. 6.12 (b).

It is seen that for the 2 GHz photodetector when the input power is below ~0.5 mW, only the amplitude of the output pulses increases linearly with increasing optical input power and the pulse width and pulse profile are nearly unchanged. This means that the pulse "gravity center" is nearly unchanged and thus the excess phase noise converted from the optical intensity noise is low. When the input power is higher than 0.5 mW, the pulse distortion of the 2 GHz photodetector becomes significant, leading to a quick increase of r_{PN}. On the contrary, for the 10 GHz photodetector, both the amplitude and pulse width of the output pulses increase with the input power for input powers starting as low as ~0.2 mW (see Fig. 6.3 (a)) and thus the pulse "gravity center" is changed accordingly, leading to a higher phase noise conversion ratio r_{PN}.

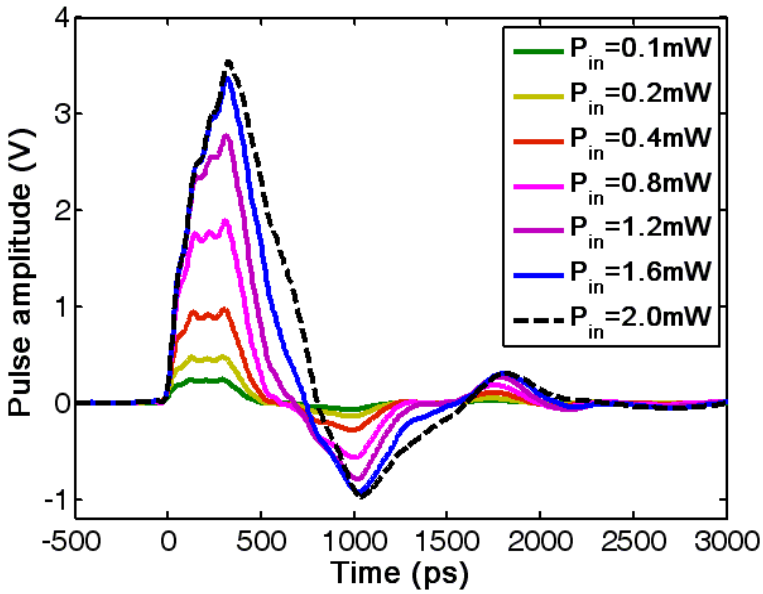

Fig. 6.11 Electrical pulse profiles for different input optical powers incident on a 2 GHz photodetector.

We can define an impulse-response saturation power (IRSP) below which increasing input optical power leads to a linear increase of electrical pulse amplitude with pulse width and pulse profile nearly unchanged. The IRSP is ~0.5 mW for the 2 GHz photodetector and ~0.2 mW for the 10 GHz photodetector. Our experimental observation suggests that the RIN-to-phase-noise conversion is low when the input power is below the IRSP although r_{PN} may not be necessarily less than 0.1 for some frequencies (see Fig. 6.12). The photodetector with a higher IRSP is preferred to allow a wider acceptable input power range (assuming that it has a sufficient bandwidth for the application) while maintaining a low excess phase noise $r_{PN} < 0.1$. This is also supported by the experimental observations on the photodetectors with similar bandwidth but different IRSP reported in [16].

Another observation is that, at a given input power, a photodetector with narrower bandwidth concentrates the power to a few low frequency components whereas a photodetector with wider bandwidth distributes the power to a wide range of frequency components. Therefore, the lower frequency components of a photodetector with narrow bandwidth have higher power than those of a photodetector with wide bandwidth. This suggests that a photodetector with just the necessary bandwidth is meaningful for real applications of microwave signal synthesis because higher output power can suppress shot and thermal noise, e.g., to generate a 1 GHz signal a photodetector with a bandwidth of 2 GHz can provide higher power at 1 GHz than a photodetector with a bandwidth of 10 GHz.

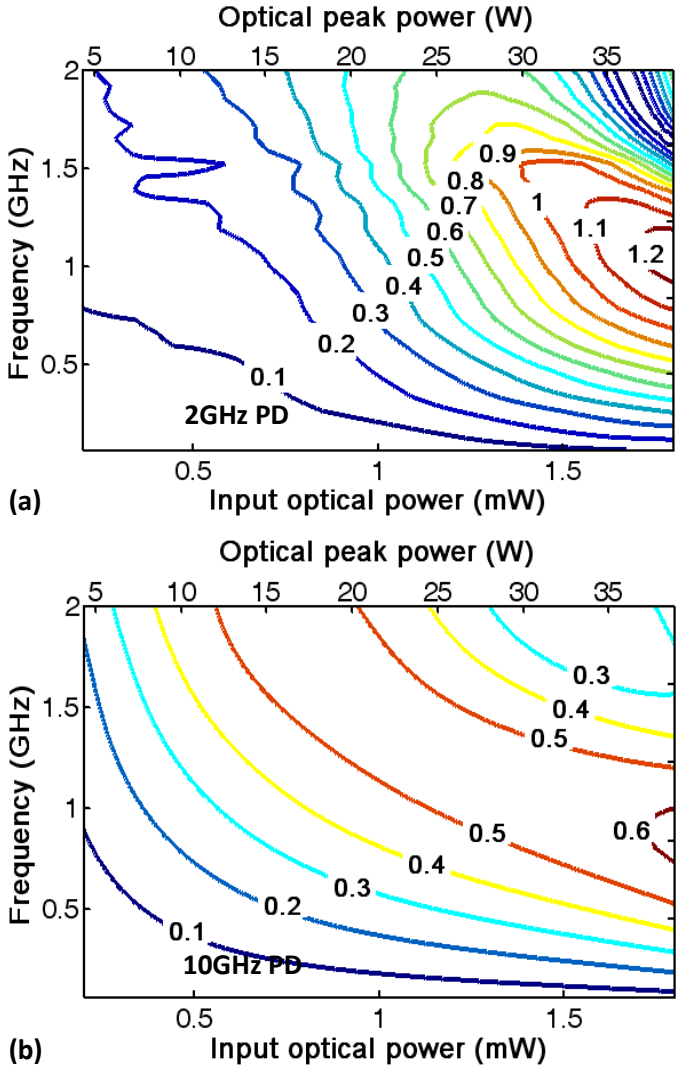

Fig. 6.12 RIN-to-phase-noise conversion ratios r_{PN} (in radians) of (a) 2 GHz photodetector and (b) 10 GHz photodetector.

Ref.[16] has discussed the effect of different photodetector design. Three designs were investigated. The first design was a conventional design for direct SMF input. The second design utilized a GRIN lens to couple the incident light to the detector. The third design applied a much thinner InP cap and a larger detection area to improve the power handling. Good power handling reduced the pulse distortion after photodetection and thus led to a better RIN-to-phase-noise conversion. The measurement results showed that the third photodetector exhibited much better RIN-to-phase-noise conversion and much regular output pulse shape

than the other two. We do not have the facility to design our own photodetector and therefore cannot compare the other noise conversion performance such as RIN-to-PWJ and RIN-to-RAN for different photodetector design.

6.6 *Summary*

In summary, we have presented a method for the detailed characterization of the excess noise conversion from optical RIN to electrical pulse width jitter, relative amplitude noise and phase noise in the photodetectors when detecting the optical pulse train from mode-locked lasers. It has been shown that the RIN-to-PWJ, RIN-to-RAN (RAN of pulse amplitude) and RIN-to-phase- noise conversion ratios can be obtained by analyzing the electrical pulse profiles measured by a high-speed oscilloscope for different input optical powers. The RIN-to-RAN (RAN at f_R) has been obtained by measuring the power at the repetition frequency by an RF spectrum analyzer for different input optical powers. Theoretical analysis has been presented to describe the relations among these noise conversion ratios and to predict the measured electrical RAN and phase noise power spectral densities. Also, optical pulses with the same average power but different pulse width and peak power are found to affect the noise conversion ratios of the photodetectors due to their optical-pulse-width-dependent impulse response, especially for the RIN-to-phase-noise conversion ratio at high frequencies. This method can be applied to any kind of photodetectors for noise characterization; however the exact noise conversion ratios for a certain photodetector are dependent on its design. A photodetector with higher impulse-response saturation power is found to allow a larger input optical power range in which the RIN-to-phase-noise conversion ratio is less than 0.1. These results provide many useful guidelines for achieving low-noise

photodetection in microwave signal synthesis application: a photodetector with higher impulse-response saturation power allows a wider range of input power levels while maintaining the excess phase noise to a low value. In addition, a proper operating point of the photodetector with respect to the input optical power and the optical pulse width needs to be chosen to obtain a low value of excess phase noise.

7 Conclusions and future work

7.1 *Conclusions*

In this thesis, we have discussed three main parts of our work. They are timing jitter reduction for passively mode-locked fiber lasers, linear and nonlinear noise conversion from the pump to the mode-locked lasers and excess phase noise conversion induced by the photodetection process.

For the timing jitter reduction for passively mode-locked lasers, we first review the theory of quantum limited noise for mode-locked lasers. Based on this theory, the optimization of the cavity loss is found to suppress the indirect noise source coupled from the frequency jitter to the timing jitter. One should also notice that this optimization of the cavity loss is only valid when the cavity net dispersion is not very small. For the mode-locked laser in our experiment, the cavity net dispersion is -0.1 ps^2 and timing jitter reduction of 24% is demonstrated. Then we analyze the drift of the repetition frequency of the mode-locked laser due to the temperature fluctuation, vibration and etc. A feedback control loop based on Proportional-Integral-Derivative control and piezoelectric transducer is set up. The phase noise at low offset frequency is found to be suppressed when the feedback is turned on and an external oscillator is applied as reference. Lastly, we investigate the effect of external incoherent addition structures. Two structures called Mach-Zehnder (MZ) and ring are studied. It is found that both MZ and ring structures can suppress the phase noise at specific spectrum positions (dependent on the design of the MZ or ring structures) for pulse trains with a background noise level above -130 dBc/Hz. This result may not be able to reduce the timing jitter of the pulse trains

directly from the mode-locked fiber lasers but can be applied for the amplified pulse trains from the Erbium-doped fiber amplifier.

For the linear and nonlinear noise conversion from the pump to the mode-locked lasers, we first experimentally characterize the linear noise conversion from the pump relative intensity noise (RIN) to the RIN and phase noise of mode-locked fiber lasers at 1.55 μm. Two mode locking mechanisms, nonlinear polarization rotation (NPR) and semiconductor saturable absorber mirror (SESAM), are compared. Pump RIN is found to be the dominant noise source for both lasers (NPR laser and SESAM laser) and thus their RIN and phase noise can be predicted with the measured noise conversion ratios and pump RIN. It is also found that the SESAM laser shows an higher phase noise than the NPR laser due to additional intracavity RIN to phase noise conversion caused by the slow saturable absorber effect of the SESAM. Then we study the nonlinear RIN conversion from the pump to the mode-locked lasers. The nonlinear RIN conversion is found to generate additional noise power at various harmonics kf_M with respect to the fundamental pump modulation frequency f_M. An exponential decay model is proposed to describe the behavior of the nonlinear RIN conversion. Physical explanation of the nonlinear noise conversion effect from the view of gain modulation is proposed and verifies the validity of exponential decay model.

For the excess phase noise conversion induced by the photodetection process, we first present a method based on the power dependent impulse response of the photodetectors in order to characterize the excess noise conversion from optical RIN to electrical pulse width jitter, relative amplitude noise and phase noise in the photodetectors when detecting the optical pulse train from mode-locked lasers. Theoretical analysis has been presented to describe the relations among these noise

conversion ratios and to predict the measured electrical relative amplitude noise (RAN) and phase noise power spectral densities. Also, optical pulses with the same average power but different pulse width and peak power are found to affect the noise conversion ratios of the photodetectors due to their optical-pulse-width-dependent impulse response, especially for the RIN-to-phase-noise conversion ratio at high frequencies. Moreover, a photodetector with higher impulse-response saturation power is found to allow a larger input optical power range in which the RIN-to-phase-noise conversion ratio is less than 0.1. These results provide many useful guidelines for achieving low-noise photodetection in microwave signal synthesis application: a photodetector with higher impulse-response saturation power allows a wider range of input power levels while maintaining the excess phase noise to a low value. In addition, a proper operating point of the photodetector with respect to the input optical power and the optical pulse width needs to be chosen to obtain a low excess phase noise.

7.2 *Future work*

The studies described in this thesis suggest many interesting directions to pursue for the future work. We briefly discuss some of these directions.

7.2.1 Mode-locked fiber laser with Erbium-doped PCF

Compared with the Ti : Sapphire mode-locked lasers, a limitation existing in Er-doped mode-locked fiber lasers is the difficulty of complete dispersion compensation over a wide spectral range which leads to a limited output bandwidth. Due to the limited design parameters, it is nearly impossible to realize complete dispersion compensation over a wide spectral range with standard fiber structure, i.e.,

single core and cladding structure. However PCF allows many more design freedoms and therefore has the possibility to achieve a desired dispersion curve and complete dispersion compensation and thus a wide laser output spectrum. This means it is possible to obtain a very narrow pulse width directly from the oscillator stage. Moreover, doping Erbium ions to PCF can realize a short cavity consisting of only PCF which avoids the problem of high splicing loss between PCF and standard fiber and thus leads to a high repetition frequency. The difficulty of this work will lie in the design of PCF to achieve a wide-band low-dispersion region. Also, doping Erbium ions to PCF structure to a high concentration may also be a big challenge.

Also, using FBG to compensate cavity dispersion is not a good choice. To support a relatively wideband reflection in the laser cavity, FBG must be chirped. However chirped FBG also introduces a large amount of dispersion (can easily equivalent to a few hundred meters of SMF). This large dispersion is dominant if the cavity length is short. So finally the large dispersion introduced by chirped FBG in the cavity results in a narrower output spectrum and wider pulse duration, which is not desired.

7.2.2 Low-noise pulse train amplification

The output power of a low-noise mode-locked fiber laser at 1.5 μm is usually limited to a maximum of ~10 mW. For many applications such as frequency metrology and photonics ADC, a higher power is often required. However, there is not much work on the low-noise amplification of the pulse train from a low-noise mode-locked laser. As we have shown in the chapter 3, a conventional EDFA can introduce significant phase noise and timing jitter. Therefore it is meaningful to develop a technology of low-noise pulse train amplification. A possible solution

may be the gated amplification. For gated amplification, the optical amplifier is only turned on when the pulse comes and turned off during the rest of the time. Although the amplification process is still noisy and not quantum limited due to the inevitable spontaneous emission in the EDFA, the ASE between two adjacent pulses can be significantly eliminated since the EDFA is off. Averagely, the total noise power is lower down. The most challenging part will be the design of an electrical gating system which can work at a very high gating speed, comparable to the pulse width from the mode-locked lasers. The recovery time of the gain media (for EDF, it is ~10 ms) needs to be taken into the consideration as well.

References

[1] C. H. TOWNES, "Production of coherent radiation by atoms and molecule," *Nobel Lecture,* 1964.

[2] T. H. Maiman, "Stimulated optical radiation in ruby," *Nature,* vol. 187, pp. 493-494, 1960.

[3] G. P. Agrawal. (2001). *Nonlinear Fiber Optics*.*4th Ed.*, pp. 1

[4] G. P. Agrawal. (2001). *Applications of Nonlinear Fiber Optics*.*2nd Ed.*, pp. 179

[5] R. Holzwarth, M. Zimmermann, T. Udem, and T. W. Hansch, "Optical clockworks and the measurement of laser frequencies with a mode-locked frequency comb," *Quantum Electronics, IEEE Journal of,* vol. 37, pp. 1493-1501, 2001.

[6] J. J. McFerran, W. C. Swann, B. R. Washburn, and N. R. Newbury, "Elimination of pump-induced frequency jitter on fiber-laser frequency combs," *Opt. Lett.,* vol. 31, pp. 1997-1999, 2006.

[7] J. L. Hall, Y. Jun, S. A. Diddams, M. Long-Sheng, S. T. Cundiff, and D. J. Jones, "Ultrasensitive spectroscopy, the ultrastable lasers, the ultrafast lasers, and the seriously nonlinear fiber: a new alliance for physics and metrology," *Quantum Electronics, IEEE Journal of,* vol. 37, pp. 1482-1492, 2001.

[8] G. C. Valley, "Photonic analog-to-digital converters," *Opt. Express,* vol. 15, pp. 1955-1982, 2007.

[9] J. Kim, J. A. Cox, J. Chen, and F. X. Kartner, "Drift-free femtosecond timing synchronization of remote optical and microwave sources," *Nat Photon,* vol. 2, pp. 733-736, 2008.

[10] S. M. Foreman, K. W. Holman, D. D. Hudson, D. J. Jones, and J. Ye, "Remote transfer of ultrastable frequency references via fiber networks," *Review of Scientific Instruments,* vol. 78, pp. 021101-25, 2007.

[11] J. Millo, R. Boudot, M. Lours, P. Y. Bourgeois, A. N. Luiten, Y. L. Coq, Y. Kersalé, and G. Santarelli, "Ultra-low-noise microwave extraction from fiber-based optical frequency comb," *Opt. Lett.*, vol. 34, pp. 3707-3709, 2009.

[12] J. Kim and F. X. Kärtner, "Microwave signal extraction from femtosecond mode-locked lasers with attosecond relative timing drift," *Opt. Lett.*, vol. 35, pp. 2022-2024, 2010.

[13] T. M. Fortier, M. S. Kirchner, F. Quinlan, J. Taylor, J. C. Bergquist, T. Rosenband, N. Lemke, A. Ludlow, Y. Jiang, C. W. Oates, and S. A. Diddams, "Generation of ultrastable microwaves via optical frequency division," *Nat Photon,* vol. 5, pp. 425-429, 2011.

[14] H. Jiang, J. Taylor, F. Quinlan, T. Fortier, and S. A. Diddams, "Noise Floor Reduction of an Er:Fiber Laser-Based Photonic Microwave Generator," *Photonics Journal, IEEE,* vol. 3, pp. 1004-1012, 2011.

[15] F. Quinlan, T. M. Fortier, M. S. Kirchner, J. A. Taylor, M. J. Thorpe, N. Lemke, A. D. Ludlow, Y. Jiang, and S. A. Diddams, "Ultralow phase noise microwave generation with an Er:fiber-based optical frequency divider," *Opt. Lett.*, vol. 36, pp. 3260-3262, 2011.

[16] J. Taylor, S. Datta, A. Hati, C. Nelson, F. Quinlan, A. Joshi, and S. Diddams, "Characterization of Power-to-Phase Conversion in High-Speed P-I-N Photodiodes," *Photonics Journal, IEEE,* vol. 3, pp. 140-151, 2011.

[17] K. Wu, P. Shum, S. Aditya, C. Ouyang, J. Wong, H. Lam, and K. Lee, "Characterization of the Excess Noise Conversion from Optical Relative Intensity Noise in the Photodetection of Mode-locked Lasers for Microwave Signal Synthesis," *Lightwave Technology, Journal of,* vol. 29, pp. 3622-3631, 2011.

[18] K. Yvind, D. Larsson, J. Mork, J. M. Hvam, M. Thompson, R. Penty, and I. White, "Low-noise monolithic mode-locked semiconductor lasers through low-dimensional structures," San Jose, CA, USA, 2008, pp. 69090A-9.

[19] H. Tsuchida, "Pulse-timing noise reduction of a mode-locked laser diode by incoherent addition," *Selected Topics in Quantum Electronics, IEEE Journal of,* vol. 9, pp. 1081-1092, 2003.

[20] U. Keller, K. J. Weingarten, F. X. Kartner, D. Kopf, B. Braun, I. D. Jung, R. Fluck, C. Honninger, N. Matuschek, and J. A. derAu, "Semiconductor saturable absorber mirrors (SESAM's) for femtosecond to nanosecond pulse generation in solid-state lasers," *Selected Topics in Quantum Electronics, IEEE Journal of,* vol. 2, pp. 435-453, Sep 1996.

[21] J. A. Alvarez-Chavez, H. L. Offerhaus, J. Nilsson, P. W. Turner, W. A. Clarkson, and D. J. Richardson, "High-energy, high-power ytterbium-doped Q-switched fiber laser," *Opt. Lett.,* vol. 25, pp. 37-39, 2000.

[22] C. C. Renaud, R. J. Selvas-Aguilar, J. Nilsson, P. W. Turner, and A. B. Grudinin, "Compact high-energy Q-switched cladding-pumped fiber laser with a tuning range over 40 nm," *Photonics Technology Letters, IEEE,* vol. 11, pp. 976-978, 1999.

[23] S. Gee, F. Quinlan, S. Ozharar, P. J. Delfyett, J. J. Plant, and P. W. Juodawlkis, "Ultralow-noise mode-locked optical pulse trains from an external cavity laser based on a slab coupled optical waveguide amplifier (SCOWA)," *Opt. Lett.,* vol. 30, pp. 2742-2744, 2005.

[24] K. Wu, J. H. Wong, P. Shum, D. R. C. S. Lim, V. K. H. Wong, K. E. K. Lee, J. Chen, and E. D. Obraztsova, "Timing-jitter reduction of passively mode-locked fiber laser with a carbon nanotube saturable absorber by optimization of cavity loss," *Opt. Lett.,* vol. 35, pp. 1085-1087, 2010.

[25] T. Hasan, Z. P. Sun, F. Q. Wang, F. Bonaccorso, P. H. Tan, A. G. Rozhin, and A. C. Ferrari, "Nanotube-Polymer Composites for Ultrafast Photonics," *Advanced Materials,* vol. 21, pp. 3874-3899, Oct 2009.

[26] F. Bonaccorso, Z. Sun, T. Hasan, and A. C. Ferrari, "Graphene photonics and optoelectronics," *Nat Photon,* vol. 4, pp. 611-622, 2010.

[27] H. Zhang, Q. Bao, D. Tang, L. Zhao, and K. Loh, "Large energy soliton erbium-doped fiber laser with a graphene-polymer composite mode locker," *Applied Physics Letters,* vol. 95, p. 141103, 2009.

[28] J. Zhou, G. Taft, C.-P. Huang, M. M. Murnane, H. C. Kapteyn, and I. P. Christov, "Pulse evolution in a broad-bandwidth Ti:sapphire laser," *Opt. Lett.,* vol. 19, pp. 1149-1151, 1994.

[29] NobelPrize. http://nobelprize.org/nobel_prizes/physics/laureates/2005/ [Online]. Available: Freq. Metrology

[30] AnalogDevicesInc. http://www.analog.com/en/analog-to-digital-converters/ad-converters/products/index.html [Online].

[31] H. A. Haus and A. Mecozzi, "Noise of mode-locked lasers," *Quantum Electronics, IEEE Journal of,* vol. 29, pp. 983-996, 1993.

[32] S. Namiki and H. A. Haus, "Noise of the stretched pulse fiber laser. I. Theory," *Quantum Electronics, IEEE Journal of,* vol. 33, pp. 649-659, 1997.

[33] L. A. Jiang, M. E. Grein, E. P. Ippen, C. McNeilage, J. Searls, and H. Yokoyama, "Quantum-limited noise performance of a mode-locked laser diode," *Opt. Lett.*, vol. 27, pp. 49-51, 2002.
[34] R. Paschotta, "Noise of mode-locked lasers (Part I): numerical model," *Appl. Phys. B*, vol. 79, pp. 153-162, 2004.
[35] R. Paschotta, "Timing jitter and phase noise of mode-locked fiber lasers," *Opt. Express*, vol. 18, pp. 5041-5054, 2010.
[36] R. Paschotta, "Noise of mode-locked lasers (Part II): timing jitter and other fluctuations," *Appl. Phys. B*, vol. 79, pp. 163-173, 2004.
[37] L. P. Chen, Y. Wang, and J. M. Liu, "Spectral measurement of the noise in continuous-wave mode-locked laser pulses," *Quantum Electronics, IEEE Journal of*, vol. 32, pp. 1817-1825, 1996.
[38] D. Eliyahu, R. A. Salvatore, and A. Yariv, "Noise characterization of a pulse train generated by actively mode-locked lasers," *J. Opt. Soc. Am. B*, vol. 13, pp. 1619-1626, 1996.
[39] D. Eliyahu, R. A. Salvatore, and A. Yariv, "Effect of noise on the power spectrum of passively mode-locked lasers," *J. Opt. Soc. Am. B*, vol. 14, pp. 167-174, 1997.
[40] I. G. Fuss, "An interpretation of the spectral measurement of optical pulse train noise," *Quantum Electronics, IEEE Journal of*, vol. 30, pp. 2707-2710, 1994.
[41] I. G. Fuss and K. J. Grant, "An all frequency model of optical pulse train noise spectra," *Optical and Quantum Electronics*, vol. 31, pp. 431-449, 1999.
[42] K. J. Granta, H.-F. Liub, and R. Janb, "Spectral technique for measuring the pulse-width jitter of a gain-switched laser," *Optics Communications*, vol. 213, pp. 183-186, 2002.
[43] L. A. Jiang, S. T. Wong, M. E. Grein, E. P. Ippen, and H. A. Haus, "Measuring timing jitter with optical cross correlations," *Quantum Electronics, IEEE Journal of*, vol. 38, pp. 1047-1052, 2002.
[44] J. Kim, J. Chen, J. Cox, and F. X. Kärtner, "Attosecond-resolution timing jitter characterization of free-running mode-locked lasers," *Opt. Lett.*, vol. 32, pp. 3519-3521, 2007.
[45] D. v. d. Linde, "Characterization of the Noise in Continuously Operating Mode-Locked Lasers," *Appl. Phys. B*, vol. 39, pp. 201-217, 1986.
[46] R. P. Scott, C. Langrock, and B. H. Kolner, "High-dynamic-range laser amplitude and phase noise measurement techniques," *Selected Topics in Quantum Electronics, IEEE Journal of*, vol. 7, pp. 641-655, 2001.
[47] D. E. Spence, W. E. Sleat, J. M. Evans, W. Sibbett, and J. D. Kafka, "Time synchronisation measurements between two self-modelocked Ti:sapphire lasers," *Optics Communications*, vol. 101, pp. 286-296, 1993.
[48] C. X. Yu, S. Namiki, and H. A. Haus, "Noise of the stretched pulse fiber laser. II. Experiments," *Quantum Electronics, IEEE Journal of*, vol. 33, pp. 660-668, 1997.
[49] J. Chen, J. W. Sickler, P. Fendel, E. P. Ippen, F. X. Kärtner, T. Wilken, R. Holzwarth, and T. W. Hänsch, "Generation of low-timing-jitter femtosecond pulse trains with 2 GHz repetition rate via external repetition rate multiplication," *Opt. Lett.*, vol. 33, pp. 959-961, 2008.
[50] S. Gee, S. Ozharar, F. Quinlan, J. J. Plant, P. W. Juodawlkis, and P. J. Delfyett, "Self-Stabilization of an Actively Mode-Locked Semiconductor-

Based Fiber-Ring Laser for Ultralow Jitter," *Photonics Technology Letters, IEEE,* vol. 19, pp. 498-500, 2007.

[51] H. Tsuchida, "Correlation between amplitude and phase noise in a mode-locked Cr : LiSAF laser," *Optics Letters,* vol. 23, pp. 1686-1688, Nov 1998.

[52] C. R. Menyuk, J. K. Wahlstrand, J. Willits, R. P. Smith, T. R. Schibli, and S. T. Cundiff, "Pulse dynamics in mode-locked lasers: relaxation oscillations and frequency pulling," *Opt. Express,* vol. 15, pp. 6677-6689, 2007.

[53] Y. Song, K. Jung, and J. Kim, "Impact of pulse dynamics on timing jitter in mode-locked fiber lasers," *Opt. Lett.,* vol. 36, pp. 1761-1763, 2011.

[54] AgilentTechnologies. (2009, *E5052B Signal Source Analyzer*. Available: http://www.home.agilent.com/agilent/product.jspx?cc=US&lc=eng&ckey=1081579&nid=-35185.631410.00&id=1081579&pselect=SR.General

[55] Rohde&Schwarz. (2009, *FSUP26 Signal Source Analyzer*. Available: http://www2.rohde-schwarz.com/en/products/test_and_measurement/spectrum_analysis/FSUP-%7C-Key_Facts-%7C-4-%7C-4865.html

[56] J. A. Cox, A. H. Nejadmalayeri, J. Kim, and F. X. Kärtner, "Complete characterization of quantum-limited timing jitter in passively mode-locked fiber lasers," *Opt. Lett.,* vol. 35, pp. 3522-3524, 2010.

[57] O. Prochnow, R. Paschotta, E. Benkler, U. Morgner, J. Neumann, D. Wandt, and D. Kracht, "Quantum-limited noise performance of a femtosecond all-fiber ytterbium laser," *Opt. Express,* vol. 17, pp. 15525-15533, 2009.

[58] S. Yamashita, T. Yoshida, S. Y. Set, P. Polynkin, and N. Peyghambarian, "Passively mode-locked short-cavity 10GHz Er:Yb-codoped phosphate-fiber laser using carbon nanotubes," San Jose, CA, USA, 2007, pp. 64531Y-9.

[59] A. V. Tausenev, E. D. Obraztsova, A. S. Lobach, A. I. Chernov, V. I. Konov, P. G. Kryukov, A. V. Konyashchenko, and E. M. Dianov, "177 fs erbium-doped fiber laser mode locked with a cellulose polymer film containing single-wall carbon nanotubes," *Appl. Phys. Lett.,* vol. 92, p. 171113, 2008.

[60] S. Namiki, E. P. Ippen, H. A. Haus, and K. Tamura, "Relaxation oscillation behavior in polarization additive pulse mode-locked fiber ring lasers," *Appl. Phys. Lett.,* vol. 69, pp. 3969-3971, 1996.

[61] H. Byun, D. Pudo, J. Chen, E. P. Ippen, and F. X. Kärtner, "High-repetition-rate, 491 MHz, femtosecond fiber laser with low timing jitter," *Opt. Lett.,* vol. 33, pp. 2221-2223, 2008.

[62] L. E. Nelson, D. J. Jones, K. Tamura, H. A. Haus, and E. P. Ippen, "Ultrashort-pulse fiber ring lasers," *Applied Physics B: Lasers and Optics,* vol. 65, pp. 277-294, 1997.

[63] P. K. Bachmann, D. U. Wiechert, and T. P. M. Meeuwsen, "Thermal expansion coefficients of doped and undoped silica prepared by means of PCVD," *Journal of Materials Science,* vol. 23, pp. 2584-2588, 1988.

[64] G. B. Hocker, "Fiber-optic sensing of pressure and temperature," *Appl. Opt.,* vol. 18, pp. 1445-1448, 1979.

[65] C. Ouyang, P. Shum, H. Wang, J. Haur Wong, K. Wu, S. Fu, R. Li, E. J. R. Kelleher, A. I. Chernov, and E. D. Obraztsova, "Observation of timing jitter reduction induced by spectral filtering in a fiber laser mode locked with a carbon nanotube-based saturable absorber," *Opt. Lett.,* vol. 35, pp. 2320-2322, 2010.

[66] K. Wu, J. H. Wong, P. Shum, S. Fu, C. Ouyang, H. Wang, E. J. R. Kelleher, A. I. Chernov, E. D. Obraztsova, and J. Chen, "Nonlinear coupling of

relative intensity noise from pump to a fiber ring laser mode-locked with carbon nanotubes," *Opt. Express,* vol. 18, pp. 16663-16670, 2010.

[67] T. D. Mulder, R. P. Scott, and B. H. Kolner, "Amplitude and envelope phase noise of a modelocked laser predicted from its noise transfer function and the pump noise power spectrum," *Optics Express,* vol. 16, pp. 14186-14191, Sep 2008.

[68] R. P. Scott, T. D. Mulder, K. A. Baker, and B. H. Kolner, "Amplitude and phase noise sensitivity of modelocked Ti:sapphire lasers in terms of a complex noise transfer function," *Optics Express,* vol. 15, pp. 9090-9095, 2007.

[69] C. Ouyang, L. Chai, H. Zhao, M. Hu, Y. Song, and C. Wang, "Position Effect of Spectral Filter on Properties of Highly Chirped Pulses in an All-Normal-Dispersion Fiber Laser," *Quantum Electronics, IEEE Journal of,* vol. 45, pp. 1284-1288, 2009.

[70] N. Dogru and M. S. Ozyazici, "Intensity noise of mode-locked fiber grating external cavity semiconductor lasers," *Optical and Quantum Electronics,* vol. 35, pp. 169-178, Jan 2003.

[71] W. Lee, M. T. Choi, H. Izadpanah, and R. J. Delfyett, "Relative intensity noise characteristics of frequency stabilised grating-coupled modelocked semiconductor laser," *Electronics Letters,* vol. 42, pp. 1156-1157, Sep 2006.

[72] N. R. Newbury and B. R. Washburn, "Theory of the frequency comb output from a femtosecond fiber laser," *Quantum Electronics, IEEE Journal of,* vol. 41, pp. 1388-1402, Nov 2005.

[73] J. J. McFerran, W. C. Swann, B. R. Washburn, and N. R. Newbury, "Suppression of pump-induced frequency noise in fiber-laser frequency combs leading to sub-radian f (ceo) phase excursions," *Applied Physics B-Lasers and Optics,* vol. 86, pp. 219-227, Jan 2007.

[74] B. R. Washburn, W. C. Swann, and N. R. Newbury, "Response dynamics of the frequency comb output from a femtosecond fiber laser," *Optics Express,* vol. 13, pp. 10622-10633, Dec 2005.

[75] I. L. Budunoglu, C. k. Ülgüdür, B. Oktem, and F. Ö. Ilday, "Intensity noise of mode-locked fiber lasers," *Opt. Lett.,* vol. 34, pp. 2516-2518, 2009.

[76] N. R. Newbury and B. R. Washburn, "Theory of the frequency comb output from a femtosecond fiber laser," *Ieee Journal of Quantum Electronics,* vol. 41, pp. 1388-1402, Nov 2005.

[77] S. Y. Set, H. Yaguchi, Y. Tanaka, M. Jablonski, Y. Sakakibara, A. Rozhin, M. Tokumoto, H. Kataura, Y. Achiba, and K. Kikuchi, "Mode-locked fiber lasers based on a saturable absorber incorporating carbon nanotubes," in *Optical Fiber Communications Conference, 2003. OFC 2003*, 2003, pp. PD44-P1-3 vol.3.

[78] E. J. R. Kelleher, J. C. Travers, Z. Sun, A. G. Rozhin, A. C. Ferrari, S. V. Popov, and J. R. Taylor, "Nanosecond-pulse fiber lasers mode-locked with nanotubes," *Applied Physics Letters,* vol. 95, Sep 2009.

[79] S. Yamashita, Y. Inoue, K. Hsu, T. Kotake, H. Yaguchi, D. Tanaka, M. Jablonski, and S. Y. Set, "5-GHz pulsed fiber Fabry-Perot laser mode-locked using carbon nanotubes," *Photonics Technology Letters, IEEE,* vol. 17, pp. 750-752, 2005.

[80] A. I. Chernov, E. D. Obraztsova, and A. S. Lobach, "Optical properties of polymer films with embedded single-wall carbon nanotubes," *physica status solidi (b),* vol. 244, pp. 4231-4235, 2007.

[81] P. A. Obraztsov, A. A. Sirotkin, E. D. Obraztsova, Y. P. Svirko, and S. V. Garnov, "Carbon-nanotube-based saturable absorbers for near infrared solid state lasers," *Optical Review,* vol. 17, pp. 1-4, 2010.

[82] E. N. Ivanov, S. A. Diddams, and L. Hollberg, "Study of the excess noise associated with demodulation of ultra-short infrared pulses," *Ultrasonics, Ferroelectrics and Frequency Control, IEEE Transactions on,* vol. 52, pp. 1068-1074, 2005.

[83] E. N. Ivanov, J. J. McFerran, S. A. Diddams, and L. Hollberg, "Noise properties of microwave signals synthesized with femtosecond lasers," *Ultrasonics, Ferroelectrics and Frequency Control, IEEE Transactions on,* vol. 54, pp. 736-745, 2007.

[84] E. N. Ivanov, S. A. Diddams, and L. Hollberg, "Analysis of noise mechanisms limiting the frequency stability of microwave signals generated with a femtosecond laser," *Selected Topics in Quantum Electronics, IEEE Journal of,* vol. 9, pp. 1059-1065, 2003.

[85] L. Nugent-Glandorf, T. A. Johnson, Y. Kobayashi, and S. A. Diddams, "Impact of dispersion on amplitude and frequency noise in a Yb-fiber laser comb," *Opt. Lett.,* vol. 36, pp. 1578-1580, 2011.

[86] K. Wu, C. Ouyang, J. H. Wong, S. Aditya, and P. Shum, "Frequency Response of the Noise Conversion From Relative Intensity Noise to Phase Noise in the Photodetection of an Optical Pulse Train," *Photonics Technology Letters, IEEE,* vol. 23, pp. 468-470, 2011.

[87] W. Zhang, T. Li, M. Lours, S. Seidelin, G. Santarelli, and Y. L. Coq, "Amplitude to phase conversion of InGaAs pin photo-diodes for femtosecond lasers microwave signal generation," *arXiv:1104.4495v1,* 2011.

[88] O. Pottiez, O. Deparis, R. Kiyan, P. Mégret, and M. Blondel, "Measurement of pulse width and amplitude jitter noises of gigahertz optical pulse trains by time-domain demodulation," *Opt. Lett.,* vol. 26, pp. 1779-1781, 2001.

[89] P.-L. Liu, K. J. Williams, M. Y. Frankel, and R. D. Esman, "Saturation characteristics of fast photodetectors," *Microwave Theory and Techniques, IEEE Transactions on,* vol. 47, pp. 1297-1303, 1999.

Appendix A

To calculate the noise conversion from the pump RIN to the laser RIN, we start from two well known equations of the gain coefficient and pulse energy of lasers [52].

$$\frac{dg}{dt} = \frac{g_s - g}{\tau_{sp}} - \frac{g}{\tau_{sp}} \frac{wf_R}{P_S} \tag{A.1}$$

$$\frac{dw}{dt} = -\frac{w}{\tau_{ph}} + 2gwf_R \tag{A.2}$$

where g is the gain coefficient, t is the time variable, g_s is the small signal gain coefficient, τ_{sp} is the upper state lifetime of the gain medium and related to the spontaneous emission, f_R is the repetition rate, P_S is the saturation power, w is the pulse energy, τ_{ph} is the photon lifetime in the cavity.

When there is a perturbation of the pump power (pump modulation with modulation index ε and frequency ω_m), the saturation power P_S changes accordingly as

$$P_S = P_{S0}(1 + \eta\varepsilon e^{j\omega_m t}) \tag{A.3}$$

where η is a coefficient representing the efficiency of the coupling from the pump power modulation to the saturation power modulation. And we assume the solutions of new g and w are given by

$$g = g_0 + g_1 e^{j\omega_m t} \tag{A.4}$$

$$w = w_0 + w_1 e^{j\omega_m t} \tag{A.5}$$

By substituting these two solutions into Eqs.(A.1) and (A.2) and comparing the coefficient before $e^{j\omega_m t}$, we have

$$\left(j\omega_m \tau_{sp} + 1 + \frac{f_R w_0}{P_S} \right) g_1 + \frac{f_R g_0}{P_S} w_1 = \frac{f_R w_0 g_0 \eta \varepsilon}{P_S} \tag{A.6}$$

$$j\omega_m w_1 = 2 w_0 f_R g_1 \tag{A.7}$$

where we use the relation $\tau_{ph}^{-1} = 2 g_0 f_R$ derived from the equilibrium solution of Eq.(A.2). The final expressions of w_1 and g_1 are given by

$$w_1 = \frac{\omega_{sp}^2}{\omega_{sp}^2 - \omega_m^2 + j\gamma_{sp}\omega_m} \cdot \eta \varepsilon w_0 \tag{A.8}$$

$$g_1 = \frac{\omega_{sp}^2}{\omega_{sp}^2 - \omega_m^2 + j\gamma_{sp}\omega_m} \cdot j\omega_m \tau_{ph} \cdot \eta \varepsilon g_0 \tag{A.9}$$

where

$$\gamma_{sp} = \frac{1}{\tau_{sp}} \left(1 + \frac{f_R w_0}{P_S} \right) \approx \frac{1}{\tau_{sp}} \frac{P_0}{P_S} \tag{A.10}$$

$$\omega_{sp}^2 = \frac{2 f_R^2 w_0 g_0}{P_S \tau_{sp}} = \frac{P_0}{P_S} \frac{1}{\tau_{sp} \tau_{ph}} \tag{A.11}$$

Therefore the pump RIN to laser RIN conversion ratio is given by

$$r_{RIN} = \frac{|\, w_1 / w_0 \,|^2}{\varepsilon^2} = \left| \frac{\omega_{sp}^2}{\omega_{sp}^2 - \omega_m^2 + j\gamma_{sp}\omega_m} \right|^2 = \frac{\eta^2}{1 + \frac{\gamma_{sp}^2 - 2\omega_{sp}^2}{\omega_{sp}^4} \omega_m^2 + \frac{\omega_m^4}{\omega_{sp}^4}} \tag{A.12}$$

Appendix B

The coefficient a_k of $\sum_{n=-\infty}^{+\infty} f_e(\frac{t-nT_R}{\tau})$ is defined in Eq.(B.1) where normalized time $x=t/\tau$ and duty cycle $\sigma=\tau/T_R$.

$$\begin{aligned} a_k &\equiv \frac{2}{T_R}\int_{-T_R/2}^{T_R/2} f_e(\frac{t}{\tau})\cos k\omega_R t dt \\ &= 2\sigma\int_{-1/2\sigma}^{1/2\sigma} f_e(x)\cos(2\pi kx\sigma)dx \end{aligned} \tag{B.1}$$

The coefficient c_k of $\sum_{n=-\infty}^{+\infty} \dot{f}_e(\frac{t-nT_R}{\tau})\frac{t-nT_R}{\tau}$ is defined in Eq.(B.2) and Eq.(B.3) where we assume the pulse width is much smaller than the period and thus $f_e(1/2\sigma)=0$. Also note that $c_0=0$.

$$\begin{aligned} c_k - a_k &\equiv \frac{2}{T_R}\int_{-T_R/2}^{T_R/2} \dot{f}_e(\frac{t}{\tau})\frac{t}{\tau}\cos k\omega_R t dt \\ &= 2\sigma\int_{-1/2\sigma}^{1/2\sigma} \dot{f}_e(x)x\cos(2\pi kx\sigma)dx \\ &= 2f_e(1/2\sigma)(-1)^k + 2\sigma\int_{-1/2\sigma}^{1/2\sigma} f_e(x)2\pi kx\sigma\sin(2\pi kx\sigma)dx \\ &\quad - 2\sigma\int_{-1/2\sigma}^{1/2\sigma} f_e(x)\cos(2\pi kx\sigma)dx \end{aligned} \tag{B.2}$$

$$c_k = 2\sigma\int_{-1/2\sigma}^{1/2\sigma} f_e(x)2\pi kx\sigma\sin(2\pi kx\sigma)dx \tag{B.3}$$

The coefficient b_k of $\sum_{n=-\infty}^{+\infty} f_o(\frac{t-nT_R}{\tau})$ is defined in Eq.(B.4).

$$\begin{aligned} b_k &\equiv \frac{2}{T_R}\int_{-T_R/2}^{T_R/2} f_o(\frac{t}{\tau})\sin k\omega_R t dt \\ &= 2\sigma\int_{-1/2\sigma}^{1/2\sigma} f_o(x)\sin(2\pi kx\sigma)dx \end{aligned} \tag{B.4}$$

The coefficient d_k of $\sum_{n=-\infty}^{+\infty} \dot{f}_o(\frac{t-nT_R}{\tau})\frac{t-nT_R}{\tau}$ is defined in Eq.(B.5) and Eq.(B.6).

$$\begin{aligned} d_k - b_k &\equiv \frac{2}{T_R}\int_{-T_R/2}^{T_R/2} \dot{f}_o(\frac{t}{\tau})\frac{t}{\tau}\sin k\omega_R t dt \\ &= 2\sigma\int_{-1/2\sigma}^{1/2\sigma} \dot{f}_o(x)x\sin(2\pi kx\sigma)dx \\ &= -2\sigma\int_{-1/2\sigma}^{1/2\sigma} f_o(x)2\pi kx\sigma\cos(2\pi kx\sigma)dx \\ &\quad -2\sigma\int_{-1/2\sigma}^{1/2\sigma} f_o(x)\sin(2\pi kx\sigma)dx \end{aligned} \tag{B.5}$$

$$d_k = -2\sigma\int_{-1/2\sigma}^{1/2\sigma} f_o(x)2\pi kx\sigma\cos(2\pi kx\sigma)dx \tag{B.6}$$

List of publications

Journal Publications

[1] **K. Wu**, P. Shum, S. Aditya, C. Ouyang, J. Wong, H. Lam, and K. Lee, Noise Conversion from the Pump to the Passively Mode-Locked Fiber Lasers at 1.5 μm, Optics Letters 37, pp1901 (2012)

[2] **K. Wu**, P. Shum, S. Aditya, C. Ouyang, J. Wong, H. Lam, and K. Lee, Characterization of the excess noise conversion from optical relative intensity noise in the photodetection of mode-locked lasers for microwave signal synthesis, Journal of Lightwave Technology 29, pp3622 (2011)

[3] **K. Wu**, C. Ouyang, J. Wong, S. Aditya, and P. Shum, Frequency response of the noise conversion from relative intensity noise to phase noise in the photodetection of an optical pulse train, IEEE Photonics Technology Letters 23, pp468 (2011)

[4] J. Wong, **K. Wu**, *et al.,* Vector solitons in a laser passively mode-locked by single-wall carbon nanotubes, Optics Communications 284, pp2007 (2011)

[5] C. Ouyang, P. Shum, **K. Wu**, *et al.*, Dissipative soliton (12 nJ) from an all-fiber passively mode-locked laser with large normal dispersion ," IEEE Photonics Journal 3, pp881 (2011)

[6] C. Ouyang, P. Shum, **K. Wu**, *et al.*, Bidirectional passively mode-locked soliton fiber laser with a four-port circulator, Optics Letters 36, pp2089 (2011)

[7] J. Xue, N. Li, **K. Wu**, *et al.*, Performance study and assessment of phase noise suppression by incoherent addition in a mode-locked fiber laser system, Optics Communications 285, pp153 (2011)

[8] **K. Wu**, J. Wong, P. Shum, S. Fu, C. Ouyang, H. Wang, E. Kelleher, A. Chernov, E. Obraztsova, and J. Chen, Nonlinear coupling of relative intensity noise from pump to a fiber ring laser mode-locked with carbon nanotubes, Optics Express 18, pp16663 (2010)

[9] **K. Wu**, J. Wong, P. Shum, D. Lim, V. Wong, K. Lee, J. Chen, and E. Obraztsova, Timing-jitter reduction of passively mode-locked fiber laser with a carbon nanotube saturable absorber by optimization of cavity loss, Optics Letters 35, pp1085 (2010)

Conference Publications

[1] **K. Wu**, P. Shum, and C. Ouyang, Characterization of the RIN-to-Phase-Noise Conversion Induced by Photodetectors in the Microwave Synthesis from Mode-locked Lasers, Conference on Lasers and Electro-Optics (CLEO), JTh2A.14, San Jose, U.S. (2012)

[2] **K. Wu**, C. Ouyang, P. Shum, and J. Wong, Characterization of the RIN-to-Phase-Noise Conversion Induced by Photodetectors in the Microwave Synthesis from Mode-locked Lasers, International Quantum Electronics Conference / Conference on Lasers and Electro-Optics Pacific Rim (IQEC/CLEO Pacific Rim), Sydney, Australia (2011)

[3] **K. Wu**, C. Ouyang, P. Shum, and J. Wong, Phase Noise at Harmonic Frequencies of a Mode-locked Fiber Laser and Low-timing-jitter Microwave Extraction, International Quantum Electronics Conference / Conference on Lasers and Electro-Optics Pacific Rim (IQEC/CLEO Pacific Rim), Sydney, Australia (2011)

[4] **K. Wu**, C. Ouyang, J. Wong, and P. Shum, Characterization of the RIN-to-Phase-Noise Conversion in the Microwave Synthesis from Mode-locked Lasers, Conference on Lasers and Electro-Optics (CLEO), JThB127, Baltimore, U.S. (2011)

[5] **K. Wu**, J. Wong, Z. Luo, C. Ouyang, P. Shum, and Z. Shen, Phase Noise and Timing Jitter Eliminator for Mode-locked Lasers Based on External Graphene Layers, Optical Fiber Communications / National Fiber Optic Engineers Conference (OFC/NFOEC), OThL5, Los Angeles, U.S. (2011)

[6] **K. Wu**, and P. Shum, Effect of photodetector on the noise conversion of the optical pulse train generated from mode -locked lasers, Photonics Global Conference (PGC), conf10a334, Singapore (2010)